Politecnico di Milano

School of Industrial and Information Engineering
Departement of Aerospace Science and Technology (DAER)
Master of Science in Space Engineering

Centre National D'Etudes Spatiales

ISAE Supaero

Predictive Autonomous Orbit Control: Integration of Mixed In-track Cross-track Station-keeping Manoeuvres

Master Thesis

Student:
Irene Cavallari
Matricola 875889

Politecnico di Milano Supervisor:
Prof. Camilla Colombo
CNES Supervisor:
Jérôme Thomassin
ISAE Supaero Supervisor:
Prof. Stéphanie Lizy-Destrez

Academic Year 2018-2019

Aknowledgements

Firstly, I would like to thank my tutor Jérôme Thomassin, who offered me the opportunity of the internship, and guided and supported me during this experience.

I would like to thank Maxime Echochard. His office door was always open whenever I ran into a trouble spot or had a question.

Moreover, I would like to thank Géraldine Constant-Filaire and all the team of DSO/DV/MS, for their welcome and constant openness.

I would also like to thank Professor Camilla Colombo, who provided me with support, insight and immense expertise during this work and has conveyed the passion for orbital mechanics during her course in Politecnico di Milano.

I am greteful to Professor Stéphanie Lizy-Destriez for the support, motivation and inspiration, and the great opportunities she gave me since I first arrived to ISAE Supaero.

I will be forever thankful to my parents for their encouragement, for having conveyed me a high sense of duty, for having pushed me and given me countless opportunities. A special gratitude goes to my grandmother, who has been my first teacher and who is a spring of inspiration and strength for all my family. I am also grateful to my sister, my godmother and godfather, to be always ready to support me in every way, and to my cousin Andrea, who is a point of reference for all my family. I thank uncle Maurizio to have taught me how to prepare the coffee, without which I would have not survived. I have to thank all my many relatives, aunts, uncles and cousins (impossible to mention everyone), to be a constant, never missing presence in my life.

I will always be grateful to my friends Angelica, Chiara, Margherita and Sara, to have been part of my life for more than ten years and to always believe in me. I thank Paolo, Gianluca, Anna, Francesco and Ester to have become my second little family in Toulouse. I would like to thank Rossella to have been my support in Milano and to be a great friend. Last but not least, all the dear friends that I have known and with whom I have shared my university years in Milano and Toulouse.

Abstract

Station keeping operations are essential for a satellite mission. They enable the maintenance of a satellite on a reference orbit, counteracting the effects of perturbing non-Keplerian forces. Making the orbit control autonomous would reduce the ground-based workload, with great advantages in terms of operational costs. Anyway, this raises the issue of the collision risks management process. The Centre National d'Etudes Spatial (CNES) is developing the Autonomous Orbit Control (AOC), an autonomous orbit controller and is studying an algorithmic method to make it predictable. The upcoming manoeuvres are computed in advance, allowing to establish a future action plan that makes possible to estimate the impact risk probability. Two kinds of manoeuvres can be executed at time: one to perform an in-track station keeping; the other one to perform a cross-track station keeping. This thesis work has contributed to the improvement of AOC, by conceiving and introducing of a third kind of manoeuvre, a mixed manoeuvre, allowing to handle both the in-track and the cross-track station keeping at the same time. Moreover, an algorithmic procedure has been implemented to determine the temporal slots, during which the mixed manoeuvres can be performed by fulfilling missions and systems constraints. Finally, a further study concerning the orbit inclination drift under the perturbations effects has been performed. This parameter estimation is important for the manoeuvres computation. Analytic and semi-analytic models of the inclination drift have been introduced to get a good estimation, by minimising the computational time required.

Contents

Symbols

a	semi-major axis [km]
a_p	perturbing acceleration [km/s]
e	eccentricity
e_X,e_Y	eccentricity vector's components
E	eccentric anomaly [deg]
F	thrust [N]
f	thrust-induced acceleration [km/s^2]
G	universal gravitational constant [m^{3}km^{-1}s^{-2}]
$\mathbf{h}$	angular momentum [m^{2}s^{-1}]
H	local hour angle [deg]
i	inclination [mdeg]
IJK	geocentric inertial equatorial coordinate system
n	orbital angular speed [rad/s]
$\mathbf{r}$	position vector [m]
$\mathbf{R}\theta\mathbf{N}$	Gaussian coordinate system
R_e	equatorial Earth radius [m]
t	time variable [s]
T_0	orbital period [s]
T_E	Earth rotation period [s]
T_{SO}	Sun apparent orbit period [s]
U	Earth potential [J/kg]
V_p	potential [J/kg]
$\mathbf{V}$	velocity vector [m/s]
α	argument of latitude [deg]
α^*	right ascension [deg]
γ	manoeuvre orientation angle [deg]
δ	declination [deg]
ΔT	in-track deviation [m]
ΔW	cross-track deviation [m]
μ	Earth standard gravitational parameter [m^3 s^{-2}]
ν	true anomaly [deg]
$\widehat{\rho}$	electric manoeuvre efficiency
$\rho\mathbf{TN}$	satellite coordinate system
ω	argument of perigee [deg]
Ω	right ascension of the ascending node [deg]
ω_e	Earth rotation rate [rad/s]

Introduction

All the satellites in orbit around the Earth are subjected to non-Keplerian forces, which deviate them from their assigned operational orbit: this makes station keeping operations essential in a mission. Up to now, the orbital control is performed by the missions ground segments. However, there is an increasing interest in making it autonomous, handled on-board by the satellite itself.

The Centre National d'Etudes Spatiales (CNES) has developed an autonomous orbit control method, Autonomous Orbit Control (AOC), that has been successfully tested by means of a controller demonstrator on the Demeter satellite, launched in 2004 [1]. Its advantages are several. First of all, there is a significant reduction of the operations cost since the orbit maintenance is not anymore ground-based: for a Low-Earth Orbit (LEO) constellation, it would imply a net savings in total annual operations cost in the order of 10/20% [2]. Then, the mission scheduling becomes more predicable and easier to handle. Anyway, there is still a problem to solve in order to make autonomous station keeping exploitable for missions. Indeed, the autonomous orbit control raises the issue of the collision risk management. The avoidance strategy against space debris is determined by ground stations and needs an accurate knowledge of the satellite orbit: this requirement can not be achieved with an on-board orbit control. Thus, CNES is studying a way to make AOC predictable by means of an algorithmic method under development. This thesis concerns a work of adjustment and improvement that has been conducted on it, in the contest of a six months internship at CNES.

The interest in making satellite and spacecraft operations autonomous dates back to the late 80s. NASA was investigating the way to make the control of orbital operations autonomous, with a focus on interplanetary missions to Mars [3]; indeed, some of them, requiring pinpoint landing and ascent and rendez-vous operations, would not be practicable without a greater autonomy. In those year, the first guidance, navigation and control algorithms were in development, along with the techniques to perform autonomous landing, rendez-vous and docking. The interest in the autonomous station keeping can be dated back to those years and it is increased since then, especially because of the advantages that it would bring to the management of mega-constellations on Low-Earth orbits, such as OneWeb [2][4]. Over the years, several studies and tests have been carried out. The first works are about the techniques to make the navigation systems autonomous, which is essential for an autonomous orbit control. In [5], Maute proposes a method based on the exploitation of star trackers and solar detectors for the measurement of the angles formed by the Sun, the Polar Star and the Earth seen from the satellite to determine its state vector. In [6], Chan and Bernstein proposes to perform the orbit estimation thanks to Global Positioning System (GPS) receivers. This last technique is used by Microcosm Inc., which studies an autonomous orbit controller on behalf of the US Air Force Research Laboratory and NASA. Its controller generates thruster firing commands, controlling the deviation of the orbit elements (the orbital period and the right ascension of the ascending node, in particular) from their expected values [7], [8]. In [9], De Florio *et al.* study a similar controller, based on an analytic feedback control algorithm, comparing its performance to that of a linear and a quadratic optimum regulators. Also Pervez and Xing in [10] propose an autonomous orbit control based on the classical control theory: they suggest the use of a multivariate feedback regulator, like a linear-quadratic regulator (LQR) or an H_∞ robust controller, minimising the control error on the satellite position and velocity and the control effort. These kinds of regulators have very good performances: indeed, they compute the orbit manoeuvres punctually without the need of estimating the non-Keplerian forces. However, they do not allow long-term prediction of the satellite dynamics and of its orbit. For this reason, the CNES

controller, AOC, is based on orbital mechanics, by measuring the orbital parameters deviations with respect to the guidance orbit and by applying a correction strategy based on theoretical equations. The focus is on low Earth orbits station keeping. The satellite orbit is determined on-board by means of Global Navigation Satellite System (GNSS) measurements, thanks to Global Positioning System (GPS) or GALILEO receivers. In order to reduce propellant burns, a control technique, exploiting the perturbing forces effects on the satellite orbit, has been developed [11]. The adopted strategy is adopted for satellites exploiting whether a chemical or an electric propulsion system.

To make the autonomous orbit control more predictable, CNES has implemented an algorithmic method consisting in the introduction of a predictable horizon for upcoming manoeuvres [12]. It is based on the same AOC original strategy, so on the control of the inclination, right ascension of the ascending node, semi-major axis and argument of latitude, optimising the orbit eccentricity. To this aim, two different kinds of manoeuvres are implemented according to the need: tangential manoeuvres with respect to the satellite orbits, used to perform the in-track station keeping; out-of-plane manoeuvres exploited for the cross-track station keeping. The algorithm is still under development at CNES, to improve its station keeping performance and to make it suitable also for satellites exploiting an electric propulsion system.

The main objective of the work presented in this thesis was to study and integrate an other type of manoeuvre, a mixed manoeuvre, performing at the same time an in-track and a cross-track station keeping control. It enables significantly improving the controller performance, especially if a low-thrust propulsion system is operated. Finally, always with the objective to improve the AOC algorithm, in both terms of station keeping performance and computational time, a further study has been started: it concerns the analytic estimation of the inclination drift under the effects of the orbital perturbations, whose knowledge is important for the correct computation of the out-of-plane manoeuvres.

Thus, this thesis work contribution has consisted in:

- improving the original AOC algorithm, by conceiving and introducing both impulsive and low-thrust mixed in-track cross-track manoeuvres;
- generating a algorithmic procedure to determine the temporal slots during which it is allow to perform the mixed in-track cross-track manoeuvres, on the basis of the standard manoeuvres already defined temporal slots: these slots have the objective to fulfill missions and systems constraints, such as the avoidance of the on-board instruments glare;
- introducing analytic and semi-analytic models for the computation of the inclination drift under the effects of orbital perturbations, whether provided by the literature or based on it; the semi-analytic determination of the inclination drift is a computationally not expensive way to predict the evolution of the orbital inclination, useful for an autonomous orbit control.

This thesis is organized as follows:

- Chapter 1 provides general background information: the exploited reference systems, the orbits of interest and reminders of the two-body problem and of orbital perturbations;
- Chapter 2 presents the working principles and the manoeuvres strategy of the AOC original algorithm, before the changes done during the internship;
- Chapter 3 is about the conception and the integration of impulsive mixed manoeuvres;
- Chapter 4 is about the concetpion and the integration of electric mixed manoeuvres;
- Chapter 5 concerns the methodology adopted to determine the temporal slots during which mixed manoeuvres can be performed;
- Chapter 6 presents the performed study about the analytical and semi-analytical estimation of the inclination drift induced by orbital perturbations.

0.1 Working environment

AOC has been developed at CNES and this work has been realised during an internship in this research centre. The CNES is the French space agency for space programs. It is a public, industrial and commercial, scientific and technical institution and it is financially independent.It is responsible for advising the government, implementing the French space policy and designing new space systems.

CNES has two main missions: to provide an overall vision of space solutions through its systems skills and to innovate. In addition to this, it is attentive:

- to remain attentive to users and their requirements;
- to remain at the crossroads of scientific/ technological laboratories, and industrial;
- to stimulate scientific, technological and industrial research and innovation for institutional and commercial requirements.

It is structured into four centres, each dedicated to complementary objectives. There is the headquarter in Paris Les Halles. All CNES administrative operations are directed from it. Administrators at headquarters, together with the overseeing ministries, establish and promote CNES policy. They also define the strategic guidelines for the agency technical centres and its relations with outside partners.

The centre in Toulouse (CST) is more focused on satellites control and orbital vehicles design and development. The opening of the CST in 1968 was the result of the decentralization of French high-tech industries from the Paris area to the provinces. The CST replaced the former space centre at Bretigny-sur-Orge. At this key site for space research, the centre develops complete space systems with its partners in industry and the scientific community, right up to their entry into operational service. The CST is unique in terms of its size and the diversity of its activities. The CST participates in scientific and instrumentation projects, and leads research and application programs such as Argos, Helios and Insight. It also leads the orbital system projects (satellites and on-board payloads, ground segments) and satellite station acquisition and keeping operations. It manages the technical policy and preparation of the future as well. This centre develops and executes scientific balloon-borne experiments and ensures the use of data as well as development of innovative applications.

Then, there is a centre is in Kourou, where the launch base is placed: the Guaiana Space centre (CSG). It is dedicated to Europe's launcher program. It coordinates all resources needed for launch infrastructures, launcher and payload preparation, control of launch operations and the equipment required for launch. As well, it participates in the construction of new launch units (Ariane 6).

Finally, the Launcher Directorate (DLA) is placed in Paris Daumesnil, where all the study, design and development of Ariane, Soyuz and Vega launch systems are carried out. It leads all developments of new European launch systems under contract to the European Space Agency (ESA). The DLA maintains constant supervision of the launcher from production to marketing and launch, through Arianespace. It develops technological demonstrators in order to prepare for future launchers. It also leads the research on new concepts for launchers and advanced propulsion systems.

The internship has taken place in the Toulouse Space centre. In particular, it has been conducted into a division of Orbital Systems and Flight Dynamics Department, that is the Space Mechanics Service.

The Orbital Systems and Flight Dynamics Department (DSO/DV) develops and carries out the studies on the space mechanics aspects, such as orbit restitution and resources localization and on the Attitude and Orbit Control System (AOCS). All the phases Research and Technology (R&T), phases 0 and A, development phases and operation monitoring are carried out in this department. In the department one can find several divisions. One of them is the Space Mechanics Systems (MS) division. Its goals are to coordinate the support for space mechanics aspects in a project, to optimise satellite positioning and maintenance strategies for isolated or in-formation satellites, collision avoidance, in-orbit services, interplanetary transfers and guided atmospheric flights.

Chapter 1

Background

1.1 Reference Frame

Several reference frames have to be considered in this work. Indeed, even if the AOC algorithm exploits mainly one reference system, others are used for the models and the conception. Below, the main reference frames are introduced.

Geocentric inertial equatorial coordinate system IJK

It is inertial and centred at the Earth centre [13] (Figure 1.1). The **I** axis lies on the equatorial plane and points the vernal equinox, which corresponds to the ascending node of the apparent orbit of the Sun around the Earth. The **K** axis is perpendicular to the equatorial plane. Finally, the **J** axis lies on the equatorial plane, completing the frame according to the right-hand rule.

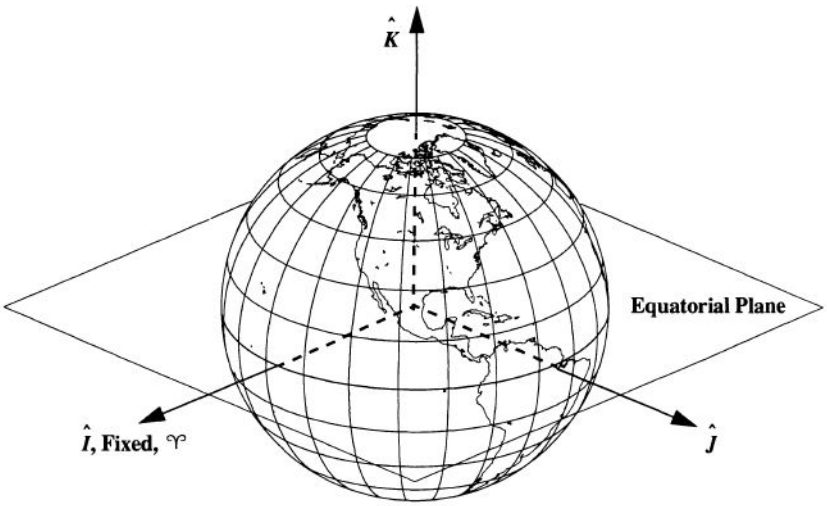

Fig. 1.1: Geocentric inertial equatorial coordinate system [13]

Celestial intermediate reference frame (CIRF)

It is a quasi-inertial geocentric reference frame [14]. It is related to the geocentric equatorial coordinate system by a time-dependent rotation accounting for precession and nutation phenomena. It is the reference frame exploited by AOC for the orbit propagation and the manoeuvres computation.

Gaussian coordinate system RθN

It is a rotating system centred at the satellite [13] (Figure 1.2): the **R** axis has the direction points from the Earth center towards the satellite in the direction of its position vector; the θ axis points in the direction of the satellite velocity vector and it is perpendicular to the **R** axis; the **N** axis is normal to the orbit plane. Considering the satellite ground track, the in-track displacements are normal to the **R** axis; in the case of quasi-circular orbits, they are nearly parallel to the θ axis. The cross-track positions are normal to the orbital plane, along the N axis.

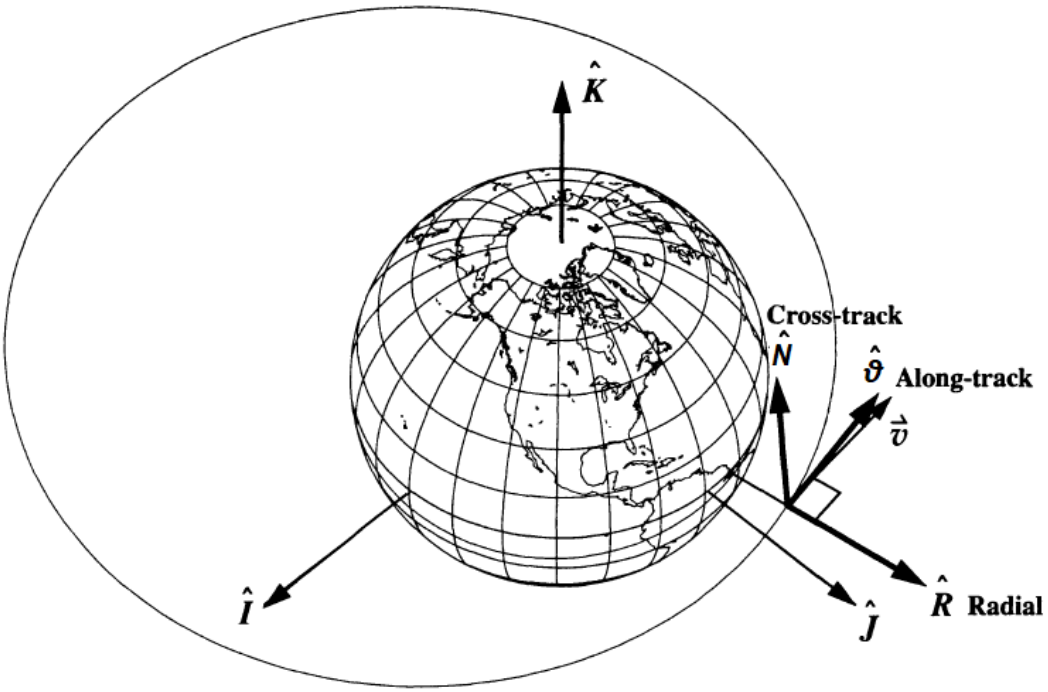

Fig. 1.2: Gaussian coordinate system [13]

Satellite coordinate system ρTN

It is a rotating reference frame centred at the satellite [13] (figure 1.3). The **T** axis is tangential to the orbit: it has the direction of the satellite velocity vector. The **N** axis is normal to the orbital plane. The ρ axis lies on the orbital plane and completes the frame according to the right-hand rule. With regard to the satellite ground track, the in-track displacements are deviations along the **T** axis. It is possible to observe that this reference frame coincides with the Gaussian coordinate system in case of a perfectly circular orbit.

The time is expressed exploiting both the International Atomic Time (TAI) [15] and the Modified Julian date (MJD) [13].

1.2 Two-body problem

In the Keplerian two-body problem, considering a satellite orbiting around the Earth, only the potential of the planet, modeled as perfectly spherical, is taken into account. The acceleration of the satellite is:

$$\ddot{\mathbf{r}} = -\frac{\mu}{r^3}\mathbf{r} \tag{1.1}$$

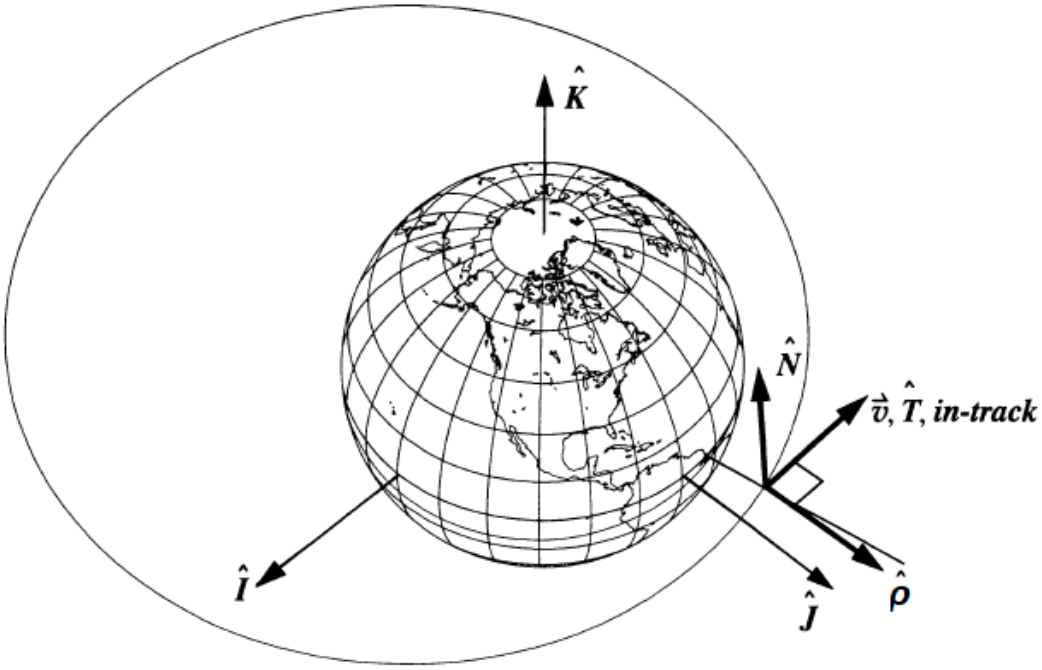

Fig. 1.3: Satellite coordinate system [13]

where $\mathbf{r}$ is the position vector, r its modulus and μ the standard gravitational parameter. Indeed $U = -\frac{\mu}{r^2}$ is the Earth gravitational potential.

Classically, in this context, there are specific elements defined as orbital parameters which are exploited to characterise an orbit. They are:

- The semi-major axis a, which is the measure of the amplitude of the orbit. It is related to the energy, integral of motion:

$$E = \frac{V^2}{2} - \frac{r}{\mu} = -\frac{\mu}{2a} \tag{1.2}$$

  where V is the orbital velocity.

- The eccentricity e, referring to the shape the orbital shape. It is the modulus of the eccentricity vector which is a constant of integration of the two-body problem:

$$\mathbf{e} = \frac{\mathbf{h} \times \mathbf{V}}{\mu} - \frac{\mathbf{r}}{r} \tag{1.3}$$

  where $\mathbf{h} = \mathbf{r} \times \mathbf{V}$ is the satellite angular momentum and it is another integral of motion. The eccentricity vector points the orbit perigee, the closer point to Earth.

- The inclination i is the tilt of the orbital plane with respect to the equatorial plane. It can been mathematically defined exploiting the $\mathbf{K}$ and the $\mathbf{N}$ axis, being these vectors normal with respect to the considered planes. Thus, we have:

$$\cos i = \mathbf{NK} \tag{1.4}$$

- The right ascension of the ascending node Ω is the angle measured positively from the $\mathbf{I}$ axis to the ascending node, which is the point on the equatorial plane where the satellite crosses the equator from south to north. The opposite point with respect to the Earth center is the

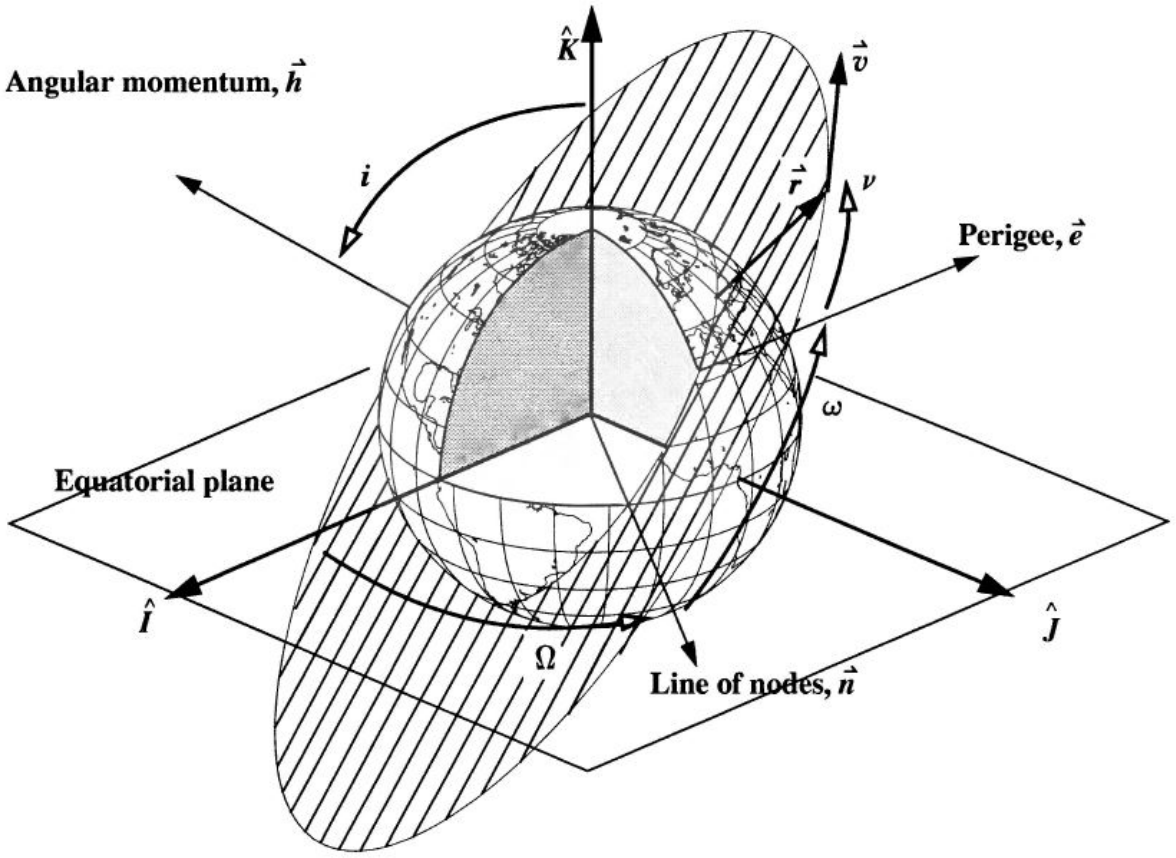

Fig. 1.4: Generic orbit orientation and geometry with respect to the geocentric inertial coordinate system [13]

descending node; the segment connecting these two points is the so called line of nodes. It is possible to write:

$$\cos\Omega = \mathbf{I}(\mathbf{K} \times \mathbf{N}) \tag{1.5}$$

- The argument of perigee ω is the angle between the ascending node and the perigee:

$$\cos\omega = \frac{\mathbf{e} \cdot (\mathbf{K} \times \mathbf{h})}{e|\mathbf{h}|} \tag{1.6}$$

- The true anomaly ν is the angle defining the current satellite position with respect to the perigee:

$$\cos\nu = \mathbf{r} \cdot \mathbf{e} \tag{1.7}$$

1.3 Orbital parameters

For low-Earth missions, generally the orbits of interest are quasi circular. Their eccentricity is in the order of 10^{-3} [16]. Therefore, in order to define the satellite position along the orbit, the notion of argument of perigee is less significant as well as the notion of true anomaly. Instead of these classical orbital parameters, the eccentricity vector of coordinates e_X and e_Y and the argument of latitude, α, are exploited. Hence, the orbital parameters used are:

a;

$e_X = e\cos\omega$, $e_Y = e\sin\omega$;

i;

Ω;

$\alpha = \omega + \nu$, defined as argument of latitude.

1.4 Orbital Perturbations

Reality doesn't conform exactly the Keplerian model. Earth is not a perfect sphere and there are other bodies gravitational potentials and other additional forces acting on the satellite that have to be taken into account. The actual satellite motion will deviate from the theoretical two-body path: the deviations from the nominal Keplerian orbit are called orbital perturbations. The real satellite acceleration is:

$$\ddot{\mathbf{r}} = -\frac{\mu}{r^3}\mathbf{r} + \mathbf{a_p} \tag{1.8}$$

where $\mathbf{a}_p$ is the acceleration component due to the perturbing forces.

1.4.1 Osculating parameters

Under the effect of perturbations, the orbital parameters change in time: they are no longer two-body elements, but osculating elements. It is possible to determine the variation of each parameter as a function of the perturbing acceleration, as shown in [13].

The state vector $[\mathbf{r};\mathbf{v}]$ can be expressed as a function of the osculating parameters and time:

$$\mathbf{r} = \mathbf{x}(a, e, i, \Omega, \alpha, t) = \mathbf{x}(\mathbf{c}, t) \tag{1.9}$$

$$\mathbf{V} = \dot{\mathbf{x}}(a, e, i, \Omega, \alpha, t) = \dot{\mathbf{x}}(\mathbf{c}, t) \tag{1.10}$$

where $\mathbf{v}$ is the velocity vector and $\mathbf{c} = [a, e, i, \Omega, \alpha]^T$.
Consequently, equation 1.8 can be re-written as:

$$\ddot{\mathbf{x}}(\mathbf{c}, t) + \frac{\mu\mathbf{x}(\mathbf{c}, t)}{|\mathbf{x}(\mathbf{c}, t)|^3} = \mathbf{a_p} \tag{1.11}$$

In order to get the variation of the osculating parameters in time, this last equation can be compared with the one obtained differentiating twice equation (1.9). Differentiating once, the result is:

$$\dot{\mathbf{x}}(\mathbf{c}, t) = \frac{d\mathbf{x}(\mathbf{c}, t)}{dt} = \frac{\partial\mathbf{x}(\mathbf{c}, t)}{\partial t} + \sum \frac{\partial\mathbf{x}(\mathbf{c}, t)}{\partial c_i}\frac{dc_i}{dt}$$

To differentiate a second time, a constraint has to be imposed to assure that each state vector defines an osculating ellipse:

$$\sum \frac{\partial\mathbf{x}(\mathbf{c}, t)}{\partial c_i}\frac{dc_i}{dt} = 0 \tag{1.12}$$

Indeed, an osculating orbit is a two-body orbit at each instant of time.

Thus, we have:

$$\dot{\mathbf{x}}(\mathbf{c}, t) = \frac{d\mathbf{x}(\mathbf{c}, t)}{dt} = \frac{\partial\mathbf{x}(\mathbf{c}, t)}{\partial t} \tag{1.13}$$

$$\ddot{\mathbf{x}}(\mathbf{c}, t) = \frac{\partial^2\mathbf{x}(\mathbf{c}, t)}{\partial t^2} + \sum \frac{\partial\dot{\mathbf{x}}(\mathbf{c}, t)}{\partial c_i}\frac{dc_i}{dt} \tag{1.14}$$

In the case of a Keplerian two body problem, where no perturbation is active, the relations would have been:

$$\ddot{\mathbf{x}}(\mathbf{c},t) + \frac{\mu \mathbf{x}(\mathbf{c},t)}{|\mathbf{x}(\mathbf{c},t)|^3} = 0 \tag{1.15}$$

$$\ddot{\mathbf{x}}(\mathbf{c},t) = \frac{d^2\mathbf{x}(\mathbf{c},t)}{dt^2} = \frac{\partial^2 \mathbf{x}(\mathbf{c},t)}{\partial t^2} \tag{1.16}$$

Comparing equations (1.11), (1.14), (1.15) and (1.16), we get:

$$\sum \frac{\partial \dot{\mathbf{x}}(\mathbf{c},t)}{\partial c_i} \frac{dc_i}{dt} = \mathbf{a_p}$$

Thus, we can write:

$$\begin{bmatrix} \sum \frac{\partial \mathbf{x}(\mathbf{c},t)}{\partial c_i} \frac{dc_i}{dt} \\ \sum \frac{\partial \dot{\mathbf{x}}(\mathbf{c},t)}{\partial c_i} \frac{dc_i}{dt} \end{bmatrix} = \begin{bmatrix} 0 \\ \mathbf{a_p} \end{bmatrix} \tag{1.17}$$

Taking the dot product of the first equation with $\partial c_i/\partial \dot{\mathbf{x}}$ and of the second with $\partial c_i/\partial \mathbf{x}$ and adding the obtained relations, we get :

$$\sum \Big(\frac{\partial c_j}{\partial \mathbf{x}} \frac{\partial \mathbf{x}}{\partial c_i} + \frac{\partial c_j}{\partial \dot{\mathbf{x}}} \frac{\partial \dot{\mathbf{x}}}{\partial c_i} \Big) \frac{dc_i}{dt} = \frac{\partial c_j}{\partial \dot{\mathbf{x}}} \mathbf{a_p}$$

As the elements are mutually independent, the result is:

$$\sum \delta_{i,j} \frac{dc_i}{dt} = \frac{\partial c_j}{\partial \dot{\mathbf{x}}} \mathbf{a_p}$$

where $\delta_{i,j}$ is the Kronecker δ. So each orbital parameter changes in time because of the action of the natural perturbing forces, according to the following relation:

$$\frac{dc_j}{dt} = \frac{\partial c_j}{\partial \dot{\mathbf{x}}} \mathbf{a_p} \tag{1.18}$$

1.4.2 Gauss equations

Gauss developed a system of equations, allowing to express the rates of change of the osculating parameters as explicit functions of the acceleration induced by the specific disturbing forces. As reference frame, the Gaussian coordinate system is exploited; the generic specific acceleration considered is of the type:

$$\mathbf{a_p} = a_{p_R} \mathbf{R} + a_{p_\theta} \theta + a_{p_N} \mathbf{N} \tag{1.19}$$

The procedure to obtain the Gaussian equations follows the one by [13].

To derive the expression for the semi-major axis, it is helpful to exploit the expression (1.2), linking it to the energy integral. The energy is not constant as in the Keplerian two-body problem; it varies in time because of the work made by the perturbing forces:

$$\frac{dE}{dt} = \mathbf{a}_p \mathbf{V}$$

In view of the following equivalences:

$$\mathbf{r} = r\mathbf{R}$$

$$\mathbf{V} = \dot{r}\mathbf{R} + \dot{\nu} r \theta = \dot{\nu} \Big(\frac{dr}{d\nu} \mathbf{R} + r\theta \Big)$$

we get:

$$\frac{dE}{dt} = \dot{\nu}\left(\frac{dr}{d\nu}a_{p_R} + r a_{p_\theta}\right)$$

where:

$$r = \frac{p}{1 + e\cos\nu}$$

$$\frac{dr}{d\nu} = \frac{re\sin\nu}{1 + e\cos\nu}$$

$$r\dot{\nu} = h = \sqrt{\mu a(1-e^2)} = na^2\sqrt{1-e^2}$$

being h the modulus of the orbital angular momentum $\mathbf{h}$. Applying equation (1.2), the result is:

$$\frac{da}{dt} = \frac{\mu}{2}\frac{1}{E^2}\frac{dE}{dt} = \frac{2e\sin\nu}{n\sqrt{1-e^2}}a_{p_R} + \frac{2a\sqrt{1-e^2}}{nr}a_{p_\theta}$$

The eccentricity of an elliptical orbit can be expressed as:

$$e = \sqrt{1 - \frac{h^2}{a}} \tag{1.20}$$

(see [13]). The h the angular momentum, which is constant in the two body problem, varies in time in case of perturbed motion:

$$\frac{d\mathbf{h}}{dt} = \mathbf{r} \times \mathbf{a_p} = r a_{p_R}\mathbf{N} - r a_{p_N}\theta$$

$$\frac{d\mathbf{h}}{dt} = \dot{h}\mathbf{N} + h\frac{d\mathbf{N}}{dt}$$

$$\dot{h} = r a_{p_R}$$

Differentiating equation (1.20) results in:

$$\frac{de}{dt} = \frac{1}{2}\left(1 - \frac{h^2}{a}\right)^{-1/2}\left(-\frac{2}{\mu a}\frac{dh}{dt} + \frac{h^2}{\mu a^2}\frac{da}{dt}\right) =$$
$$= -\frac{h}{\mu a e}r f_\theta + \frac{h^2}{2\mu a^2 e}\left(\frac{2e\sin\nu}{n\sqrt{1-e^2}}a_{p_R} + \frac{2a\sqrt{1-e^2}}{nr}a_{p_\theta}\right)$$

Exploiting the relations:

$$h = \sqrt{\mu a(1-e^2)}$$

$$n = \sqrt{\mu/a^3}$$

we get:

$$\frac{de}{dt} = \frac{\sqrt{1-e^2}}{na}\left(\sin\nu a_{p_R} + \left(\cos\nu + \frac{e + \cos\nu}{1 + e\cos\nu}\right)a_{p_\theta}\right)$$

Because the angular momentum is directed as the **N** axis, it can be exploited in order to define the orbital inclination, following the relation (1.4):

$$\cos i = \frac{\mathbf{hK}}{h} \tag{1.21}$$

Differentiating the equation results in:

$$-\sin i \frac{di}{dt} = \frac{1}{h}\frac{d\mathbf{h}}{dt}\mathbf{K} - \frac{1}{h^2}\dot{h}(\mathbf{hK})$$

Considering that $\theta\mathbf{K} = \cos\alpha \sin i$ and that $\mathbf{NK} = \cos i$, and substituting $d\mathbf{h}/dt$ and $\dot{h}$:

$$\frac{di}{dt} = \frac{r\cos\alpha a_{p_N}}{na^2\sqrt{1-e^2}}$$

Also the right ascension of the ascending node can be defined as a function of the angular momentum, applying it to equation (1.5):

$$\cos\Omega = \mathbf{I}\frac{\mathbf{K}\times\mathbf{h}}{|\mathbf{K}\times\mathbf{h}|} \tag{1.22}$$

Differentiating the equation, we get:

$$-\sin\Omega\frac{d\Omega}{dt} = \mathbf{I}\frac{\mathbf{K}\times\dot{\mathbf{h}}}{|\mathbf{K}\times\mathbf{h}|} - \mathbf{I}\frac{\mathbf{K}\times\mathbf{h}}{|\mathbf{K}\times\mathbf{h}|^2}\frac{d}{dt}|\mathbf{K}\times\mathbf{h}| =$$
$$= \frac{\mathbf{I}\big(\mathbf{K}(ra_{p_R}\mathbf{N} - ra_{p_N}\theta\big)}{h\sin i} - \frac{h\cos\Omega\sin i}{h^2\sin i^2}\Big(\dot{h}\sin i + h\cos i\frac{di}{dt}\Big)$$

Since $\mathbf{I}(\mathbf{K}\times\theta) = (\mathbf{I}\times\mathbf{K})\theta = -\mathbf{J}\theta = \sin\alpha\sin\Omega - \cos\alpha\cos\Omega\cos i$:

$$\frac{d\Omega}{dt} = \frac{r\sin\alpha a_{p_N}}{na^2\sqrt{1-e^2}\sin i}$$

The argument of latitude is the angle between the vector aligned with the line of nodes $\mathbf{K}\times\mathbf{h}$ and the position vector $\mathbf{r}$:

$$\cos\alpha = \frac{\mathbf{r}}{r}\frac{\mathbf{K}\times\mathbf{h}}{|\mathbf{K}\times\mathbf{h}|} \tag{1.23}$$

So, differentiating equation 1.23 we obtain:

$$-\sin\alpha\frac{d\alpha}{dt} = \frac{|\mathbf{K}\times\mathbf{h}|\big(\mathbf{K}\times\dot{\mathbf{h}}\mathbf{r}\big) + (\mathbf{K}\times\mathbf{hr})\frac{d}{dt}|\mathbf{K}\times\mathbf{h}|}{r|\mathbf{K}\times\mathbf{h}|^2}$$

From the following equations:

$$\mathbf{K}\times\mathbf{Nr} = r\sin i\cos\alpha$$

$$\mathbf{K}\times\theta\mathbf{r} = r\theta\times\mathbf{RK} = -r\mathbf{NK} = -r\cos i$$

$$\mathbf{K}\times\mathbf{hr} = rh\sin i\cos\alpha$$

by means of a substitution, we have:

$$\frac{d\alpha}{dt} = -\frac{r\cot i\sin\alpha a_{p_N}}{h}$$

Summarising, the equations of Gauss are:

$$\frac{da}{dt} = \frac{2}{n\sqrt{1-e^2}}(e\sin\nu a_{p_R} + (1+e\cos\nu)a_{p_\theta}) \tag{1.24}$$

$$\frac{de}{dt} = \frac{\sqrt{1-e^2}}{na}\Big(\sin\nu a_{p_R} + \Big(\cos\nu + \frac{e+\cos\nu}{1+e\cos\nu}\Big)a_{p_\theta}\Big) \tag{1.25}$$

$$\frac{di}{dt} = \frac{r\cos\alpha}{na^2\sqrt{1-e^2}}a_{p_N} \tag{1.26}$$

$$\frac{d\Omega}{dt} = \frac{r\sin\alpha}{na^2\sqrt{1-e^2}\sin i}a_{p_N} \tag{1.27}$$

$$\frac{d\alpha}{dt} = -\frac{r\cot i\sin\alpha}{na\sqrt{1-e^2}}a_{p_N} \tag{1.28}$$

Another useful Gaussian equation concerns the true anomaly. The two-body problem trajectory equation is expressed as follows:

$$r(1+e\cos\nu) = -\frac{h^2}{\mu}$$

Differentiating it results in:

$$r(\frac{de}{dt}\cos\nu - e\sin\nu\frac{d\nu}{dt}) = -2\frac{h}{\mu}\frac{dh}{dt}$$

Substituting de/dt and dh/dt, we get:

$$\frac{d\nu}{dt} = \frac{\sqrt{1-e^2}}{nae}\Big(\cos\nu a_{p_R} - \frac{2+e\cos\nu}{1+e\cos\nu}a_{p_\theta}\Big) \tag{1.29}$$

1.4.3 Lagrange equations

Another set of equations defining the orbital elements drift was developed by Lagrange. Differently from the set of Gauss equations which are valid for every kind of perturbing acceleration, it can be applied if the perturbation is represented by a gravitational potential: the acceleration is conservative and equal to the gradient of the potential. In order to derive them, it is possible to apply the procedure by Battin [17].

Considering the system (1.17), let's perform the dot product between the first equation and $-\frac{\partial\dot{\mathbf{x}}(\mathbf{c},t)}{\partial c_k}$ and between the second and $\frac{\partial\mathbf{x}(\mathbf{c},t)}{\partial c_k}$:

$$\sum\frac{dc_i}{dt}\Big(\frac{\partial\mathbf{x}(\mathbf{c},t)}{\partial c_k}\frac{\partial\dot{\mathbf{x}}(\mathbf{c},t)}{\partial c_i} - \frac{\partial\mathbf{x}(\mathbf{c},t)}{\partial c_i}\frac{\partial\dot{\mathbf{x}}(\mathbf{c},t)}{\partial c_k}\Big) = \frac{\partial V_p}{\partial c_k}$$

being V_p the perturbing potential. Let be:

$$[c_i,c_k] \equiv \frac{\partial\mathbf{x}(\mathbf{c},t)}{\partial c_k}\frac{\partial\dot{\mathbf{x}}(\mathbf{c},t)}{\partial c_i} - \frac{\partial\mathbf{x}(\mathbf{c},t)}{\partial c_i}\frac{\partial\dot{\mathbf{x}}(\mathbf{c},t)}{\partial c_k} \tag{1.30}$$

$[c_i,c_k]$ is the so called Lagrangian bracket. Thus, it is possible to express the time derivative of each orbital element as:

$$\frac{d\mathbf{c}}{dt} = L^{-1}\frac{\partial V_p}{\partial\mathbf{c}} \tag{1.31}$$

where:

$$L = \begin{bmatrix} [c_1, c_1] & \cdots & [c_1, c_{n_{oe}}] \\ \vdots & \ddots & \vdots \\ [c_{n_{oe}}, c_1] & \cdots & [c_{n_{oe}}, c_{n_{oe}}] \end{bmatrix}$$

In order to determine the orbital elements drifts it is convenient to to exploit the orbital frame, having an axis directed as the eccentricity vector $\mathbf{e}$, an axis directed as the angular momentum $\mathbf{h}$ and an axis directed as $\frac{\mathbf{h}\times\mathbf{e}}{eh}$. Indeed, the position vector and the velocity vectors can be expressed as:

$$\mathbf{x} = \mathbf{R} \begin{bmatrix} a(\cos E - e) \\ a\sqrt{1-e^2}\sin E \sin \nu \\ 0 \end{bmatrix}$$

$$\dot{\mathbf{x}} = \mathbf{R} \begin{bmatrix} -\sqrt{\frac{\mu}{a}}\frac{\sin E}{1-e\cos E} \\ -\sqrt{\frac{\mu(1-e^2)}{a}}\frac{\cos E}{1-e\cos E} \\ 0 \end{bmatrix}$$

where

$$\mathbf{R} = \begin{bmatrix} \cos\Omega\cos\omega - \sin\Omega\sin\omega\cos i & -\cos\Omega\sin\omega - \sin\Omega\cos\omega\cos i & \sin\Omega\sin i \\ \sin\Omega\cos\omega - \cos\Omega\sin\omega\cos i & -\sin\Omega\sin\omega - \cos\Omega\cos\omega\cos i & -\cos\Omega\sin i \\ \sin\omega\sin i & \cos\omega\sin i & \cos i \end{bmatrix}$$

and E is the eccentric anomaly:

$$\tan\frac{E}{2} = \sqrt{\frac{1-e}{1+e}}\tan\frac{\nu}{2}$$

The eccentric anomaly can be expressed as a function of the so called mean anomaly $M = \sqrt{\frac{\mu}{a^3}}\cdot t$ by means of the following equation:

$$M = E - e\sin E$$

Therefore, we have:

$$\frac{\partial(\mathbf{x}, \dot{\mathbf{x}})}{\partial(\Omega, \omega, i)} = \frac{\partial \mathbf{R}}{\partial((\Omega, \omega, i)}\Big(\begin{bmatrix} a(\cos E - e) \\ a\sqrt{1-e^2}\sin E\sin\nu \\ 0 \end{bmatrix}, \begin{bmatrix} -\sqrt{\frac{\mu}{a}}\frac{\sin E}{1-e\cos E} \\ -\sqrt{\frac{\mu(1-e^2)}{a}}\frac{\cos E}{1-e\cos E} \\ 0 \end{bmatrix}\Big)$$

$$\frac{\partial(\mathbf{x}\dot{\mathbf{x}})}{\partial(a, e, M)} = \mathbf{R}\frac{\partial}{\partial(a, e, M)}\Big(\begin{bmatrix} a(\cos E - e) \\ a\sqrt{1-e^2}\sin E\sin\nu \\ 0 \end{bmatrix}, \begin{bmatrix} -\sqrt{\frac{\mu}{a}}\frac{\sin E}{1-e\cos E} \\ -\sqrt{\frac{\mu(1-e^2)}{a}}\frac{\cos E}{1-e\cos E} \\ 0 \end{bmatrix}\Big) \tag{1.32}$$

Considering that the following conditions hold:

- $[c_i, c_i] = 0$
- $[c_i, c_k] = -[c_k, c_i]$

and evaluating the Lagrangian brackets at the perigee, where $E = 0$ (the Lagrangian brackets don't depend on time explicitly so they can be evaluated for any convenient value of t and consequently of E), the Lagrangian equations can be determined:

$$\frac{da}{dt} = -\frac{2}{na}\frac{\partial V_p}{\partial M} \tag{1.33}$$

$$\frac{de}{dt} = \frac{\sqrt{1-e^2}}{na^2 e}\frac{\partial V_p}{\partial \omega} + \frac{e^2-1}{na^2 e}\frac{\partial V_p}{\partial M} \tag{1.34}$$

$$\frac{di}{dt} = \frac{1}{na^2\sqrt{1-e^2}\sin i}\frac{\partial V_p}{\partial \Omega} + \frac{\cot i}{na^2\sqrt{1-e^2}}\frac{\partial V_p}{\partial \omega} \tag{1.35}$$

$$\frac{d\Omega}{dt} = \frac{-1}{na^2\sqrt{1-e^2}\sin i}\frac{\partial V_p}{\partial i} \tag{1.36}$$

$$\frac{d\omega}{dt} = -\frac{\sqrt{1-e^2}}{na^2 e}\frac{\partial V_p}{\partial e} + \frac{\cot i}{na^2\sqrt{1-e^2}}\frac{\partial V_p}{\partial i} \tag{1.37}$$

$$\frac{dM}{dt} - n = \frac{2}{na}\frac{\partial V_p}{\partial a} - \frac{e^2-1}{na^2 e}\frac{\partial V_p}{\partial e} \tag{1.38}$$

1.4.4 Osculating parameters evolution

The evolution of each orbital parameter p can be modeled as the sum of different terms:

- a term associated to the secular evolution :

$$p_{sec}(t) = \sum_{i=1}^{n} B_i (t - t_0)^i$$

- a term associated to the periodical evolution:

$$p_{per}(t) = \sum_{j=1}^{m} A_j \sin\left(2 * \pi * \frac{t}{T_j} + \phi_j\right)$$

- a mean parameter p_0.

The secular evolution represents the long term trend of the orbital parameters: in this time, indeed, the perturbations periodic effects can be neglected. Each periodic component of the parameters evolution is characterised by its proper period T_j and amplitude A_j. In particular, according to the period length, it is possible to identify:

- the short period evolution if $T_j < T_0$, being T_0 the orbital period;
- the medium period evolution if $T_0 < T_j < T_e$, being T_e the Earth rotation period;
- the long term period evolution if $T_j > T_e$.

Finally the mean parameter is the nominal value of the orbital parameter.
Thus, it is possible to write :

$$p(t) = p_0 + p_{per}(t) + p_{sec}(t);$$

1.4.5 Disturbing Forces

There are several contributions to the perturbing acceleration. Indeed, the general form of the equation of motion can be expressed as [18]:

$$\frac{d^2\mathbf{r}}{dt^2} = \mathbf{a}_{GR} + \mathbf{a}_{3rd} + \mathbf{a}_{SRP} + \mathbf{a}_D + \mathbf{a}_{sf}$$

where:

- $\mathbf{a}_{GR}$ is the acceleration due to real Earth gravitational potential, which includes also the Keplerian two-body acceleration.

- $\mathbf{a}_{3rd}$ is the acceleration generated by the gravitational attraction of other celestial bodies, mainly the Moon and the Sun: it corresponds to the so called three-body effect.
- $\mathbf{a}_{SRP}$ is the Solar radiation pressure effect, due to the photons radiated from the Sun.
- $\mathbf{a}_D$ is the acceleration due to the atmospheric drag. When the orbit is less than 1500 km, the air molecules encounters the satellite, determining a variation of their momentum. This change creates a force acting on the surface of the satellites itself. The impact of this force depends on the local atmosphere density and on the satellite cross-section area.
- $\mathbf{a}_{sf}$ is the sum of smaller effects, for example the tides, the Earth infrared radiation and the Earth optical albedo. In this work only the effect of terrestrial tides are considered: they can be seen an time-varying components of the geopotential (more precisely of the geopotential coefficients C_{lm} and S_{lm} that will be introduced in the following paragraph).

In the following paragraph, the first contribution, due to the geopotential is analysed more in detail. In Table 1.1 , the effects of each perturbing forces on the orbital parameters are summarised, following the analysis performed in [16] and in [19] .

Earth's gravity field

Since Earth is not a perfectly spherical body, its gravitational potential differs from the one assumed in the Keplerian model. The classical assumed model for it is the one by Chobotov [18]. The potential is defined as an infinite series of harmonics:

$$U = \frac{\mu}{r}\sum_{l=0}^{\infty}\sum_{m=0}^{k}\Big(R_e/r\Big)^l P_{lm}\Big(\sin\delta\Big)\Big(C_{lm}\cos m\lambda + S_{lm}\sin m\lambda\Big) \tag{1.39}$$

where P_{lm} are Legendre functions (see Appendix A), δ is the satellite declination (which is the angular distance of the satellite with respect to the equatorial plane), and λ is the satellite longitude, with respect to the geocentric inertial coordinate system. The terms C_{lm} and S_{lm} are coefficients to determine from observation. Finally, R_e is the Earth equatorial radius. For $l = 0$ and $m = 0$, the potential of a perfect spherical body is obtained.

There are three kinds of harmonics: the zonal, the sectorial and the tesseral harmonis. The zonal ones correspond to the zero order terms ($m = 0$). Taking only them into account, the potential becomes:

$$U = \frac{\mu}{r}\Big(1 - \sum_{l=2}^{\infty}(R_e/r)^l J_l P_l(\sin\delta)\Big) \tag{1.40}$$

where $J_l = -C_{l0}$.

Sectorial harmonics are function of longitude only($l = m$). Tesseral harmonics are function of both longitude and declination ($l \neq m$).

The harmonic which determines the strongest perturbation due to the Earth shape is the zonal one associated to the term J_2. J_2 is almost 1000 times larger than the next largest coefficient (J_3).

1.5 Sun-synchronous orbits

Very frequently the orbits of interest are not only quasi-circular, but also sun-synchronous.

Adequate and not fluctuating light conditions are useful for remote-sensing missions, above all if no other means other than the Sun light is used to the Earth. For this reason, the local hour of the passage of the satellite over a certain region is something fixed. The local hour is the angle between the plane of the meridian which passes through the satellite and the plane of the Sun meridian. For convention an angle of 0° corresponds to 12 h. In a sun-synchronous orbit, the local hour is constant: the angle between the Sun and the orbital plan does not change. The orbital perturbations are exploited in order to obtain sun-synchronous orbits. The right ascensions of the ascending node drift is imposed

equal to the Earth rotation angular velocity, by means of selecting and orbit with a semi-major axis and an inclination fulfilling the following equation:

$$-\frac{3}{2}J_2\Big(\frac{R_e}{a(1-e^2)}\Big)^2\sqrt{\frac{\mu}{a^3}}\cos i = \omega_e \tag{1.41}$$

being ω_e the Earth angular velocity. Since the semi-major axis is usually fixed to fulfill missions requirement, the inclination is selected in order to make the orbit sun-synchronous. For low-Earth orbits, these orbits are almost polar.

Table 1.1: Perturbing forces effects on orbital parameters

orbital parameter	**semi-major axis**	
	type of perturbation	effects
	geopotential	short and medium period effects
	lunar-solar potential	no effect
	atmospheric drag	short period, long period and secular effects
	solar radiation pressure	no effect
orbital parameter	**eccentricity**	
	type of perturbation	effects
	geopotential	short period, medium period, long period and secular effects
	lunar-solar potential	no effect
	atmospheric drag	short period and secular effects
	solar radiation pressure	long period effects (secular if sun-synchronous)
orbital parameter	**inclination**	
	type of perturbation	effects
	geopotential	short and medium period effects
	lunar-solar potential	long period effect (secular if sun-synchronous)
	atmospheric drag	short period, long period and secular effects
	solar radiation pressure	long period effects (secular if sun-synchronous)
orbital parameter	**right ascension of the ascending node**	
	type of perturbation	effects
	geopotential	short period, medium period and secular effects
	lunar-solar potential	long period effect (secular if sun-synchronous)
	atmospheric drag	short period and long period effects
	solar radiation pressure	no effects
orbital parameter	**argument of latitude**	
	type of perturbation	effects
	geopotential	short period, medium period and secular effects
	lunar-solar potential	no effect
	atmospheric drag	short period, long period and secular effects
	solar radiation pressure	long period effects (secular if sun-synchronous)

Chapter 2

Autonomous Orbit Control : Control Strategy and Original CNES Algorithm

In this chapter the models on which AOC is based and the algorithm as it was before the internship are described. AOC is implemented in JAVA and exploits the CNES libraries *Sirius* and *Patrius*.

2.1 Manoeuvres strategy

As in case of a standard on-ground station keeping, the main aim of AOC is to confine the satellite ground traces inside a specific spatial box. Indeed, the satellite orbit deviates from the nominal orbit because of the perturbing forces acting on it: manoeuvres have to be performed to hinder them. In comparison to the standard station keeping, the automatic control has to assure the spacecraft inside a reduced box, not only for mission-linked reasons, but also for on-ground antennas stations planification for tracking and telemetry. With respect to the satellite ground track, the box is defined by the in-track largest admitted deviation ΔT and the cross-track one, ΔW, in both the directions. The in-track station keeping is the control of the satellite on the orbital plane; the cross-track station keeping is the control of the orbital plane orientation (see Figure 2.1).

To fulfill the station keeping requirements, the natural perturbations are exploited: the reference and guidance orbit is not Keplerian, but it is perturbed by the geopotential effect and the manoeuvre strategy is based on its natural evolution. Moreover, the control has been moved from a direct one, based on the measurement of ΔT and ΔW, to an indirect one, based on the variation of selected orbital parameters.There exist an interdependence among these lasts and the variations of the in-track and cross-track positions.

The in-track position changes at the variation of several parameters, which are the argument of latitude, the eccentricity, the argument of the ascending node [12]:

$$\frac{\Delta T}{a} = 2(\Delta e_x \sin\alpha - \Delta e_y \cos\alpha) + \Delta\Omega + \Delta\alpha \tag{2.1}$$

From the equation (2.1), it is possible to observe that the variation of the argument of latitude has a direct effect on ΔT.

Experimentally, it has been observed that the cross-track position changes with the variation of several orbital parameters like the inclination, the semi-major axis, the argument of latitude, but the parameter with the largest influence is right ascension of the ascending node [20].

The temporal evolution of both the argument of latitude and the right ascension of the ascending node under the perturbing forces effects is fast, being parabolic. Thus, the cross-track station keeping is assured limiting the variation of $\Delta\Omega$ and the in-track one imposing a control on $\Delta\alpha$.

Two kinds of manoeuvres were designed: tangential and out-of-plane, with respect to the satellite orbit. They were designed as impulsive, with the hypothesis of a chemical propulsion system. Then, their conception has been extended to integrate the case of satellites exploiting an electrical propulsion system.

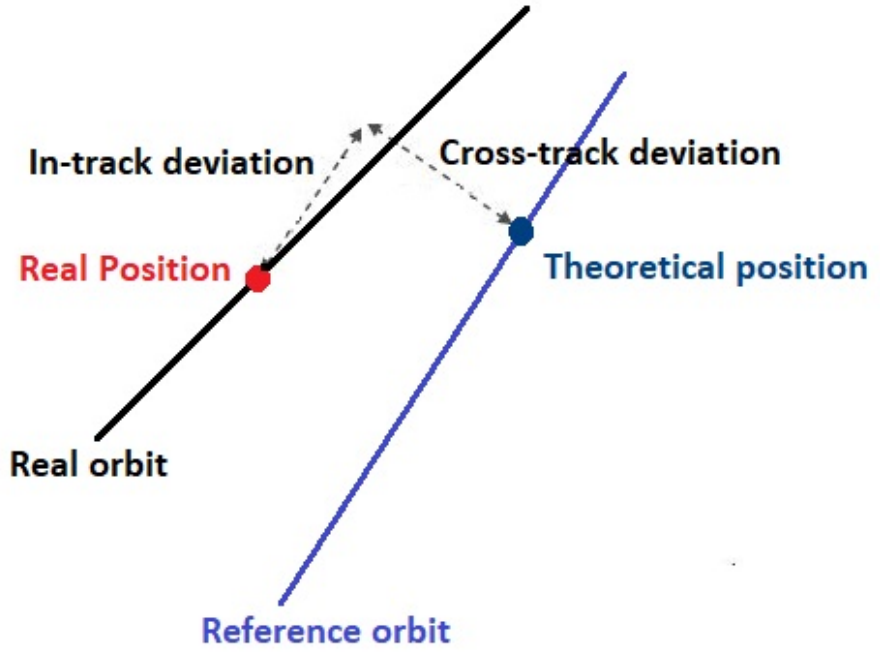

Fig. 2.1: Definition of in-track and cross-track deviations

2.1.1 Thrust effects

Before describing the manoeuvres implementation, the thrust effects on the orbital parameters is analysed. The thrust induces on the satellite an acceleration composed by three components: the radial f_ρ, the tangential f_T and the normal f_N. To determine the orbital parameters variations that it induces, it is treated as a perturbation: the Gauss equations (from (1.24) to (1.29)) are used. The hypothesis of quasi circular orbit is assumed, such that the two reference frames $\mathbf{R}\theta\mathbf{N}$ and $\rho\mathbf{TN}$can be considered coincident and several simplifications can be adopted:

- the eccentricity can be considered null: $e \sim 0$;
- the orbital radius can be considered coincident with the semi-major axis: $a = r$;
- the orbital velocity magnitude V can be considered constant and equal to the product between the semi-major axis and the orbital angular velocity: $V = an$.

Moreover, considering that:

$$\frac{de_X}{dt} = \cos\omega\frac{de}{dt} - e\sin\omega\frac{d\omega}{dt} \tag{2.2}$$

$$\frac{de_Y}{dt} = \sin\omega\frac{de}{dt} + e\sin\omega\frac{d\omega}{dt} \tag{2.3}$$

$$\frac{d\omega}{dt} = \frac{d\alpha}{dt} - \frac{d\nu}{dt} \tag{2.4}$$

the following relations are obtained:

$$\frac{da}{dt} = \frac{2a}{V}f_T \tag{2.5}$$

$$\frac{de_X}{dt} = \frac{\sin\alpha}{V} f_R + \frac{2\cos\alpha}{V} f_T \tag{2.6}$$

$$\frac{de_Y}{dt} = \frac{\cos\alpha}{V} f_R + \frac{2\sin\alpha}{V} f_T \tag{2.7}$$

$$\frac{di}{dt} = \frac{\cos\alpha}{V} f_N \tag{2.8}$$

$$\frac{d\Omega}{dt} = \frac{\sin\alpha}{V\sin i} f_N \tag{2.9}$$

$$\frac{d\alpha}{dt} = -\frac{\sin\alpha\cos i}{V\sin i} f_N \tag{2.10}$$

With the assumption of impulsive manoeuvres, the following expressions can be deduced:

$$\Delta a = \frac{2a}{V}\Delta V_T \tag{2.11}$$

$$\Delta e_X = \frac{\sin\alpha}{V}\Delta V_\rho + \frac{2\cos\alpha}{V}\Delta V_T \tag{2.12}$$

$$\Delta e_Y = \frac{\cos\alpha}{V}\Delta V_\rho + \frac{2\sin\alpha}{V}\Delta V_T \tag{2.13}$$

$$\Delta i = \frac{\cos\alpha}{V}\Delta V_N \tag{2.14}$$

$$\Delta\Omega = \frac{\sin\alpha}{V\sin i}\Delta V_N \tag{2.15}$$

$$\Delta\alpha = -\frac{\sin\alpha\cos i}{V\sin i}\Delta V_N \xrightarrow{polar orbits} 0 \tag{2.16}$$

where ΔV_ρ, ΔV_T and ΔV_N indicate respectively the radial, tangential and normal directions of $\Delta\mathbf{V}$.

It can be observed that it is possible to impose a direct variation of Ω and α by directing the thrust in the normal direction. However, this is not the implemented strategy. Considering the equation (2.16) concerning the argument of latitude, the reason is evident: in case of quasi-polar orbits the thrust effect would be almost negligible. More in general, another reason concerns the fuel consumption. The direct manoeuvres, aimed to modify a considered parameter, are more expensive than the rendez-vous manoeuvres, which impose a variation to the parameter time derivative. Actually, this is true only if a relatively long time is admitted for the manoeuvres realization. As explained in [16], calling y the generic parameter to modify, the two possible manoeuvres are:

- direct: $\Delta y = K_1\Delta x_1$;
- rendez-vous: $\Delta\dot{y} = K_2\Delta x_2$, so $\Delta y = K_2\Delta x_2\Delta t$

where x_1 and x_2 are other two generic orbital parameters and K_1 and K_2 are proportionality coefficients. Calling C_1 and C_2 the two manoeuvres consumption, given by:

$$C_1 = C_{m1}\Delta x_1$$
$$C_2 = 2C_{m2}\Delta x_2$$
$$C_m = \frac{\partial m}{\partial x}$$

it can be deduced that

$$C_1 < C_2 \Leftrightarrow \Delta t < 2\frac{C_{m2}}{C_{m1}}\frac{|K_1|}{|K_2|} = \Delta t_{12} \tag{2.17}$$

being Δt_{12} the drift time. Thus, after a time equal to Δt_{12}, a rendez-vous manoeuvre is more economic. This is the case of interest: indeed, the guidance orbit is not a Keplerian one and the objective is not to join a given orbit but to keep the considered one in an admitted spatial box.

2.1.2 Out-of-plane manoeuvres

The guidance orbit is not Keplerian: it is affected by the effects of the geopotential perturbation. The main component of this last one, causing the nodal drift, is the J_2 term. Under its effect the natural evolution of nodal drift is quadratic, as demonstrated in [13].

The nodal drift is sensitive to inclination changes, more than to changes of a and e:

$$\Delta\dot{\Omega} = \frac{3}{2}n\Big(\frac{R_e}{a(1-e^2)}\Big)^2 J_2 \sin i\Delta i + O(\Delta i)^2 \tag{2.18}$$

$$\Delta\dot{\Omega} = -\dot{\Omega}\tan i\Delta i + O(\Delta i)^2 \tag{2.19}$$

The inclination drift at time t is:

$$\Delta i = \Delta i_0 + \frac{di}{dt}(t - t_0) \tag{2.20}$$

$$\frac{di}{dt} = f(perturbations) \tag{2.21}$$

where the term di/dt is evaluated considering other perturbations effects as explained later and it can be considered constant over time: the inclination drift is linear. Thus, the nodal drift is:

$$\Delta\Omega = -\dot{\Omega}\tan i\frac{di}{dt}(t - t_0)t^2 - -\dot{\Omega}\tan i\Delta i_0(t - t_0) \tag{2.22}$$

In Figure 2.2, the natural evolution of Δi and $\Delta\Omega$ are shown: the first one is linear and increasing, the second one is parabolic and convex; it is also possible to have a decrease of Δi and a concave parabolic trend of $\Delta\Omega$. The oscillations, which are visible along the curves, are due to other perturbations effects, mainly the solar-lunar gravitation one.

In order to reduce as much as possible the number of manoeuvres (so, also the fuel consumption), this trend is exploited. The manoeuvre is performed only in proximity of a defined threshold $\Delta\Omega_{threshold}$, depending on the largest admitted ΔW. Moreover, in order to delay a next station keeping operation, the manoeuvre is conceived to target a tangent parabola: so the given ΔV is such that $\Delta\dot{\Omega}$ is modified, not directly $\Delta\Omega$.

At the date of the manoeuvre, the values $\Delta\Omega_{mes}$ and $\Delta\dot{\Omega}_{mes}$ (where the subscript *mes* means measured) are measured and the targeted $\Delta\dot{\Omega}_{targeted}$ is defined. So, it is possible to deduce the variation of $\Delta\dot{\Omega}$, $\Delta\dot{\Omega}_{comm}$ (where *comm* means commanded), to impose:

$$\Delta\Omega_{comm} = \Delta\dot{\Omega}_{targeted} - \Delta\dot{\Omega}_{mes} \tag{2.23}$$

If $\Delta\Omega_{mes} > -\Delta\Omega_{mes}$ and $\Delta\dot{\Omega}_{mes} > 0$, applying quadratic equations, the result is:

$$\Delta\dot{\Omega}_{comm} = -\sqrt{2\Delta\ddot{\Omega}_{targeted}}\sqrt{\Delta\Omega_{max} + \Delta\Omega_{mes}} - \Delta\dot{\Omega}_{mes} \tag{2.24}$$

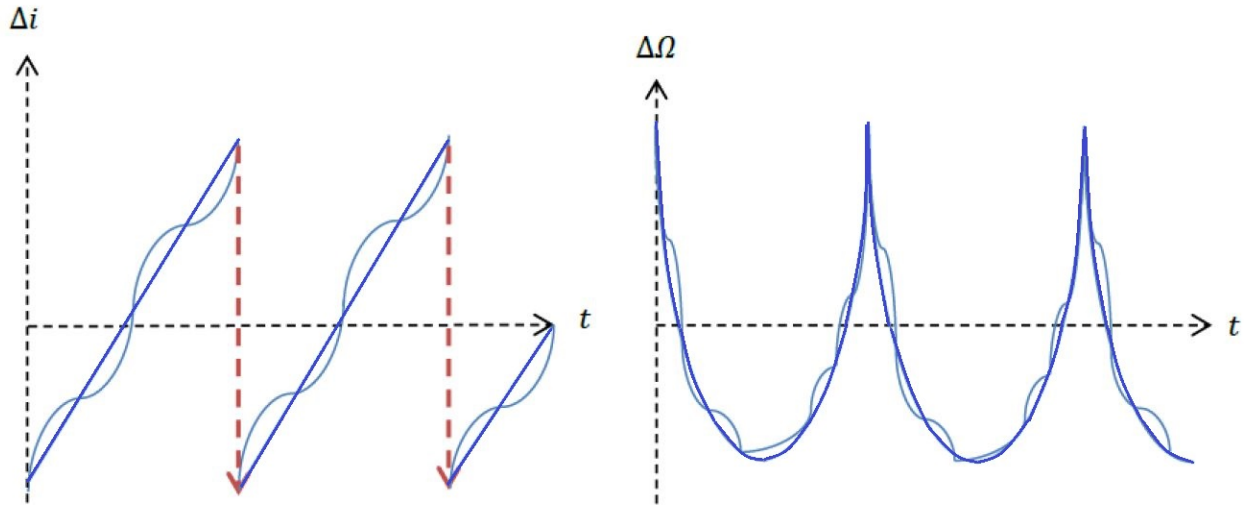

Fig. 2.2: Trends of the inclination and right ascension of the ascending node and manoeuvre strategy

where $\Delta\Omega_{max}$ is the largest admissible value of $\Delta\Omega$ and $\Delta\ddot{\Omega}_{targeted}$ is defined as follows:

$$\Delta\ddot{\Omega}_{targeted} = \dot{\Omega}\tan i\frac{di}{dt} \tag{2.25}$$

In the case $\Delta\Omega_{mes} = -\Delta\Omega_{max}$ and $\Delta\dot{\Omega}_{mes} < 0$, it is evident that $\Delta\dot{\Omega}_t = 0$, so:

$$\Delta\dot{\Omega}_{comm} = -\Delta\dot{\Omega}_{mes} \tag{2.26}$$

Since this last manoeuvre doesn't follow the natural evolution of $\Delta\Omega$, it implies a larger consumption of fuel: it has to be avoided as much as possible. The value $\Delta\Omega_{max}$ in equation (2.24) is chosen in order to fulfill this objective. It defines the targeted parabola vertex: indeed, this last is a point of coordinate $(\widehat{t}, \Delta\Omega_{max})$. To assure a good orbit station keeping and to avoid the manoeuvre described by equation (2.26), $\Delta\Omega_{max}$ is not imposed to be equal to $\Delta\Omega_{threshold}$, in terms of absolute value: a smaller value is adopted. It will be indicated as $\Delta\Omega_{tg\_parab}$. In the following, more details are provided about the definition of both $\Delta\Omega_{threshold}$ and $\Delta\Omega_{tg\_parab}$.

Once defined $\Delta\dot{\Omega}_{comm}$, the variation of inclination to be imposed is deduced:

$$\Delta i = \Delta\dot{\Omega}_{comm}/k_{\Omega-i} \tag{2.27}$$

Therefore, to perform the manoeuvre is necessary to impose a variation of inclination, while not changing $\Delta\Omega = \Delta\Omega_{mes}$ (Figure 2.3). From equations (2.14) and (2.15), it is evident that this is possible by directing the thrust in the normal direction and by performing the manoeuvre at $\alpha = 0$ or $\alpha = \pi$, i.e. at the orbital nodes. Because of this characteristic of the out-of-plane manoeuvres, they are also called *inclination manoeuvres*. The value of ΔV is expressed as:

$$\Delta V = V\Delta i \tag{2.28}$$

Inclination evolution

When considering di/dt, it is necessary to consider the three main sources of perturbation: the Moon and the Sun gravitation, the atmospheric drag and the terrestrial tides. The last two sources are usually neglected, as the long period variation of inclination is mainly consequence of a third body (Sun and Moon) effect. However, during periods characterised by a strong solar activity it is not possible to neglect the other two sources without committing significant errors.

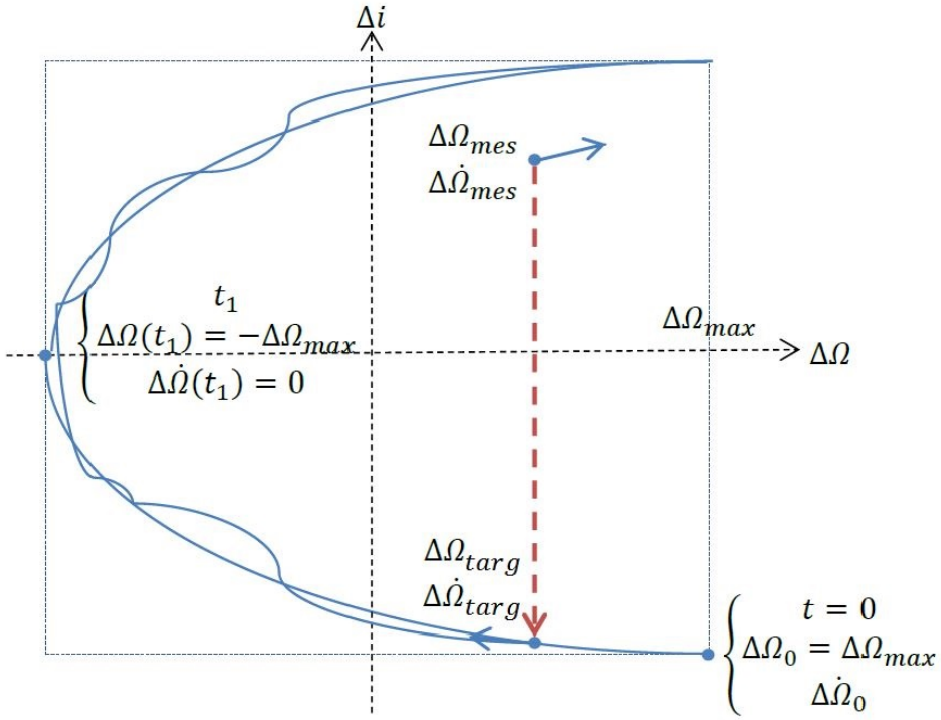

Fig. 2.3: Model of the evolution of the right ascension of the ascending node as a function of inclination

The inclination evolution due to a three body gravitational potential is:

$$\frac{di}{dt}_{3rdB} = \frac{3}{2}\frac{\mu}{nd^3}\frac{Z}{\sqrt{1-e^2}}(\cos\omega(1+4e^2)X - \sin\omega(e^2)Y) \tag{2.29}$$

where:

- μ: gravitational parameter of the third body
- X, Y, Z : components of the vector going from the Earth to the third body
- $d = \sqrt{X^2+Y^2+Z^2}$

(see [21]).

Since an analytic model of the other two sources effects is complex, they are deduced from the past inclination evolution (obtained by means of a backwards numerical propagation in the simulator) by subtracting the effects of the Sun and Moon potentials. An averaged value of di/dt is obtained and it is considered constant for the next $\Delta\Omega$ semi-parabola.

Quasi-equatorial orbits

While considering smaller and smaller value of the nominal orbital inclination, the implemented strategy becomes problematic. Indeed, the value Δi to impose is significant, and it can become too important for nominal orbits which are not polar. In these cases, the manoeuvre is split. If the value Δi to be imposed is too high, it is reduced to its largest possible value and a direct variation of $\Delta\Omega$ is also planned. This manoeuvre has some limitations. By considering equation (2.1), it is evident that, in order to assure an in-track deviation smaller than the largest admitted ΔT, the variation of the right ascension of the ascending node implies a variation of the eccentricity. This last one can't be excessive in order to maintain the orbit quasi-circular. So the manoeuvre has to be executed at a convenient argument of latitude and the value $\Delta\Omega_{comm}$ is bounded.

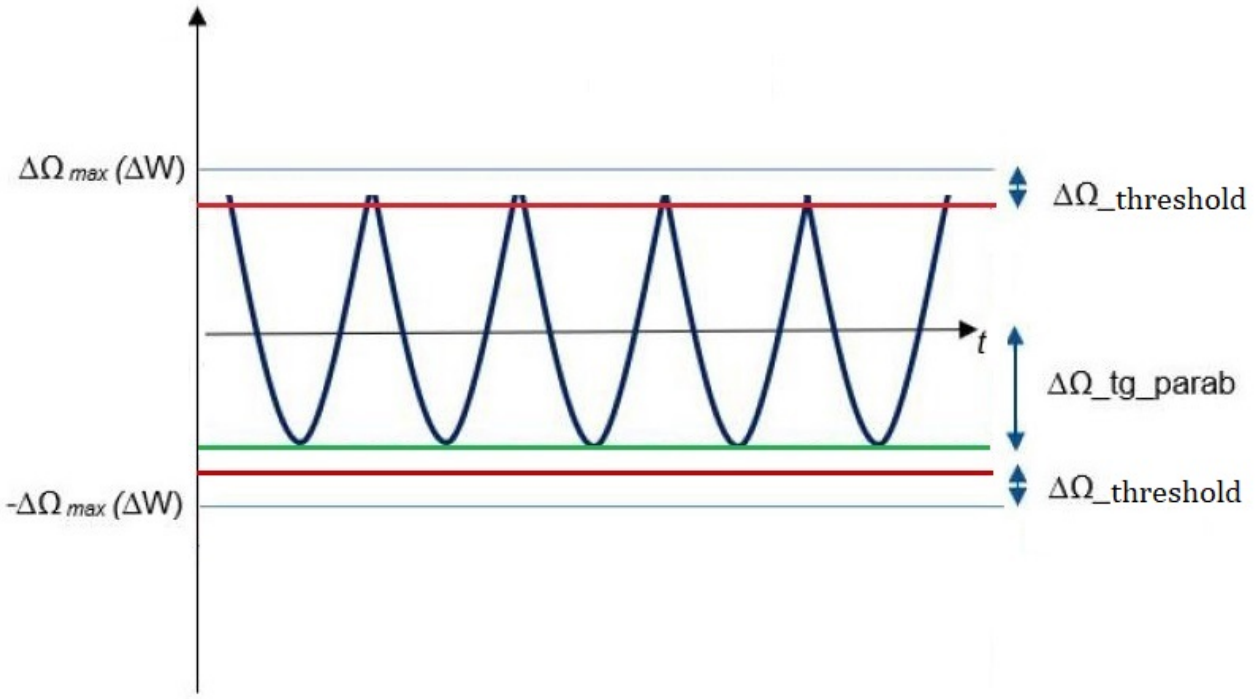

Fig. 2.4: Control margins for the inclination controller [20]

Thresholds

As already highlighted, the manoeuvre depends on two control values: the control margin $\Delta\Omega_{threshold}$ and the targeted $\Delta\Omega_{tg\_parab}$. The former represents the threshold that activates the manoeuvre when overcome. The latter defines the targeted parabola and, as consequence, the ΔV to be imposed. $\Delta\Omega_{tg\_parab}$ is smaller than $\Delta\Omega_{threshold}$: a margin is taken in such a way that the specified threshold is not overcome in case of not predicted satellite dynamics variations, as the ones due to the solar activity. Moreover, it is imposed also to avoid as much as possible the manoeuvres associated to equation (2.26), that imply a fuel over consumption. The value of $\Delta\Omega_{threshold}$ is defined as a margin of ΔW, while $\Delta\Omega_{tg\_parab}$ is expressed as a percentage of ΔW.

Table 2.1: Control margins

Margins	$\Delta\Omega_{tg\_parab}$	$\Delta\Omega_{threshold}$
Definition	$\%\Delta W$	$1 - \%\Delta W$

2.1.3 In-Plane manoeuvres

Also the secular drift of the argument of latitude is caused by the geopotential perturbation. Under the effect of the J_2 term, it is [16]:

$$\frac{1}{\dot{\alpha}}\Delta\dot{\alpha} = -\frac{3}{2a}\left[1 + \frac{7}{2}J_2\left(\frac{R_e}{a}\right)^2(4\cos i^2 - 1)\right]\Delta a - 6J_2\left(\frac{R_e}{a}\right)^2 \sin 2i\Delta i \tag{2.30}$$

As the inclination drift, also the semi-major axis drift can be considered linear. As consequence, the argument of latitude drift is quadratic and highly dependant on both Δa and Δi. In Figure 2.5, it is shown the evolution of the argument of latitude and of the semi-major axis. The strategy adopted for the in-track station keeping is very similar to the one adopted in the case of the cross-track one. A manoeuvre is performed only when $\Delta\alpha$ is close to an imposed threshold and a tangent parabola is targeted.

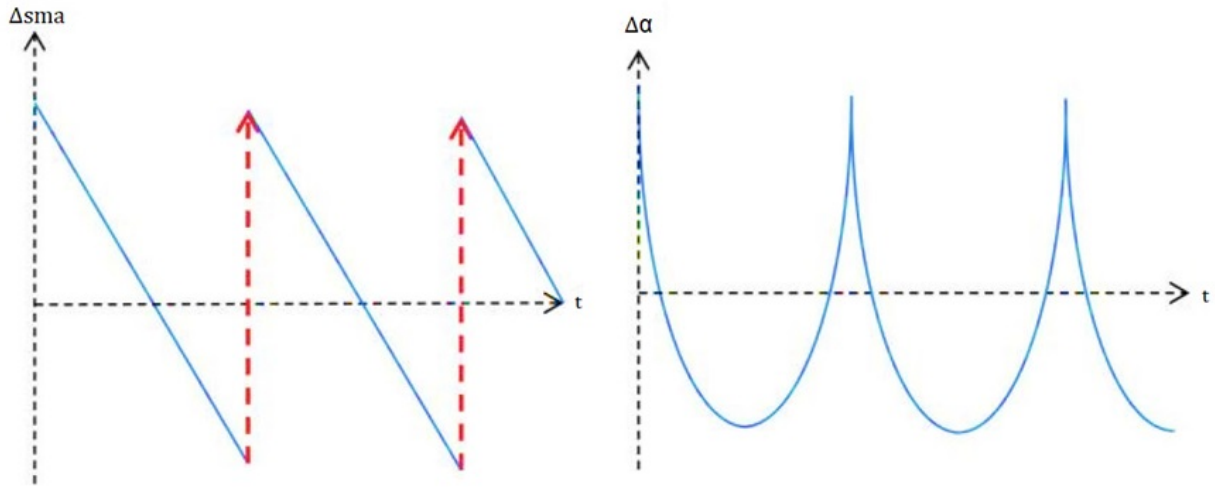

Fig. 2.5: Trends of the semi-major axis and argument of latitude and manoeuvre strategy

At the manoeuvre date, $\Delta\alpha_{mes}$ and $\Delta\dot{\alpha}_{mes}$ are computed, and the variation to be imposed is deduced:

$$\Delta\dot{\alpha}_{comm} = \Delta\dot{\alpha}_{targeted} - \Delta\dot{\alpha}_{mes} \tag{2.31}$$

where $\Delta\alpha_{targeted}$ is the targeted drift.

If $\Delta\alpha_{mes} > -\Delta\alpha_{max}$ and $\Delta\dot{\alpha}_{mes} > 0$, from quadratic relations, the result is expressed as:

$$\Delta\dot{\alpha}_{comm} = -\sqrt{2\Delta\ddot{\alpha}_{targeted}}\sqrt{\Delta\alpha_{max} + \Delta\alpha_{mes}} - \Delta\dot{\alpha}_{mes} \tag{2.32}$$

where $\Delta\ddot{\alpha}_t = f(perturbations)$.

If $\Delta\alpha_{mes} = -\Delta\alpha_{max}$ and $\Delta\dot{\alpha}_{mes} < 0$, $\Delta\dot{\alpha}_{targeted} = 0$, we have:

$$\Delta\dot{\alpha}_{comm} = -\Delta\dot{\alpha}_{mes} \tag{2.33}$$

Since this last manoeuvre does not follow the natural evolution of $\Delta\alpha$, it implies an over consumption of fuel. In order to avoid it, the same strategy used for out-of-plane manoeuvre is adopted. The value $\Delta\alpha_{max}$, identifying the targeted parabola vertex, is imposed equal to $\Delta\alpha_{tg\_parab}$, which is smaller than the imposed threshold triggering the manoeuvre.

To obtain the desired drift, a variation of the semi-major axis is imposed:

$$\Delta a = \Delta\dot{\alpha}_{comm}/k_{\alpha-a} - k_{\alpha-i}\Delta i/k_{\alpha-a} \tag{2.34}$$

This is the reason the in-plane manoeuvres are also called *sma (semi-major axis) manoeuvres.*

The thrust has to be directed tangentially to the orbit. The value of ΔV, from equation 2.11, is computed as follows:

$$\Delta V = \frac{\Delta a}{2a} V \tag{2.35}$$

Of course, this kind of manoeuvre implies also a variation of eccentricity, as it can be deduced from equations (2.12) and (2.13):

$$\Delta e_X = \frac{2\cos\alpha}{V}\Delta V \tag{2.36}$$

$$\Delta e_Y = \frac{2\sin\alpha}{V}\Delta V \tag{2.37}$$

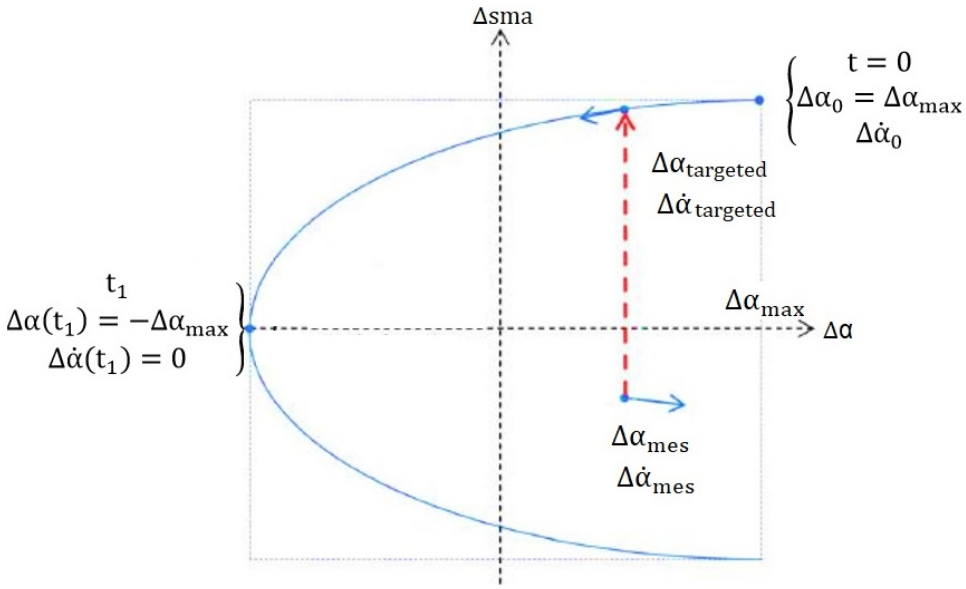

Fig. 2.6: Model of the evolution of the argument of latitude as a function of the semi-major axis

Since Δe_X and Δe_Y have to kept close to zero, the manoeuvre should be performed as closer as possible to the optimal argument of latitude, equal to (Figure 2.7):

$$\alpha_{optim} = \arctan \frac{\Delta e_Y}{\Delta e_X} \tag{2.38}$$

with Δe_X and Δe_Y computed at the date of the manoeuvre. The correction of eccentricity that the manoeuvre provides is:

$$corr_{ecc} = \Delta e - \sqrt{\Delta e^2 + \Delta e_{man}^2 - 2\Delta e \Delta e_{man} \cos(\alpha_{man} - \alpha_{optim})} \tag{2.39}$$

$$\Delta e_{man} = \frac{2}{V} \Delta V \tag{2.40}$$

where α_{man} is the argument of latitude at which the manoeuvre is performed.

Thresholds

The in-plane manoeuvres depend on three control variables: the margins $\Delta\alpha_{threshold\_up}$ and $\Delta\alpha_{threshold\_down}$ and the targeted $\Delta\alpha_{tg\_parab}$. The first two represent the thresholds that activate the manoeuvre when overcome: the first is associated to the manoeuvre defined by to equation (2.32); the second one is associated to the manoeuvre defined by equation (2.33). They are imposed as margin of ΔT. $\Delta\alpha_{tg\_parab}$ characterises the targeted parabola: the required ΔV depends on it. It is smaller than $\Delta\alpha_{threshold\_down}$: a margin is taken in order to assure the correct in-track station keeping in case of not predicted variations of the satellite dynamics, as the ones due to the solar activity. Moreover, it is imposed also to avoid as much as possible the manoeuvres associated to equation 2.33, that implies a fuel over consumption. Its value is defined as a percentage of ΔT.

Since the two kinds of manoeuvres, with a positive variation of the semi-major axis and with a negative one, are regulated independently, the first ones are called *sma-up manoeuvres*, the second ones *sma-down manoeuvres*.

Table 2.2: Control margins [20]

Margins	$\Delta\alpha_{tg\_parab}$	$\Delta\alpha_{threshold\_up}$	$\Delta\alpha_{threshold\_down}$
Definition	$\%\Delta T$	$1 - \%\Delta T$	$1 - \%\Delta T$

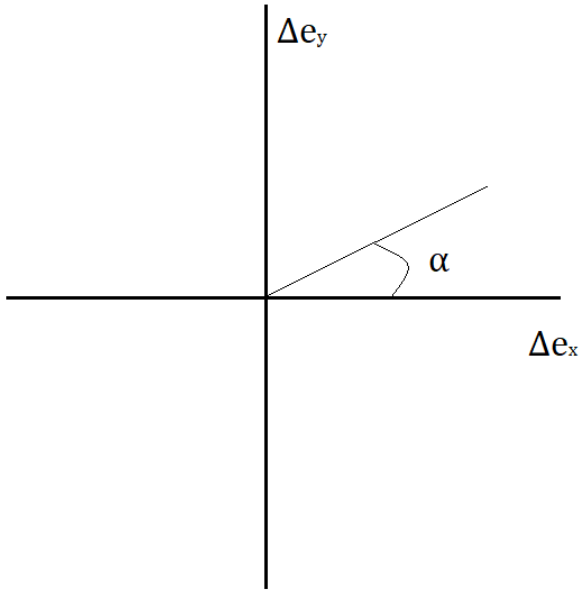

Fig. 2.7: Relation between the argument of latitude, Δe_X and Δe_Y

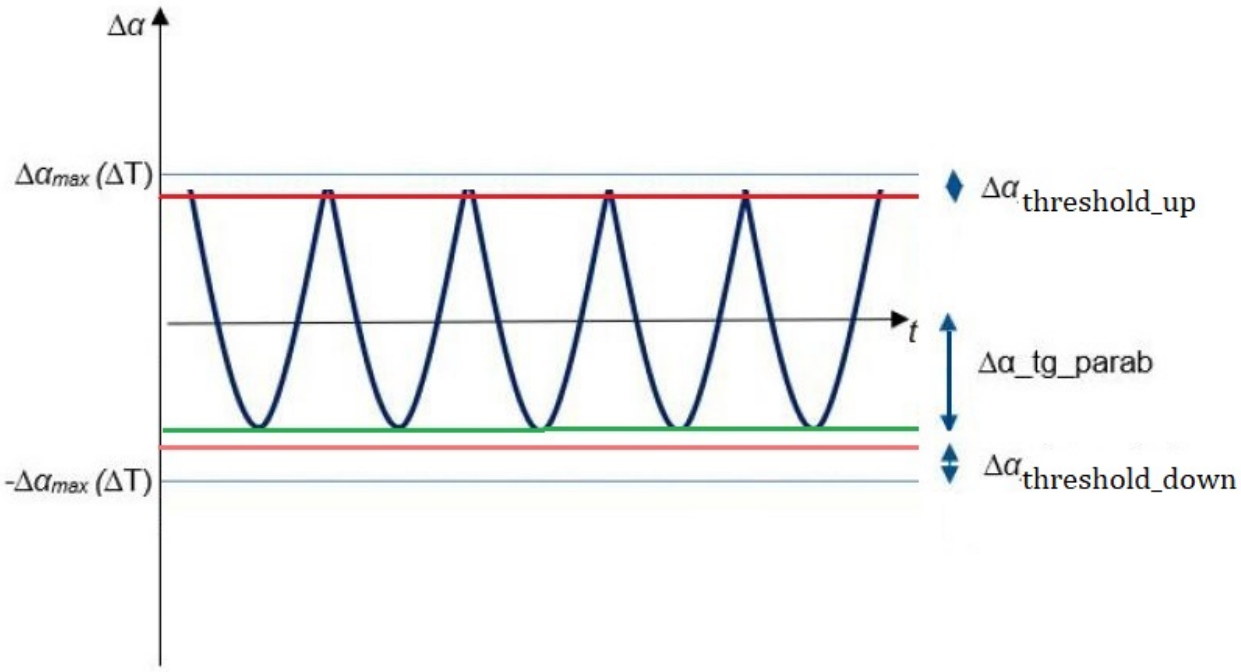

Fig. 2.8: Control margins for the semi-major axis controller [20]

2.1.4 Manoeuvres slots

Manoeuvres can be performed only in determined time slots. They are defined according to mission constraints. First of all, the mission has the priority and must not be constrained by station keeping operations. Moreover, the slots depend also on system constraints; for example, it is necessary to avoid the solar glare of optical instruments or thrust on eclipse for electrical thrusters. This kind of constraint imposes an important limitation to manoeuvre opportunities.

2.2 The AOC algorithm

The AOC is activated at each ascending node of the orbit. In this way the 2D guidance orbit which depends on both the argument of the latitude and the longitude of the ascending node, becomes 1D. Once activated, AOC computes the future necessary station keeping manoeuvres. The collisions management requires an accurate knowledge of the satellite position within 12 and 24 hours, which implies to define the manoeuvres plan in advance. To fulfill this objective, at each activation, AOC divides the future temporal line into three intervals: in chronological order, these are the frozen horizon, the semi-frozen horizon and the research horizon. The frozen horizon and the semi-frozen horizon belong to the predictable horizon, which includes the manoeuvres calculated at previous AOC activations: the frozen horizon ones cannot be modified; the semi-frozen horizon ones can be modified only in magnitude, in order to handle unpredictable variations of the satellite dynamics, mainly due to the solar activity. The research horizon is the following time interval analysed in order to calculate the eventual necessary future manoeuvres: these lasts can become the next semi-frozen manoeuvres.

At each activation the algorithm performs the following steps:

1. It measures the deviations of the measured orbit at the node with respect to the guidance orbit: Δe_X, Δe_Y, $\Delta\Omega$ and $\Delta\alpha$ are determined. Exploiting the past stored deviations, and assuming simple linear or quadratic trends, also the derivatives are determined by means of a polynomial fitting: the evolution of Δe_X, Δe_Y and $\Delta\Omega$ are considered linear; the evolution of $\Delta\alpha$ is considered parabolic. So $\Delta\dot{e}_X$, $\Delta\dot{e}_Y$, $\Delta\dot{\Omega}$, $\Delta\dot{\alpha}$ and $\Delta\ddot{\alpha}$ are estimated.

2. Exploiting the measured and estimated data and in particular assuming that $\Delta\dot{e}_X$, $\Delta\dot{e}_Y$, $\Delta\dot{\Omega}$ and $\Delta\ddot{\alpha}$ are constant, an analytic propagation is conducted along the frozen horizon to obtain the satellite state after this interval. Of course, the effect of the eventual previously planned manoeuvres is taken into account.

3. The same operation is done along the semi-frozen horizon. Anyway before performing the propagation, the semi-frozen manoeuvres are updated, by modifying their amplitude. Finally, the satellite state after the semi-frozen horizon is estimated.

4. The analytic propagation is conducted along the research horizon until an imposed threshold is overcome: the limit date before which the next manoeuvre will have to be performed and the type of the next manoeuvre are defined.

5. The next operations done by AOC depend on the determined next manoeuvre type:

   - If it is an out-of-plane manoeuvre: the admitted time slots are analysed in an inverse chronological order from the limit date to the final date of the semi-frozen horizon searching from the optimal one, that is a slot including the optimal argument of latitude. As soon as an appropriate slot is found the research is interrupted.
   - If it is an in-plane manoeuvre: first of all a criterion of evaluation of the manoeuvre is selected. Indeed, this manoeuvre can be performed either with the aim to minimise the effect of the correction on eccentricity or to increase the ΔV (to minimise the number of manoeuvre). At the limit date a value of Δe_{man} (equation (2.40)) is estimated and compared to the current value of Δe: if the number of manoeuvre to achieve Δe is larger than a threshold value n, $\Delta e > n\Delta e_{man}$, AOC will search for a manoeuvre optimising the eccentricity correction. Once established the criterion, the slots are analysed in chronological order until the limit date. The manoeuvres calculated at the different slots are evaluated according to the selected criterion and the best one is chosen. If no slot is found before the limit date, the research continues after it: the first acceptable manoeuvre is selected, independently on the implied eccentricity correction.

6. The selected manoeuvre is evaluated according to the propulsion system constraints: the ΔV has to be included between a minimum and maximum. If this is not the case, it is discarded.

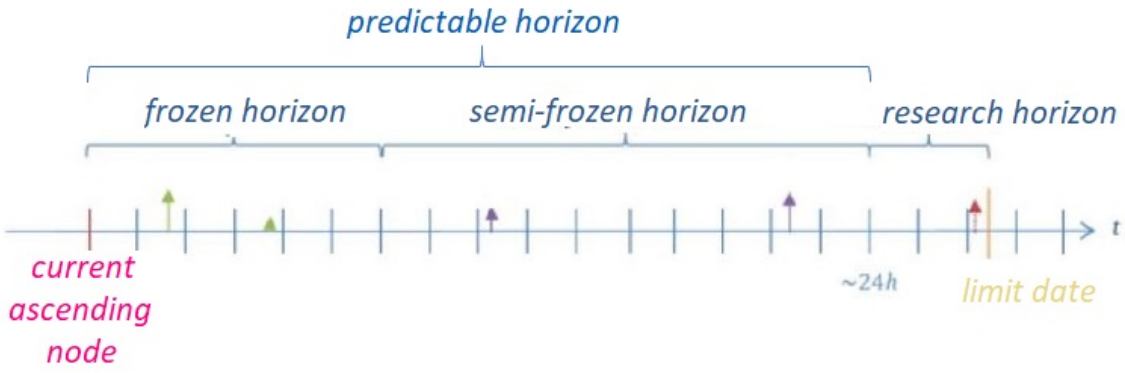

Fig. 2.9: Predictable horizon

7. If the date of the selected manoeuvre occurs in the orbital period following the semi-frozen horizon, it becomes a semi-frozen manoeuvre; otherwise, it is discarded.

In orbit, at each ascending node when AOC is activated, the satellite navigation system will measure the deviations Δe_X, Δe_Y, $\Delta\Omega$ and $\Delta\alpha$. In the simulator, they are determined by performing a numerical propagation which takes into account all the natural perturbing forces. The numerical propagation gives a very fine estimation of the orbital parameters so these last ones can be assumed as real. However, the numerical propagation is very expensive from a computational point of view: an on-board computer would not be able to perform it. This is the reason why the part of the algorithm that predicts the orbit evolution to calculate the future manoeuvres, which is the one that will characterise the on-board controller, exploits an analytic propagation.

Frozen and semi-frozen horizons

As already explained the semi-frozen horizon is conceived in order to reduce the effects of the unpredictability of the solar activity. Not only it allows to modify the already designed manoeuvres magnitude, but it gives the possibility to force the introduction of the so-called *opportunity manoeuvres*. These lasts are null in-plane manoeuvres, introduced according to the solar flux intensity at the AOC activation. More precisely, they are imposed if the time spent from the last inclusion of a manoeuvre in the semi-frozen horizon is longer than a reference time, which depends on the solar flux. In this way they could eventually be exploited in future to hinder the solar activity. In particular, the ooportunity manoeuvres are of the type sma-up: if eventually a ΔV is necessary, it is always positive.

When semi-frozen, the manoeuvres amplitude can be modified without respecting the propulsion system constraints. Only when the considered manoeuvre occurs within the first orbit after the frozen horizon, these constraints are considered; indeed, in this case the semi-frozen manoeuvre becomes frozen.

The temporal length of frozen and semi-frozen horizons (expressed in number of orbits) are control parameters to impose. To increase the predictability, the ideal solution would give a frozen horizon as longer as possible and a semi-frozen horizon as shorter as possible, while respecting the station keeping threshold. Moreover, the total predictable horizon should be almost 24 h long.

2.3 Electric propulsion system

A strategy to perform manoeuvres assuming an electrical propulsion system is also implemented.

The electric manoeuvre is conceived as a degraded impulsive manoeuvre, because of the time needed to reach the desired ΔV: an efficiency $\widehat{\rho}$ is introduced. By considering the Newton second law, the

thrust is:

$$F = m\frac{dV}{dt} \tag{2.41}$$

With respect to Figure 2.10, it is possible to determine the effective imposed ΔV, ΔV_{real}:

$$\Delta V_{real} = \int_{-\alpha_{start}}^{\alpha_{end}} \frac{F}{m}\cos u du\frac{dt}{du} = \frac{F}{m}(\sin\alpha_{end} - \sin\alpha_{start})\frac{\Delta V_{impulsive} m}{F}\frac{1}{\alpha_{end} - \alpha_{start}} \tag{2.42}$$

$$\Delta V_{real} = \Delta V_{impulsive}\frac{(\sin\alpha_{end} - \sin\alpha_{start})}{\alpha_{end} - \alpha_{start}} \tag{2.43}$$

As consequence, we obtain:

$$\widehat{\rho} = \frac{(\sin\alpha_{end} - \sin\alpha_{start})}{\alpha_{end} - \alpha_{start}} \tag{2.44}$$

The efficiency is an user defined parameter: it depends on the assumed electric propulsion system. Considering the reduced ΔV_{real} with respect to the desired $\Delta V_{impulsive}$, it can be understood that the searched ΔV_{elec} will be larger:

$$\Delta V_{elec} = \frac{\Delta V_{impulsive}}{\widehat{\rho}} \tag{2.45}$$

In order to model the electric manoeuvres, other relations are considered, based on equation 2.41 and the Tsiolkowski law:

$$\Delta m = m_{initial}(1 - e^{-\frac{\Delta V_{elec}}{gI_{SP}}}) \tag{2.46}$$

The following hypothesis are assumed:

- constant value of the thrust F and constant mass flow $\dot{m}$
- constant specific impulse I_{SP}
- $\Delta V_{elec} << gI_{SP}$

So the mass consumption to achieve a given ΔV_{elec} is:

$$\Delta m = m_{initial}\frac{\Delta V_{elec}}{gI_{SP}} \tag{2.47}$$

and the time required is

$$\Delta t = \int_{m_{initial}}^{m_{final}} -g\frac{I_{SP}}{T}dm = \frac{I_{SP}}{F} = \frac{m_{initial}\Delta V_{elec}}{F} \tag{2.48}$$

This relation is exploited in order to determine the largest value of ΔV_{elec} that can be imposed: $\Delta V_{achievable}$. Once established the available time to perform the manoeuvre, assuming the same hypothesis already introduced and that the satellite mass is constant along one orbit, $\Delta V_{achievable}$ is computed. Of course, its determination takes into account also the thrust system limitations: it has to be between the minimum and the maximum, that the propulsion system is able to provide.

The strategy to introduce electric manoeuvres is conceived as an extension of the strategy adopted for the impulsive manoeuvres. The electric manoeuvre is considered as an impulsive manoeuvre spread in time, as a certain time is necessary in order to get the desired ΔV value. The required time is too long to be achieved in one only slot; for this reason, several slots along one orbit have to be used. When the next future required manoeuvre type is established, the slots analysis starts: the algorithm takes into account all the slots included between the final date of the predictable horizon and the limit date and stores those which would allow an acceptable impulsive manoeuvre. These slots are sorted according to a defined criterion (the one already described for the in-plane manoeuvres; the date in case of out-of-plane manoeuvres). Moreover, the computed impulsive manoeuvres associated to the slots are modified according to the efficiency $\widehat{\rho}$, in order to get ΔV_{elec} from $\Delta V_{impulsive}$. Finally, the best manoeuvre is selected and its $\Delta V_{bestman}$ is spread among the sorted slots, as much as possible

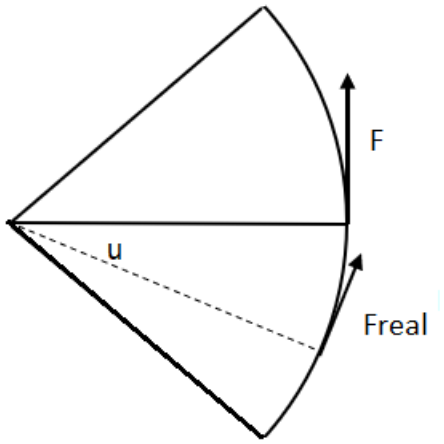

Fig. 2.10: Electrical thrust as degraded impulsive thrust

depending on the available time. This last one depends on the slots length and on the optimal argument of latitude at which the manoeuvre should be performed. The sorted slots are considered one after the other: the manoeuvres are planned at each of them until the sum of the achievable $\Delta V_{achievable}$ becomes equal to ΔV_{best_man} or they terminate.

2.4 AOC: analysed missions and control parameters

Previous studies have determined the optimal parameters to be imposed according to the analysed mission in order to obtain the best performance consisting in the best compromise between station keeping requirements and the most extended predictable horizon. Moreover, the parameters allowing to respect the imposed thresholds with the smallest number of manoeuvres have been selected. The main among these control parameters are:

- the number of frozen orbits;
- the number of semi-frozen orbits;
- the control margins $\Delta\Omega_{threshold}$, , $\Delta\alpha_{threshold\_up}$ and $\Delta\alpha_{threshold\_down}$;
- $\Delta\Omega_{tg\_parab}$, $\Delta\alpha_{tg\_parab}$;
- the number n of manoeuvres leading the criterion choice for the in-plane manoeuvres.

In table 2.3, the considered missions are recorded. Among them, mission A1 and mission A2 coincide except for the solar activity. Then, what changes between mission D2 and D3 is the length of the predictable horizon, longer for the first one.

In table 2.4, the objectives to achieve in terms of station keeping performance for each mission are shown. The performance is expressed as the annual percentage of the mission time during which the satellite is successfully kept inside specific station-keeping window, identified by means of a threshold S. In particular, for the in-track orbital control, two deviation values, $S1$ and $S2$, are taken into account: for each of them a different targeted station keeping percentages are specified.

2.5 Internship work

The state of the art before the internship has been described. At this point, it is possible to observe that one limit of AOC is the impossibility to perform concurrently an in-track station keeping manoeuvre

and a cross-track one. Either an out-of-plane manoeuvre or an in-plane manoeuvre can be computed and mixed manoeuvres, which are manoeuvres with a $\mathbf{\Delta V}$ characterised by both a normal and a tangent component, are not taken into account. This is one of the main reason that causes the non-respect of the thresholds, above all in case of very low thrust due to electrically-powered satellite propulsion.

The objective of this work is to integrate the algorithm to allow mixed manoeuvre, both considering chemical and electric propulsion systems.

Finally, a study has been started in order to determine a semi-analytic model of the inclination drift di/dt, necessary for the computation of the out-of-plane manoeuvres. The aim is to obtain a sufficiently accurate estimation of this parameter in such a way to minimise also the required computational time.

Table 2.3: Analysed Missions (SSO points a sun synchronous orbit)

Name	Mission type	Altitude	i	Local time	trace	Mode propulsion	solar activity
A1	Constellation observation	470 km	SSO	10:30	15+8/27	chemical electric	high
A2	Constellation observation	470 km	SSO	10:30	15+8/27	chemical electric	medium
B1	Optical/Radar Imaging	689 km	SSO	10:30	14+19/32	chemical	high
B2	Optical/Radar Imaging	689 km	SSO	06:00	14+19/32	chemical	high
C	Earth observation	689 km	10 deg	-	14+19/32	electric chemical	high
D1	Scientific environment	800 km	SSO	22:00	14+7/27	chemical electric	high
D2	Scientific environment	800 km	SSO	22:00	14+7/27	chemical electric	Low
D3	Scientific environment	800 km	SSO	22:00	14+7/27	electric	Low
E	Telecom	1200 km	88 deg	-	13+4/39	chemical electric	High
F	Altimetry	1336 km	66 deg	-	12+7/10	chemical	High

Table 2.4: Missions Constraints

mission	ΔT - S1	ΔT - S2	ΔW - S
A1	98%	100%	100%
A2	98%	100%	100%
B1	98%	100%	100%
B2	98%	100%	100%
C	98%	100%	100%
D1	98%	100%	100%
D2	98%	100%	100%
D3	98%	100%	100%
E	98%	100%	100%
F	98%	100%	100%

Chapter 3

Impulsive Mixed In-track Cross-track Manoeuvres

3.1 Interest in mixed in-track cross-track manoeuvre

The integration of mixed in-track cross-track manoeuvres is useful for two main reasons. First of all, they allow to perform both in-track and cross-track corrections simultaneously. This is necessary above all in the case of low-thrust propulsion, for which the occurrence and spreading of needs of both in-track and cross-track corrections require performing these lasts on the same orbit. Then, mixed manoeuvres are convenient for fuel saving. A mixed manoeuvre ΔV will be always inferior than the sum of two distinct necessary in-plane and out-of-plane manoeuvres ΔV:

$$\sqrt{\Delta V^2{}_{in-plane} + \Delta V^2{}_{out-of-plane}} < |\Delta V_{in-plane}| + |\Delta V_{out-of-plane}|$$

Moreover, an out-of-plane manoeuvre may also have an effect on the semi-major axis: it induces its positive variation. Indeed, as it can be observed from Figure 3.1, the manoeuvre changes both the direction and the magnitude of the satellite velocity vector. Thus, mixed manoeuvres are convenient when both a variation of the inclination and a positive variation of the semi-major axis are required. AOC algorithm is modified to introduce mixed manoeuvres if such a situation shows up, keeping the so called *sma-down* manoeuvres independent.

This chapter is about the integration of mixed manoeuvres in case of a chemical propulsion system. The next chapter (Chapter 4) concerns the case of an electric propulsion system.

3.2 Strategy

The impulsive mixed manoeuvres are introduced in such a way not to modify the working principles of the AOC algorithm. The algorithm works as before: only if both an inclination (or right ascension of the ascending node) and a semi-major axis corrections are necessary, mixed manoeuvres are computed in place of the standard in-plane and out-of-plane manoeuvres. This means that, only if, at the limit date of the research horizon the variations to impose to the $\Delta\Omega$ and $\Delta\alpha$ drifts, $\Delta\dot{\Omega}_{comm}$ and $\Delta\dot{\alpha}_{comm}$, are not null (in particular, $\Delta\dot{\alpha}_{comm}$ is such that the Δa to be imposed is positive), mixed manoeuvres are evaluated.

The same models and strategies adopted for the computation of the standard in-plane and out-of-plane manoeuvres are used as inspiration for the new manoeuvres conception.

The dimensioning of station-keeping window implies Δi corrections that are less frequent but larger than Δa corrections. Thus, the algorithm behaviour is such that these manoeuvres are delayed as much as possible until the most suitable slot is found. This strategy is efficient; thus, it is maintained and exploited also for the mixed manoeuvres integration, as done also by [21]. Mixed manoeuvres are conceived as an extension of the out-of-plane manoeuvres. Once a required out-of-plane manoeuvre

is determined, the need for a semi-major axis correction is evaluated and a tangent component is eventually added. In this case, the evaluated $\Delta\mathbf{V}$ in-plane component, ΔV_T, is reduced according to the variation of the semi-major axis due to the out-of-plane component, ΔV_N:

$$\Delta V_{T_{induced}} = \sqrt{V_{initial}^2 + \Delta V_N^2} - V_{initial} \tag{3.1}$$

$$\Delta a_{induced} \sim 2a \frac{\Delta V_{T_{induced}}}{V_{initial}}$$

Thus, the imposed value is :

$$\Delta V_T = \Delta V_{T_{required}} - \Delta V_{T_{induced}} \tag{3.2}$$

The average value of the guidance orbit velocity is taken as value of $V_{initial}$.

In order to avoid glare risks, the mixed $\Delta\mathbf{V}$ direction is subjected to limitations: the $\Delta\mathbf{V}$ inclination with respect to the orbital plane has to be into an admitted range. This last one depends on the mission characteristics like the largest admissible angle between an optic instrument and the Sun direction. Evidently, it depends also on the satellite position with respect to the Sun (eventually also with respect to the Moon). Since the out-of-plane component ΔV_N is fixed, this results in a limitation of ΔV_T: $\Delta V_T \in [0; \Delta V_{T_{max\_glare}}]$. In Chapter, 5 the technique to determine $\Delta V_{T_{max\_glare}}$ is described. There exists also a limitation linked to the propulsion system, related to a maximum, ΔV_{max_propu}, of the ΔV that can be practically imposed. Thus, the added in-plane component has to be smaller than $\Delta V_{T_{max\_propu}} = \sqrt{\Delta V^2{}_{max\_propu} - \Delta V^2{}_N}$. In conclusion ΔV_T has to be smaller or equal to a maximum, $\Delta V_{T_{max}}$, which is computed as:

$$\Delta V_{T_{max}} = min\left(\Delta V_{T_{max\_propu}}, \Delta V_{T_{max\_glare}}\right)$$

The possibility of mixed manoeuvre is not the only change done. The new algorithm gives also the capability to plan more than one manoeuvre along one same orbital period, combining a standard out-of-plane manoeuvre with an in-plane manoeuvre or a mixed manoeuvre with an in-plane manoeuvre. So, if the need of a mixed manoeuvre is detected, the algorithm can compute four possible results:

- a mixed manoeuvre;
- a mixed manoeuvre and a standard in-plane manoeuvre;
- a standard out-of-plane manoeuvre and a standard in-plane manoeuvre;
- a standard out-of-plane manoeuvre, if no in-plane manoeuvre is found.

The new algorithm integration behaviour is described more in detail in the next section.

3.3 New algorithm

As first step, the algorithm determines the limit date of the research horizon, before which a manoeuvre has to be performed to avoid that the imposed thresholds are not crossed. At this date, the need of a mixed manoeuvre is checked. When the most urgent manoeuvre is an out-of plane one, a mixed manoeuvre will be considered necessary if, at the limit date, also a positive semi-major axis variation is required; similarly, when a positive in-plane manoeuvre is the most urgent, the need is identified if, at the limit date, an inclination correction is required. At this point, the algorithm performs the following steps:

1. The criterion of evaluation of the manoeuvres is selected, following the same convention of the in-plane manoeuvre: a mixed manoeuvre will be selected to maximise either ΔV_T or the eccentricity correction.

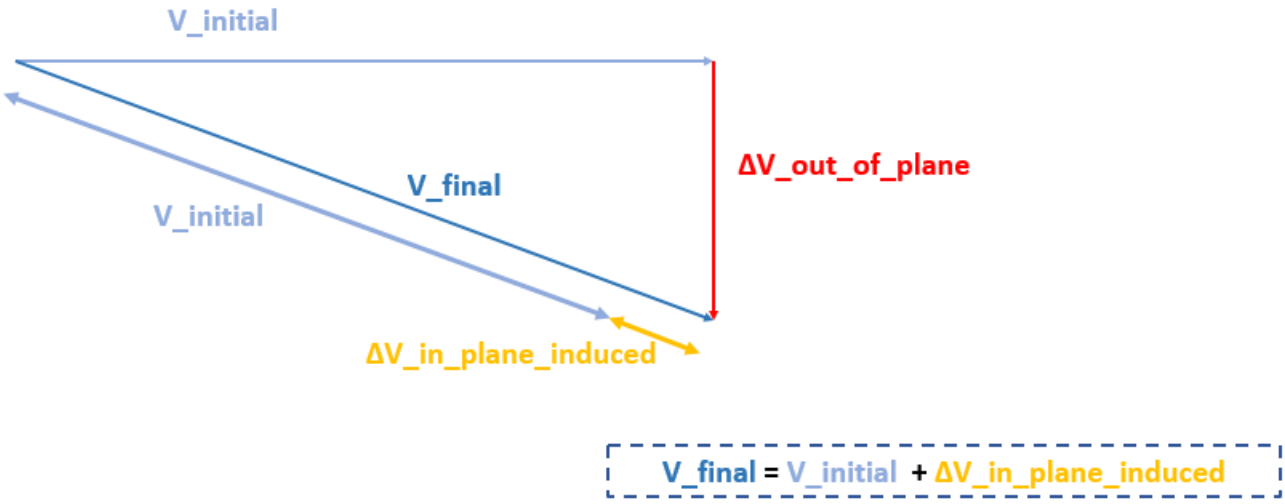

Fig. 3.1: An out-of-plane manoeuvre doesn't implies only an inclination variation but also a semi-major axis variation

2. All the possible out-of-plane manoeuvres in the research horizon are calculated. Each manoeuvre can be potentially converted into a mixed manoeuvre, by adding an in-plane component to the computed $\Delta\mathbf{V} = \begin{bmatrix} 0 \\ 0 \\ \Delta V_N \end{bmatrix}$. In case no out-of-plane manoeuvre is found and the most urgent manoeuvre is an in-plane manoeuvre, the algorithm works as the original one, searching for a standard in-plane manoeuvre.

3. For each out-of-plane manoeuvre found, the largest addable in-plane component value, $\Delta V_{T_{max}}$, is determined.

4. For each out-of-plane manoeuvre found, the eventual necessary semi-major axis correction is computed. Thus, the required in-plane component ΔV_T is determined. If ΔV_T is different from zero and it is smaller than $\Delta V_{T_{max}}$, then the out-of-plane manoeuvre is transformed into a mixed manoeuvre:

$$\Delta\mathbf{V} = \begin{bmatrix} \Delta V_T \\ 0 \\ \Delta V_N \end{bmatrix}$$

   On the contrary, the research horizon is investigated again in order to find an eventual standard in-plane manoeuvre that can be exploited to impose the required semi-major axis correction. If several manoeuvres are found, only one is selected according to the previous determined criterion. In the case the most urgent manoeuvre is an out-of-plane one, only a portion of the research horizon is investigated: the time interval following the analysed out-of-plane manoeuvre date. On the contrary, if there is an urgent need of an in-plane manoeuvre, all the horizon is explored; in this case, the value of the analysed out-of-plane manoeuvre is updated to take into account the orbit variation due to the eventually selected in-plane manoeuvre. It is also checked if it is possible to transform the out-of-plane manoeuvre into a mixed manoeuvre to combine with the in-plane manoeuvre.

5. Once the two previous operations are executed for each found out-of-plane manoeuvre, the manoeuvre or the combination of manoeuvres to be imposed is chosen according to the selected criterion.

The new integration behaviour, which has been described, is schematised in Figure 3.2: a kind of flow chart is shown. The arrows link an operation to the successive one. The yellow windows concern

the preliminary steps, from the selection of the research horizon limit date to the determination of the manoeuvres selection criterion. The light blue windows are relative to all the following steps, about the manoeuvres computation. More specifically, all the windows inside the largest blue box are the operations effectuated for each out-of-plane manoeuvre found.

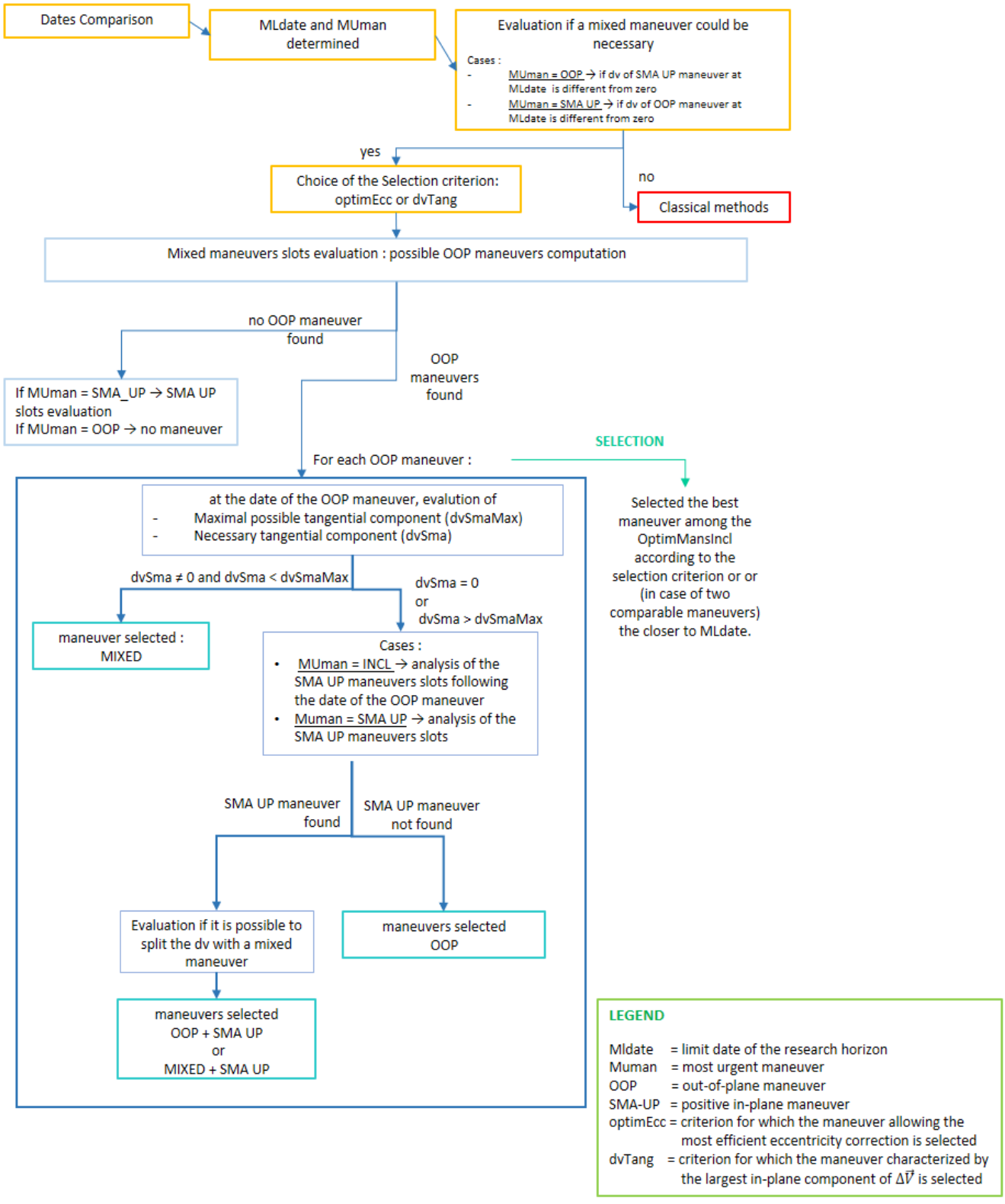

Fig. 3.2: Mixed manoeuvres integration: algorithm behaviour scheme

3.4 Analysis of the results: comparison with the original algorithm

Once effectuated the integration, a series of simulations are carried out, by exploiting the missions introduced in Section 2.4 and described in Table 2.3. All the missions are characterised by low-Earth orbits, with altitudes between 470 km and 1340 km. Among them, only three orbits are not sun-synchronous.

As explained in Section 2, to test the algorithmic control method, AOC, the real orbital dynamics is simulated by means of a numerical propagation, which consequently provides all the measures that would be obtained by a navigator on-board. The standard already implemented numerical simulator exploited at CNES has been used. Each simulation covers a period of one year.

The simulations show that, in comparison with the original algorithm, the controller has a larger efficiency. Either the performance improves or the in-track station keeping and cross-track one result to be more balanced. Indeed, even though the first deteriorates little, the other improves or vice-verse (like in missions B1, D2 and F). There are just two missions for which the mixed manoeuvres seem not to have a positive influence: missions A1 and A2. The cross-track station keeping is almost unchanged, while the in-track one gets worse. Anyway, these two missions are the most complex to handle since they are characterised by low orbit highly affected by the atmospheric drag. Moreover, a general analysis of the missions show that the cause of the performance degradation is not an incorrect evaluation of the mixed manoeuvres. All the missions behaviour depends on a series of parameters, set in order to optimise the performance, as explained in Section 2.4. The integration of mixed manoeuvres modifies the algorithm behaviour: the parameters have to be adjusted in order to find the new optimal configuration. The conducted optimisation is focused only on some selected parameters, which have the largest influence on the performance: the control variables $\Delta\Omega_{threshold}$, $\Delta\Omega_{tg\_parab}$, $\Delta\alpha_{threshold\_up}$ $\Delta\alpha_{threshold\_down}$ and $\Delta\alpha_{tg\_parab}$. The predictable research horizon length is left unchanged in order to verify that mixed manoeuvres can allow a better performance for the same AOC predictable capacity. More details about the performed optimisation are explained in Section 3.5.

In the case of mission A2, an additional problem arises. It is linked to the negative in-plane manoeuvres: an excessive delay in their execution, due to the unpredictable solar activity effects, degrades the performance. For this reason, a further algorithm modification is done, which is the possibility to introduce negative opportunity manoeuvres: these manoeuvres are of type *sma-down*, so they are such that their magnitude can become negative.

After the optimisation process and the introduction of the *sma-down* opportunity manoeuvres, the simulations are repeated with new control margins.

All the outcomes are shown in Tables 3.1 - 3.9. The performance obtained with the new algorithm, before and after the optimisation process, is compared to the performance obtained with the original algorithm. As already introduced in Section 2.4, the performance is expressed in terms of annual percentage of the mission time during which the satellite doesn't cross a cross-track threshold S and two in-track thresholds S1 and S2, with S1 $<$ S2. The outcomes show also the distance of the largest in-track and cross-track deviations with respect to the associated thresholds, respectively S and S2: this quantity is negative if the threshold is never crossed during one year. Moreover, the trends of the in-track and cross-track deviations, obtained after the optimisation process, are shown: in the figures, the blue lines show the evolution of the deviations measured at the orbital ascending nodes; the red lines are referred to all the other orbital points. In the figures, it is possible to observe eventually also the lines associated to the thresholds.

The new and original algorithms comparison in terms of performance is summarised in Figure 3.3. After the optimisation process, the performance improves. For five missions the in-track station keeping annual percentage increases; for six missions the cross-track station keeping annual percentage increases. For seven missions, the largest in-track deviations over one year decreases; for eight missions, the largest in-track deviations over one year decreases. For six missions the total ΔV decreases; for the other three missions it increases but not in a significant way. In the case of missions B1 and C, the small increase of the cost is justifiable considering the important improvement of the performance.

The only mission for which performance is not satisfying is mission A2. The problem is linked to the difficulties of the algorithm to predict the necessary standard positive in-plane manoeuvres in a period of high variation of the solar activity (Figures 3.4, 3.5).

In general, the obtained results are good and demonstrate the advantage of the mixed manoeuvres. In some cases (see missions D1, D2 and F), they allow to fulfill the missions constraints.

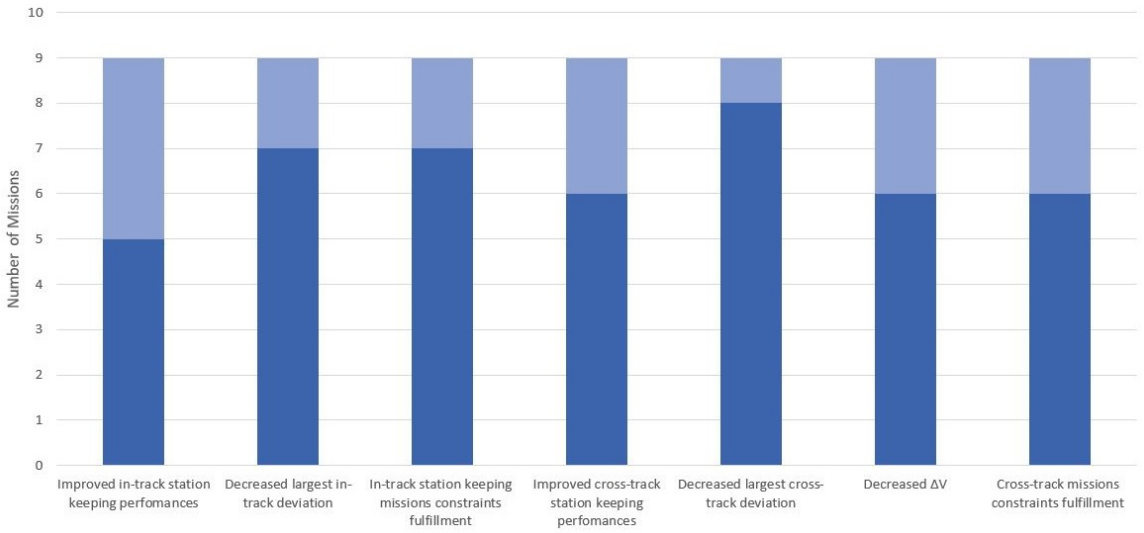

Fig. 3.3: Impulsive mixed manoeuvres integration outcomes

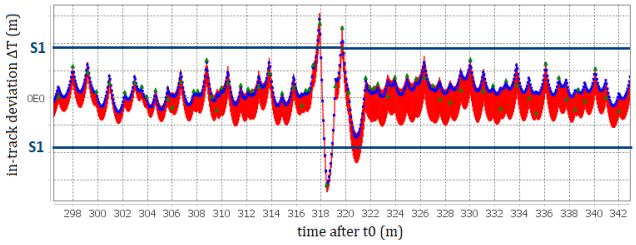

Fig. 3.4: Mission A2 - cross of the in-track station keeping threshold

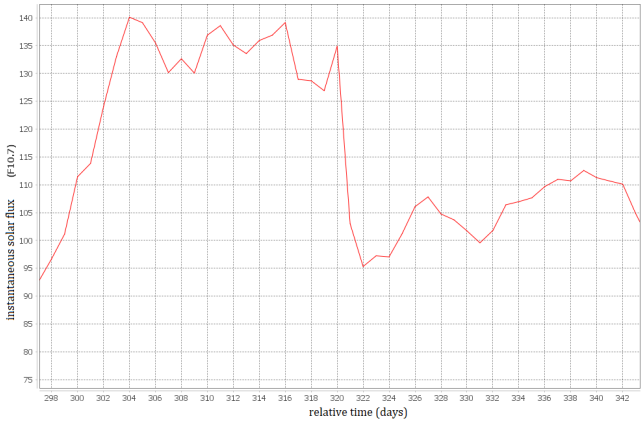

Fig. 3.5: Mission A2 - solar activity at the crossing of the in-track station keeping threshold

3.5 Optimiser

In order to maximise the station keeping performance (defined in Section 2.4), five variables are modified for each mission: $\Delta\Omega_{threshold}$, $\Delta\Omega_{tg\_parab}$, $\Delta\alpha_{threshold\_up}$ $\Delta\alpha_{threshold\_down}$ and $\Delta\alpha_{tg\_parab}$. These lasts are the control margins that trigger the manoeuvres and impact their magnitudes: they have been described in Sections 2.1.2 and 2.1.3. Even though they are not the only control parameters affecting the missions behaviour, they are those to which this last is more sensible. The optimisation problem to consider is multiobjective. Indeed, good performance coincides with the following objectives:

1. to maximise the time percentage of correct in-track station keeping;

2. to maximise the time percentage of correct cross-track station keeping;

3. to minimise the maximum in-track deviation;

4. to minimise the maximum crossed-track deviation;

5. to minimise the total energy cost.

To evaluate the in-track station keeping three different spatial boxes are considered: a smaller, a medium and a larger. In the case of cross-track station keeping, the boxes are two. So five percentages are to be considered. The cost function is written as a linear combination of the cost function associated to each objective:

$$f(\Delta\Omega_{limit}, \Delta\Omega_{tg\_parab}, \Delta\alpha_{limit\_up}, \Delta\alpha_{limit\_down}, \Delta\alpha_{tg\_parab}) = k_1 f_{o_1} + k_2 f_{o_2} + k_3 f_{o_3} + k_4 f_{o_4} + k_5 f_{o_5}$$

where the $k_1 ... k_5$ are constants settled to impose the same weight to the first four objectives, and a smaller weight to the last objective: the fulfillment of the missions constraints has the priority over the minimisation of the total ΔV. Moreover, the cost function is built in order to have a minimisation problem. Indeed, f_{o_1} and f_{o_2} are written as:

$$f_{o_{1,2}} = \sum \frac{1}{percentage}$$

In this way, higher percentages imply a smaller cost function.

An optimiser already avaiable in Java is used: it is based on the *covariance matrix adaptation evolution strategy* (CMA-ES). The brief description of this method is reported in Appendix A. The optimiser is global, so it would be capable to determine the global minimum over the whole problem domain. However, this last is reduced so that the optimiser has to investigate only a reduced portion of it. This is done for two main reasons. Before the mixed manoeuvres integration, an optimisation process had been already realized and consequently small adjustments of the parameters are sufficient. The second reason is linked to the computation process. Each evaluation of the cost function implies the execution of the AOC algorithm. In some cases, it is sufficient to simulate a small period. However some missions optimisation requires the simulation of a significant time period. In any case, the optimisation process is very expensive in terms of both computational time and cost. This is also the reason only the five most significant parameters are considered as variables of the problem. If an entire optimisation process has to be done, it is recommended to perform a parametric study such the one done in [20] in order to determine the domain region of the optimum and then to execute the described optimisation process.

3.6 Analysis of the algorithm behaviour

After the optimisation process, the conducted simulations (described in Section 3.4) show two main trends in the algorithm behaviour:

- mixed manoeuvres are usually computed when there is an urgent need of performing a right ascension of the ascending node trend correction, which is perfectly coherent with the way they are conceived, as modified out-of-plane manoeuvres; this is also linked to the algorithm characteristic of delaying out-of-plane manoeuvres until the most suitable slot is found;

- when the need of a mixed correction is detected, the manoeuvres, the most frequently selected by the algorithm, are mixed manoeuvres. Indeed, they allow small semi-major axis corrections, which would be impossible to perform by means of a standard in-plane manoeuvre: the propulsion system can not provide a ΔV smaller than a certain limit. In terms of selection frequency, they are followed by the combination of an in-plane manoeuvre and an out-of-plane manoeuvre.

The results obtained in terms of performance highlight the correct behaviour of AOC. Figures 3.6-3.14 show the free evolution of the missions orbits under the effects of perturbations: no orbital control is performed. The geopotential, the three body effect, the solar radiation pressure, the atmospheric drag and the terrestrial tides are taken into account. The deviations of the orbital parameters with respect to the reference orbit ones are represented. In particular, the blue points are referred to the orbital parameters deviations at the orbital nodes; the red points are relative to all the other orbital points.

In the case of mission A1, the manoeuvres associated to the in-track station keeping are significantly larger in number of those aimed to correct the right ascension of the ascending node trend: the ratio is $1 : 0.006$. This outcome is consistent with the perturbations effects on the orbit. This last one has a nominal altitude of 470 km so it is highly subjected to the atmospheric drag. This perturbation, which has important effects for altitudes lower than 1500 km, is preponderant up to 600 km [16]. Moreover, mission A1 is subjected to an high solar activity, which increases the effects of the atmospheric drag and the solar radiation pressure. Focusing on mission A2, which is equal to the mission A1 except for its lower solar activity, the argument of latitude free deviation is reduced of more than one half; coherently, the manoeuvres ratio is $1 : 0.016$ and the in-track station keeping performance is higher.

Missions B1 and B2 have an altitude such that the atmospheric drag influence is significantly reduced. The largest free semi-major axis and argument of latitude deviations reached in 35 days would be 1000 m and 4°, against the values of 8000 km and 35° of the mission A2. This determines a lower number of in-track executed corrections. For mission B1 the manoeuvres ratio is $1 : 0.021$; for mission B2 it is $1 : 0.459$. Indeed, mission B2 has a largest need of cross-track station keeping manoeuvres than mission B1: its right ascension of the ascending node free deviation is more important, being characterised by a dawn orbit. A dawn orbit is a sun-synchronous orbit whose local mean time for passages at the equatorial latitude is around sunrise (6 h). For dawn orbits the effect of solar potential on the right ascension of ascending node is more significant. The solar potential usually determines long period variations of the orbital inclination, right ascension of the ascending node and argument of latitude. In the particular case of sun-synchronous orbits, it has secular effects on the inclination and the right ascension of the ascending node. In first approximation, the secular drifts are expressed as:

$$\frac{di}{dt} \sim \frac{3\pi}{2} \frac{T_0}{T_{SO}^2} \sin i \cos^4 \frac{i_{SO}}{2} \sin\left(4\pi\left(\frac{H}{T_E} - \frac{1}{2}\right)\right) \tag{3.3}$$

$$\frac{d\Omega}{dt} \sim \frac{3\pi}{2} \frac{T_0}{T_{SO}^2} \cos i \left(\left(\cos^4 \frac{i_{SO}}{2} \cos\left(4\pi\left(\frac{H}{T_E} - \frac{1}{2}\right)\right)\right) + \frac{3}{2} \sin^2 i_{SO} - 1\right) \tag{3.4}$$

where the following notations are used:

- T_0 is the orbital period;
- T_{S0} is the period of the apparent solar orbit around Earth;
- i_{S0} is the inclination of the apparent solar orbit around Earth;
- T_E is the Earth rotation period;
- H is the local hour at the ascending node.

For a dawn-dusk orbit (or for orbits whose local hour is 12 h, 18 h and 24 h), there is no secular variation on the inclination (Figure 3.15); indeed, the inclination deviation is larger for mission B1, whose local hour is such that the solar potential imposes an inclination drift near to the maximum possible. On the contrary, the right ascension of the ascending node drift is the maximum obtainable (Figure 3.16), which justifies the larger deviations of this orbital element for mission B2. This is also the reason the performance of mission B1 is higher than that obtained of mission B2.

Also comparing missions D1 and D2, the obtained performance results coherent. The two missions are coincident except for the solar activity which is higher for the first. Indeed, the performance of mission D2, for both the in-track and the cross-track station keeping, is slightly superior. Moreover, the manoeuvres ratios are $1 : 9$ for mission D1 and $1 : 15$ for mission D2: for a comparable number of out-of-plane manoeuvres, the number of in-track station keeping corrections is lower for mission D2.

The analysis carried out until now by comparing missions characterised by sun-synchronous orbits with the same altitude shows the correct behaviour of the algorithm. However, an apparent anomaly emerges if a cross comparison among all the discussed missions is done. At the increase of the orbital altitude, the right ascension of the ascending node free deviations decrease. Nevertheless the number of out-of-plane manoeuvres becomes more important (Figure 3.17). Indeed, the number of out-of-plane manoeuvres computed by the algorithm seems to have a relation of inverse proportionality with the perturbations effects on the argument of latitude. The reason is linked to the algorithm behaviour, which is coherent with the implemented strategy concerning the detection of a mixed manoeuvre need. At the limit date of the research horizon, when the argument of latitude or the right ascension of the ascending node would cross the imposed threshold, there is the possibility that the variation to be imposed to the other orbital parameter trend is not null: only in this case a mixed manoeuvre is considered necessary and it is evaluated. For missions subjected to perturbations highly affecting the argument of latitude, the limit date is closer and closer to the date of beginning of the research horizon and it is farther and farther to the time period when a correction of the right ascension of the ascending node trend should be performed. Thus, in these cases the algorithm very frequently doesn't detect the need of a mixed manoeuvre. On the contrary, lower the perturbations on the argument of latitude, farther in time the limit date: thus, the algorithm has the possibility to detect an out-of-plane manoeuvre or a mixed manoeuvre need. A modification to this strategy is not conceivable. Indeed, even if a mixed manoeuvre was fixed after the limit date it would be imposed as closer as possible to it in order to avoid an excessive threshold crossing: thus, this is the time to take as reference.

There is also another important reason for the observed behavior. Previously, it has been demonstrated that an out-of-plane manoeuvre determines not only a variation of the inclination, but also of the semi-major axis. This is one of the causes why mixed manoeuvres have been integrated in the first place. Thus, an out-of-plane manoeuvre induces an involuntary in-track correction. That is a further reason in addiction to the perturbation effects of the observed trend characterised by the increasing of cross-track station keeping manoeuvres and the decreasing of in-track station keeping ones.

Also the results obtained for mission C are consistent. The mission is comparable to mission B2, as the reference orbit has the same altitude and the perturbations cause similar right ascension of ascending node and argument of latitude free deviations. Indeed, the manoeuvres ratio has the same order of magnitude: $1 : 0.25$. The number of out-of-plane manoeuvres is lower than that of mission B2, but this is linked to the almost equatorial orbit of mission C. Orbits with lower inclinations imply a different method for the out-of-plane manoeuvre evaluation, because of the need to avoid that a pure inclination variation could excessively move it from its reference value. This is also the reason the number of out-of-plane manoeuvres is higher for mission E (30) with respect to mission F (13), whose right ascension of the ascending node free deviations are larger: indeed, mission F orbit inclination is lower.

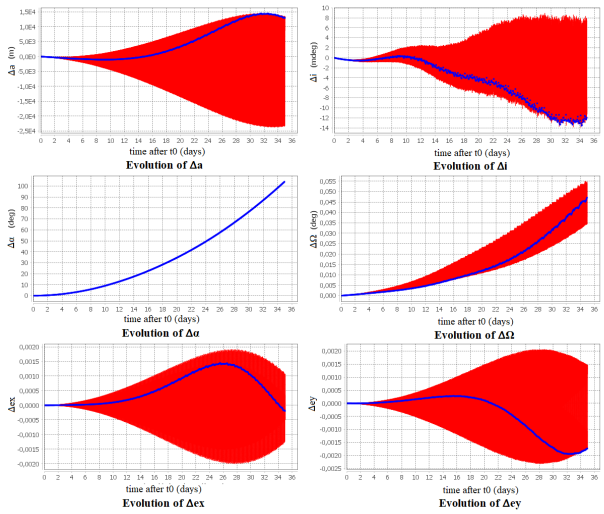

Fig. 3.6: Mission A1 - orbital parameters free evolution. From left to right, from the top to the bottom: Δa [m], Δi [mdeg], $\Delta\alpha$ [deg], $\Delta\Omega$ [deg], Δe_x, Δe_y. Simulated time: 35 days

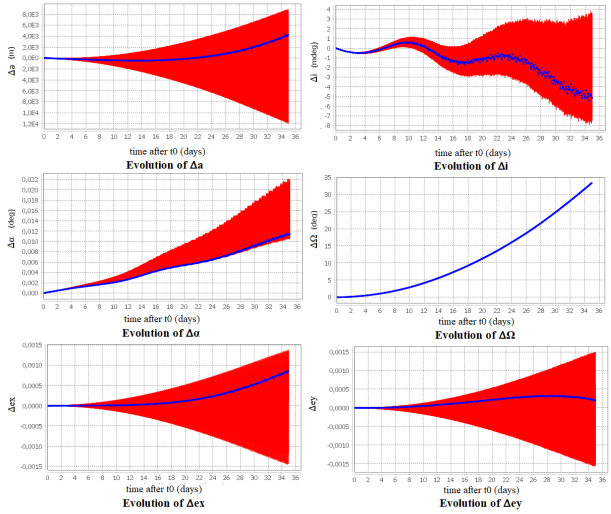

Fig. 3.7: Mission A2 - orbital parameters free evolution. From left to right, from the top to the bottom: Δa [m], Δi [mdeg], $\Delta\alpha$ [deg], $\Delta\Omega$ [deg], Δe_x, Δe_y. Simulated time: 35 days

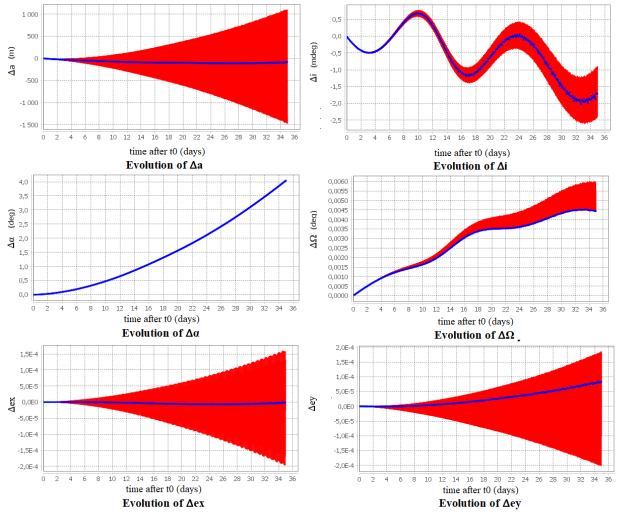

Fig. 3.8: Mission B1 - orbital parameters free evolution. From left to right, from the top to the bottom: Δa [m], Δi [mdeg], $\Delta\alpha$ [deg], $\Delta\Omega$ [deg], Δe_x, Δe_y. Simulated time: 35 days

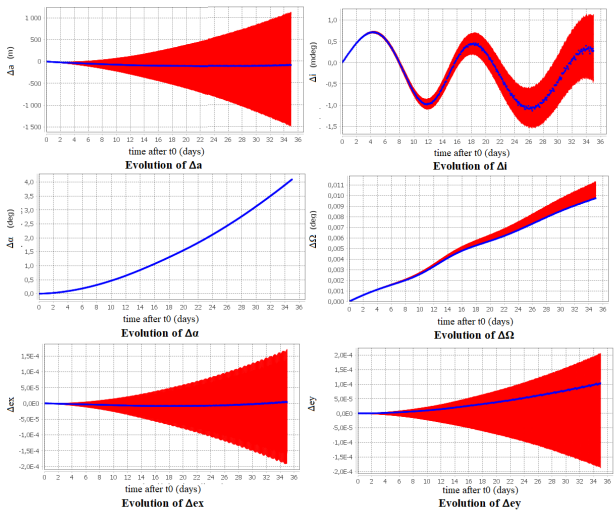

Fig. 3.9: Mission B2 - orbital parameters free evolution. From left to right, from the top to the bottom: Δa [m], Δi [mdeg], $\Delta\alpha$ [deg], $\Delta\Omega$ [deg], Δe_x, Δe_y. Simulated time: 35 days

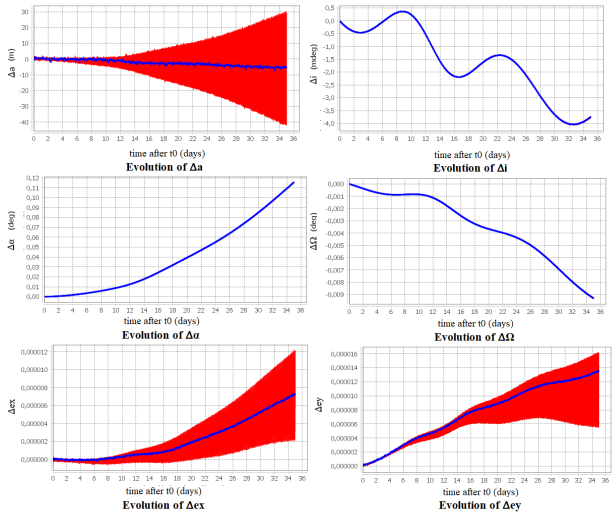

Fig. 3.10: Mission D2 - orbital parameters free evolution. From left to right, from the top to the bottom: Δa [m], Δi [mdeg], $\Delta\alpha$ [deg], $\Delta\Omega$ [deg], Δe_x, Δe_y. Simulated time: 35 days

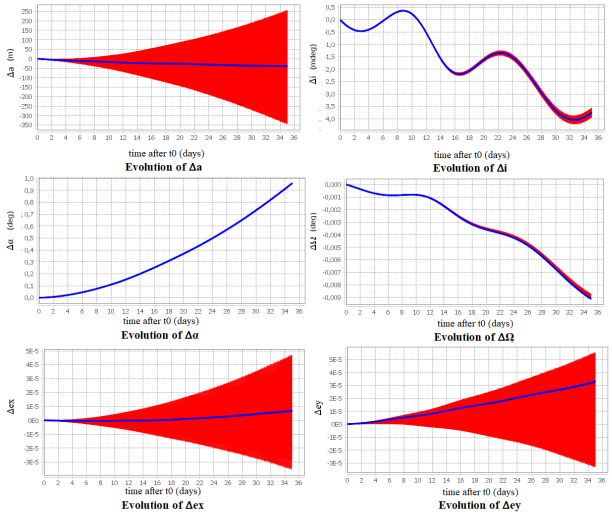

Fig. 3.11: Mission D1 - orbital parameters free evolution. From left to right, from the top to the bottom: Δa [m], Δi [mdeg], $\Delta\alpha$ [deg], $\Delta\Omega$ [deg], Δe_x, Δe_y. Simulated time: 35 days

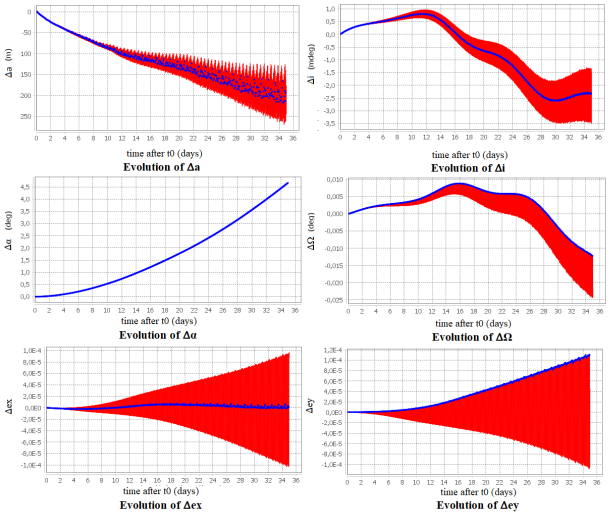

Fig. 3.12: Mission C - orbital parameters free evolution. From left to right, from the top to the bottom: Δa [m], Δi [mdeg], $\Delta\alpha$ [deg], $\Delta\Omega$ [deg], Δe_x, Δe_y. Simulated time: 35 days

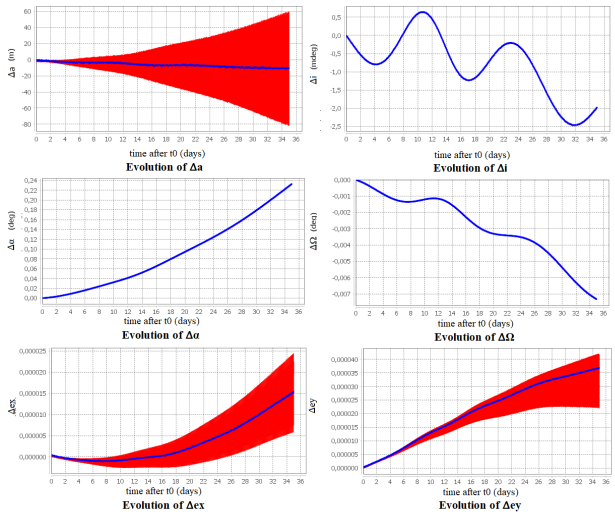

Fig. 3.13: Mission E - orbital parameters free evolution. From left to right, from the top to the bottom: Δa [m], Δi [mdeg], $\Delta\alpha$ [deg], $\Delta\Omega$ [deg], Δe_x, Δe_y. Simulated time: 35 days

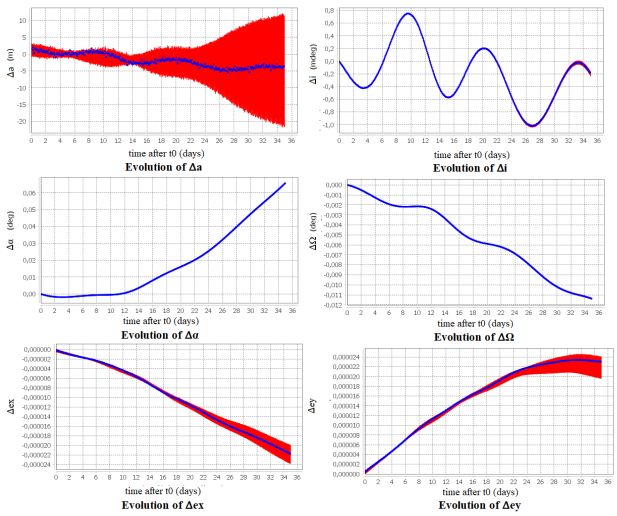

Fig. 3.14: Mission F - orbital parameters free evolution. From left to right, from the top to the bottom: Δa [m], Δi [mdeg], $\Delta\alpha$ [deg], $\Delta\Omega$ [deg], Δe_x, Δe_y. Simulated time: 35 dayss

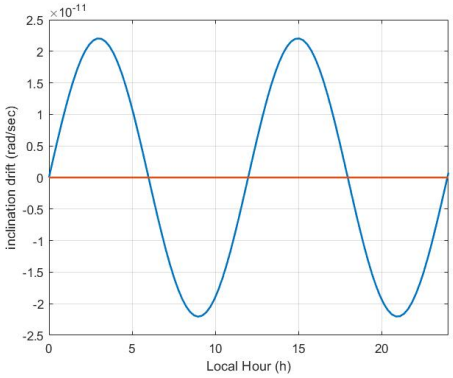

Fig. 3.15: Inclination drift due to the solar potential at the variation of the local mean time H, in case of sun-synchronous orbits

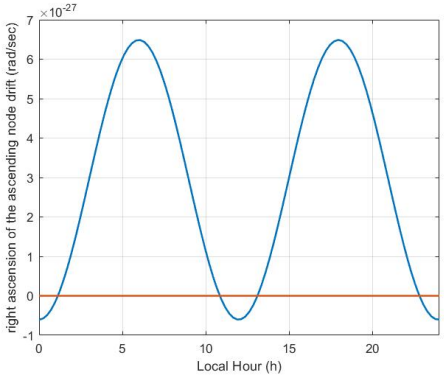

Fig. 3.16: Right ascension of the ascending node drift due to the solar potential at the variation of the local mean time H, in case of sun-synchronous orbits

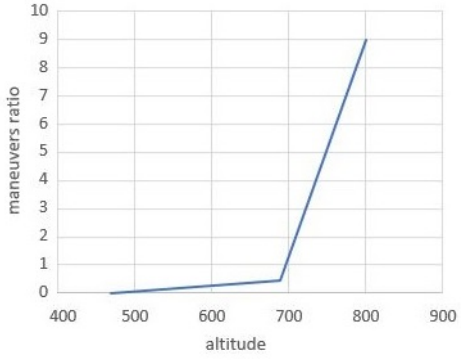

Fig. 3.17: Trend of the manoeuvres ratio (cross-track station keeping manoeuvres/in-track station keeping manoeuvres) with respect to altitude, for sun-synchronous missions

Table 3.1: Mission A1 outcomes: in-track and cross-track station keeping performance; in figures, the in-track and cross-track deviations in time

A1 mission

	old algorithm	new algorithm
percentage of respected in-track deviation (S1)	98.888%	) 98.781%
percentage of respected in-track deviation (S2)	99.863%	99.843%
maximum in-track deviation - S2	712 m	712.3 m
percentage of respected crossed-track deviation (S)	100%	100%
maximum crossed-track deviation - S	−293.86 m	−292.54 m
total number of manoeuvres	1191	1114
total ΔV	38.966 m/s	38.827 m/s

	optimised algorithm
percentage of respected in-track deviation (S1)	99.955%
percentage of respected in-track deviation (S2)	99.83%
maximum in-track deviation - S2	773.9 m
percentage of respected crossed-track deviation (S)	100%
maximum crossed-track deviation - S	−314.06 m
total number of manoeuvres	1121
total ΔV	38.685 m/s

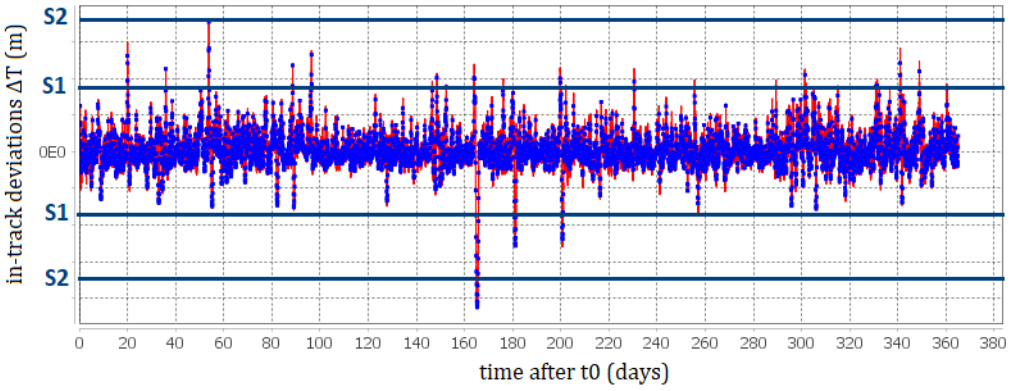

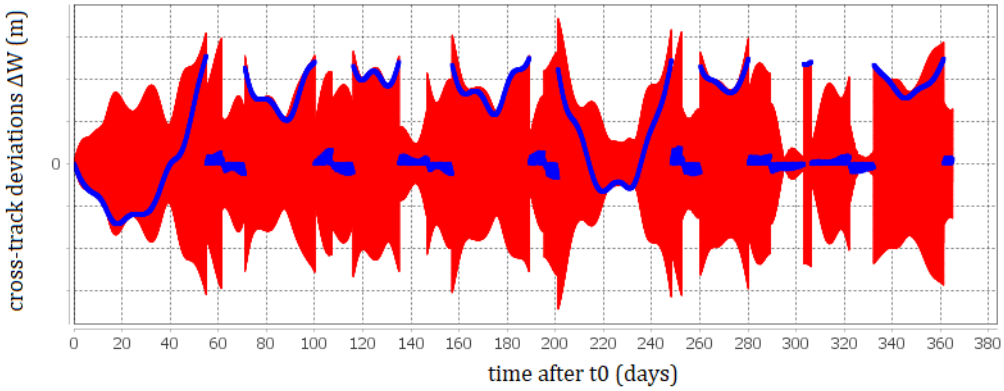

Table 3.2: Mission A2 outcomes: in-track and cross-track station keeping performance; in figures, the in-track and cross-track deviations in time

A2 mission

	old algorithm	new algorithm
percentage of respected in-track deviation (S1)	99.801%	99.554%
percentage of respected in-track deviation (S2)	100%	99.984%
maximum in-track deviation - S2	−1482.2 m	118.7 m
percentage of respected crossed-track deviation (S)	100%	100%
maximum crossed-track deviation - S	−282.47 m	−282.54 m
total number of manoeuvres	416	435
total ΔV	12.794 m/s	12.801 m/s

	optimised algorithm
percentage of respected in-track deviation (S1)	99.632%
percentage of respected in-track deviation (S2)	100%
maximum in-track deviation - S2	−15 m
percentage of respected crossed-track deviation (S)	100%
maximum crossed-track deviation - S	−283.01 m
total number of manoeuvres	435
total ΔV	12.847 m/s

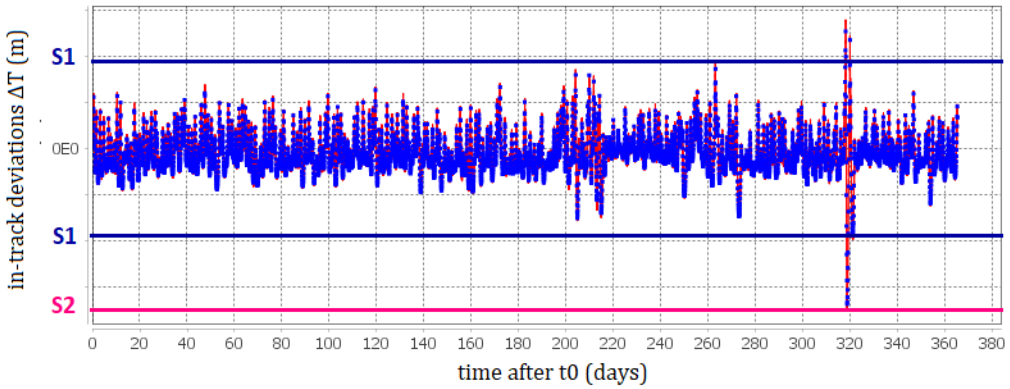

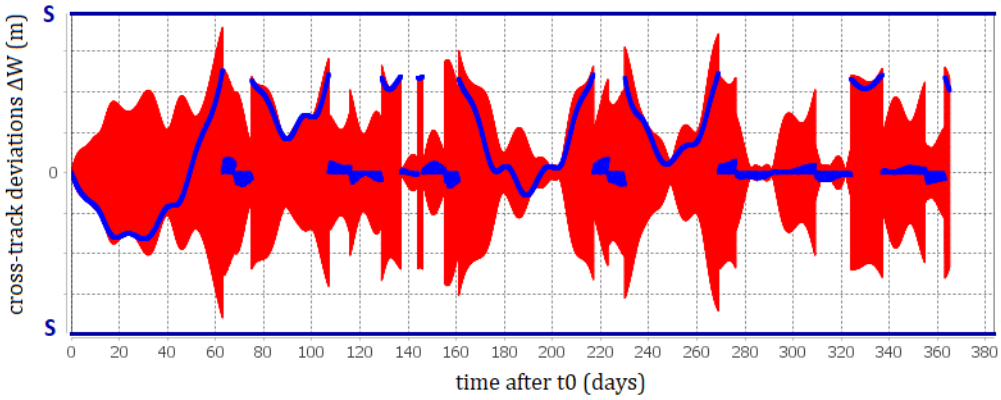

Table 3.3: Mission B1 outcomes: in-track and cross-track station keeping performance; in figures, the in-track and cross-track deviations in time

B1 mission

	old algorithm	new algorithm
percentage of respected in-track deviation (S1)	100%	100%
percentage of respected in-track deviation (S2)	100%	100%
maximum in-track deviation - S2	−2147.7 m	−2297.4 m
percentage of respected crossed-track deviation (S)	100%	100%
maximum crossed-track deviation - S	−313.7 m	−281.16 m
total number of manoeuvres	283	289
total ΔV	6.3175 m/s	6.7306 m/s

	optimised algorithm
percentage of respected in-track deviation (S1)	100%
percentage of respected in-track deviation (S2)	100%
maximum in-track deviation - S2	−2507.9 m
percentage of respected crossed-track deviation (S)	100%
maximum crossed-track deviation - S	−334.13 m
total number of manoeuvres	291
total ΔV	6.4369 m/s

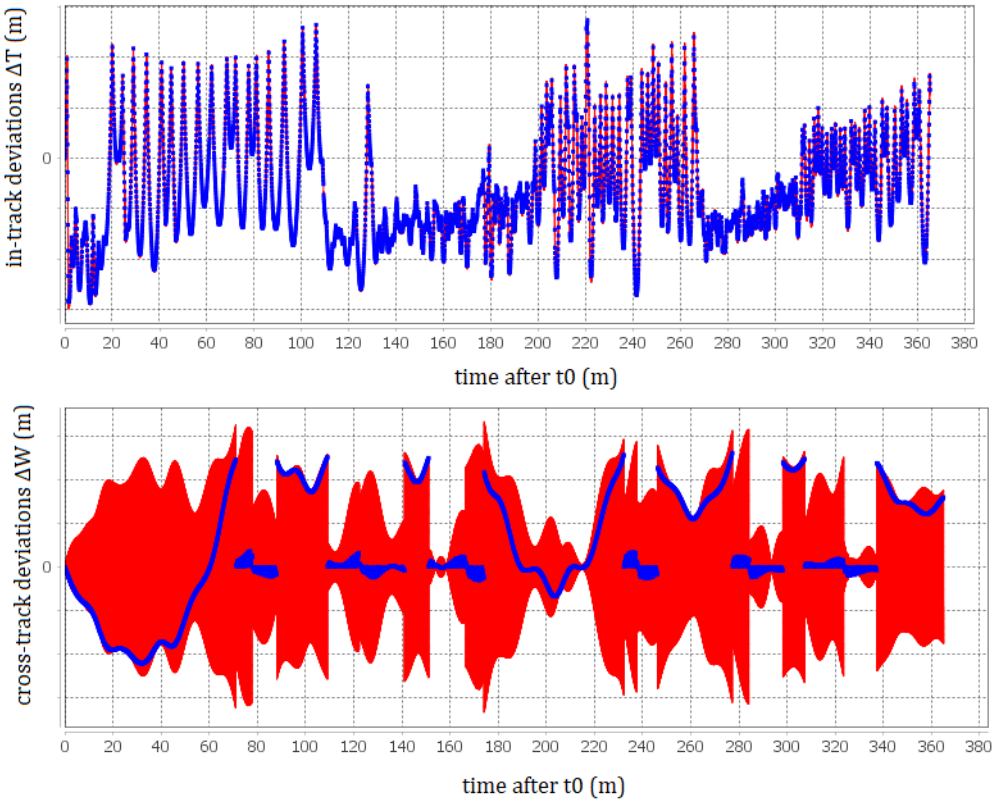

Table 3.4: Mission B2 outcomes: in-track and cross-track station keeping performance; in figures, the in-track and cross-track deviations in time

B2 mission

	old algorithm	new algorithm
percentage of respected in-track deviation (S1)	99.458%	99.842%
percentage of respected in-track deviation (S2)	100%	100%
maximum in-track deviation - S2	$-1497.4m$	-1968.4 m
percentage of respected crossed-track deviation (S)	99.228%	99.622%
maximum crossed-track deviation -S	166.3 m	166.1 m
total number of manoeuvres	181	150
total ΔV	19.149 m/s	12.93 m/s

	optimised algorithm
percentage of respected in-track deviation (S1)	99.97%
percentage of respected in-track deviation (S2)	100%
maximum in-track deviation - S2	-1893.3 m
percentage of respected crossed-track deviation (S)	99.903%
maximum crossed-track deviation - S	117.1 m
total number of manoeuvres	193
total ΔV	9.6547 m/s

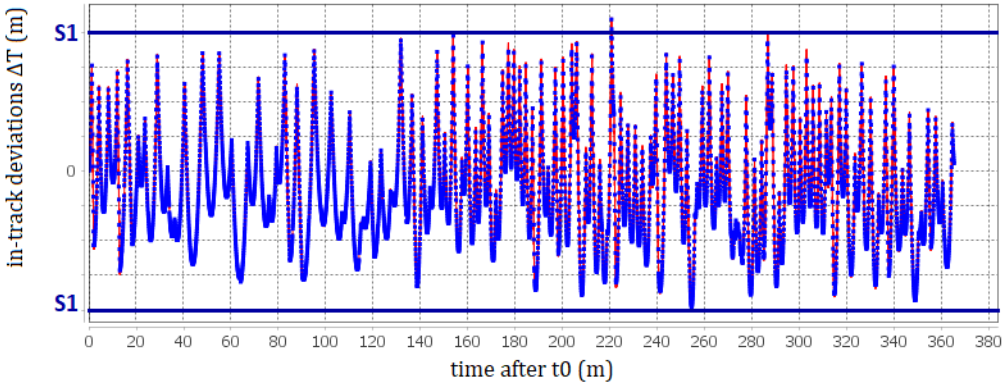

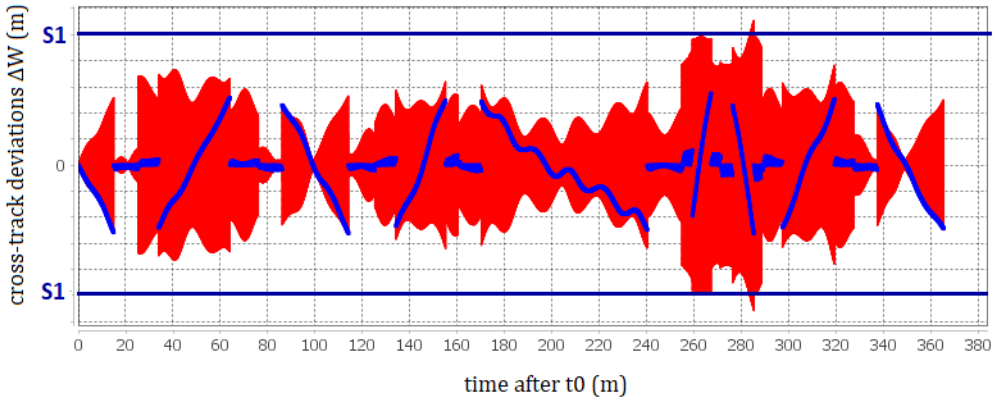

Table 3.5: Mission D1 outcomes: in-track and cross-track station keeping performance; in figures, the in-track and cross-track deviations in time

D1 mission

	old algorithm	new algorithm
percentage of respected in-track deviation (S1)	99.433%	99.483%
percentage of respected in-track deviation (S2)	100%	100%
maximum in-track deviation - S2	−1719.2 m	−1900.9 m
percentage of respected crossed-track deviation (S)	99.999%	100%
maximum crossed-track deviation - S	1.1 m	−4.8 m
total number of manoeuvres	688	662
total ΔV	34.304 m/s	34.059 m/s

	optimised algorithm
percentage of respected in-track deviation (S1)	100%
percentage of respected in-track deviation (S2)	100%
maximum in-track deviation - S2	−2081.7 m
percentage of respected crossed-track deviation (S)	100%
maximum crossed-track deviation - S	−30.7 m
total number of manoeuvres	694
total ΔV	33.887 m/s

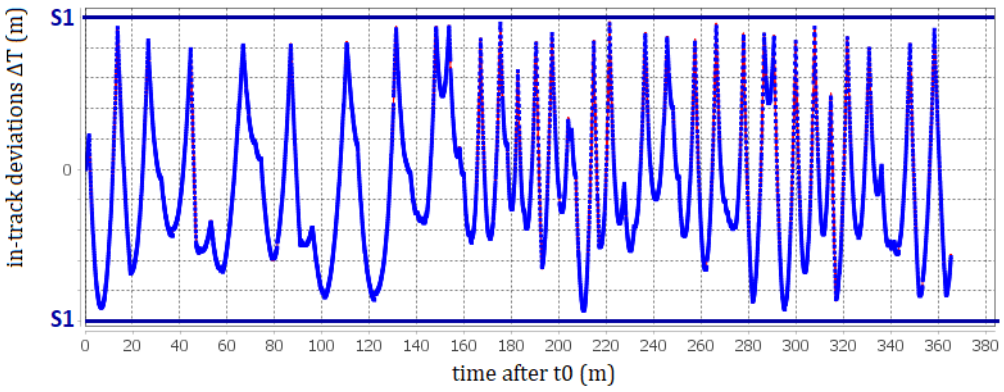

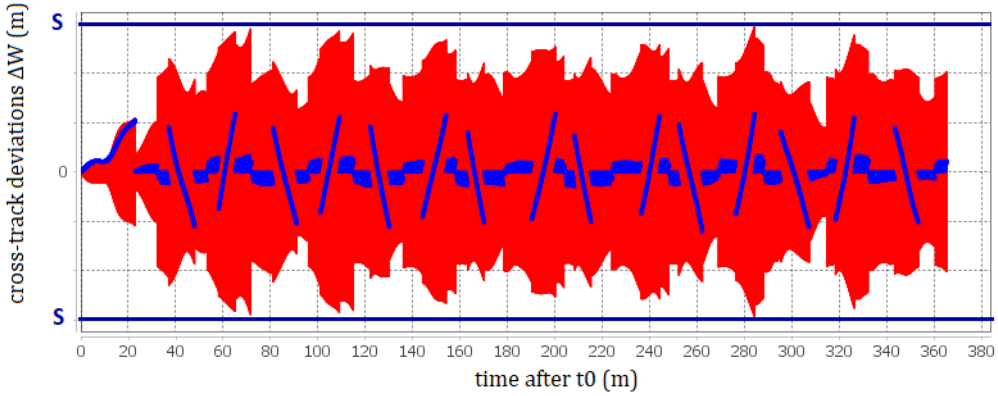

Table 3.6: Mission D2 outcomes: in-track and cross-track station keeping performance; in figures, the in-track and cross-track deviations in time

D2 mission

	old algorithm	new algorithm
percentage of respected in-track deviation (S1)	99.956%	99.99%
percentage of respected in-track deviation (S2)	100%	100%
maximum in-track deviation - S2	−1979.1 m	−1986.3 m
percentage of respected crossed-track deviation (S)	98.608%	98.598%
maximum crossed-track deviation - S	285.1 m	285.1 m
total number of manoeuvres	484	491
total ΔV	40.356 m/s	40.37 m/s

	optimised algorithm
percentage of respected in-track deviation (S1)	100%
percentage of respected in-track deviation (S2)	100%
maximum in-track deviation - S2	−2157.7 m
percentage of respected crossed-track deviation (S)	100%
maximum crossed-track deviation - S	−73.6 m
total number of manoeuvres	726
total ΔV	31.897 m/s

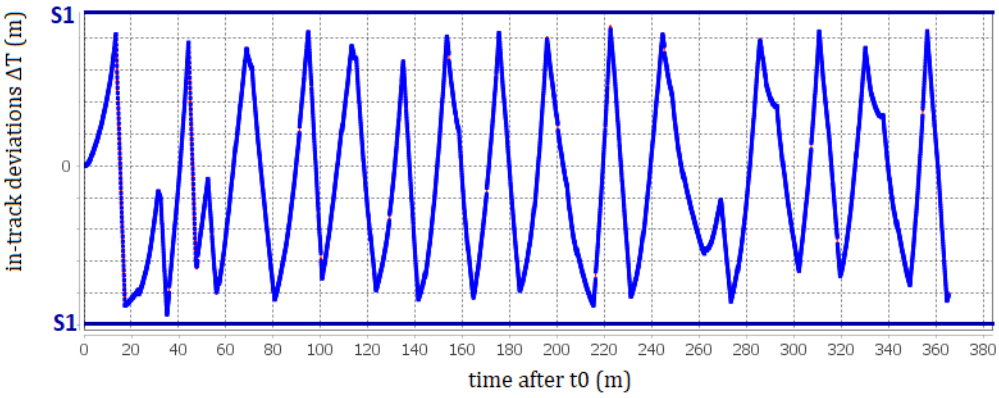

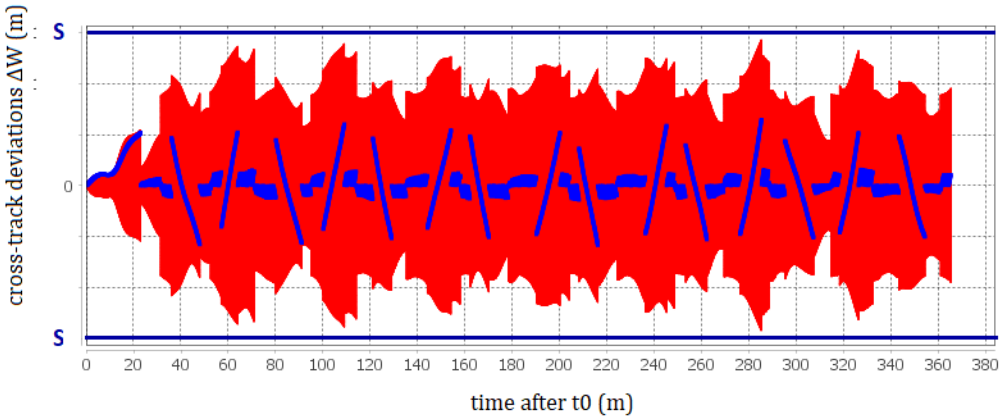

Table 3.7: Mission C outcomes: in-track and cross-track station keeping performance; in figures, the in-track and cross-track deviations in time

C mission

	old algorithm	new algorithm
percentage of respected in-track deviation (S1)	82.095%	85.93%
percentage of respected in-track deviation (S2)	96.963%	98.384%
maximum in-track deviation - S2	2615.2 m	1957.8 m
percentage of respected crossed-track deviation (S)	90.523%	91.142%
maximum crossed-track deviation - S	279.6 m	265.7 m
total number of manoeuvres	152	136
total ΔV	4.7639 m/s	4.4951 m/s

	optimised algorithm
percentage of respected in-track deviation (S1)	86.599%
percentage of respected in-track deviation (S2)	99.284%
maximum in-track deviation - S2	1085.7 m
percentage of respected crossed-track deviation (S)	96.194%
maximum crossed-track deviation - S	164.7 m
total number of manoeuvres	154
total ΔV	4.9845 m/s

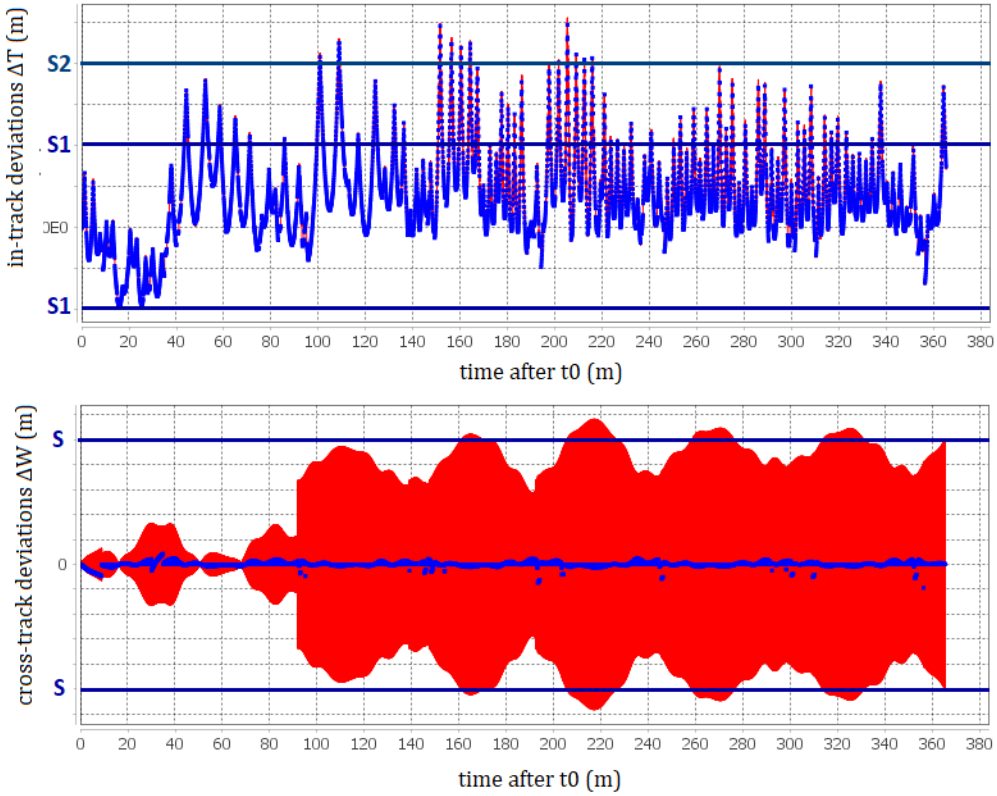

Table 3.8: Mission E outcomes:in-track and cross-track station keeping performance; in figures, the in-track and cross-track deviations in time

E mission

	old algorithm	new algorithm
percentage of respected in-track deviation (S1)	100%	100%
percentage of respected in-track deviation (S2)	100%	100%
maximum in-track deviation - S2	−2543.3 m	−2659.1 m
percentage of respected crossed-track deviation (S)	93.293%	93.644%
maximum crossed-track deviation - S	2591.6 m	2591.6 m
total number of manoeuvres	64	64
total ΔV	31.627 m/s	32.774 m/s

	optimised algorithm
percentage of respected in-track deviation (S1)	100%
percentage of respected in-track deviation (S2)	100%
maximum in-track deviation - S2	−3008.8 m
percentage of respected crossed-track deviation (S)	99.439%
maximum crossed-track deviation - S	169.3 m
total number of manoeuvres	50
total ΔV	18.042 m/s

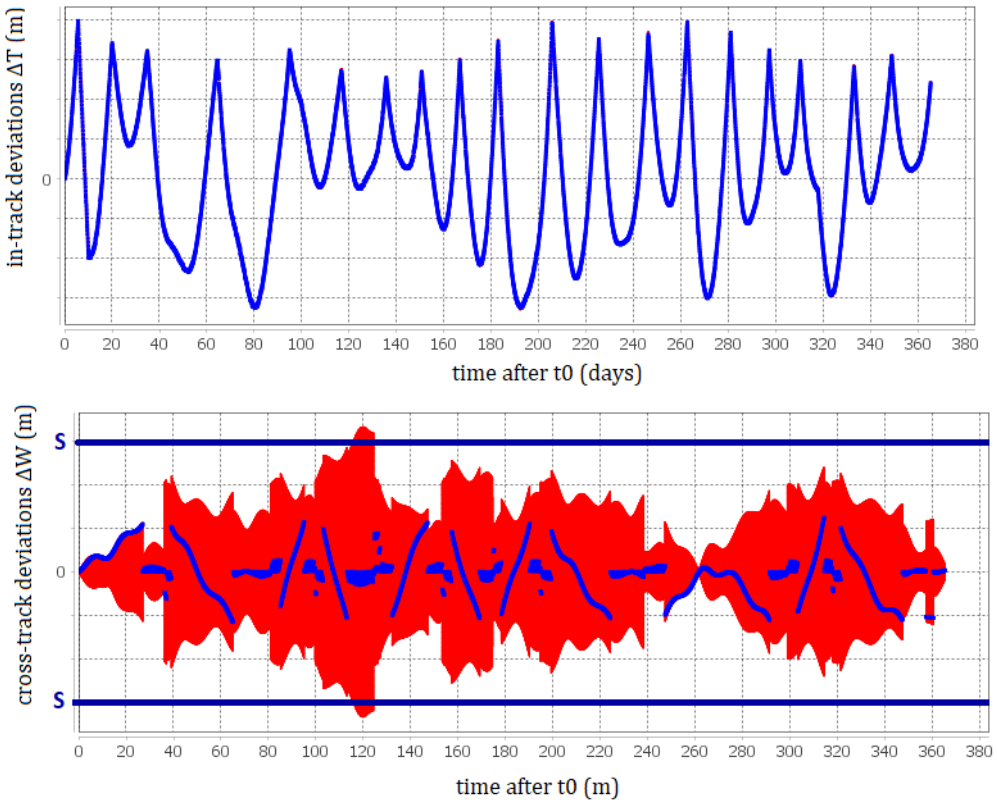

Table 3.9: Mission F outcomes: in-track and cross-track station keeping performance; in figures, the in-track and cross-track deviations in time

F mission

	old algorithm	new algorithm
percentage of respected in-track deviation (S1)	100%	97.361%
percentage of respected in-track deviation (S2)	100%	100%
maximum in-track deviation - S2	−2457.6 m	−1480 m
percentage of respected crossed-track deviation (S)	99.987%	100%
maximum crossed-track deviation - S	29.1 m	−22.5 m
total number of manoeuvres	42	50
total ΔV	6.4376 m/s	4.1554 m/s

	optimised algorithm
percentage of respected in-track deviation (S1)	100%
percentage of respected in-track deviation (S2)	100%
maximum in-track deviation - S2	−2585.3 m
percentage of respected crossed-track deviation (S)	100%
maximum crossed-track deviation - S	−24.9 m
total number of manoeuvres	57
total ΔV	4.1976 m/s

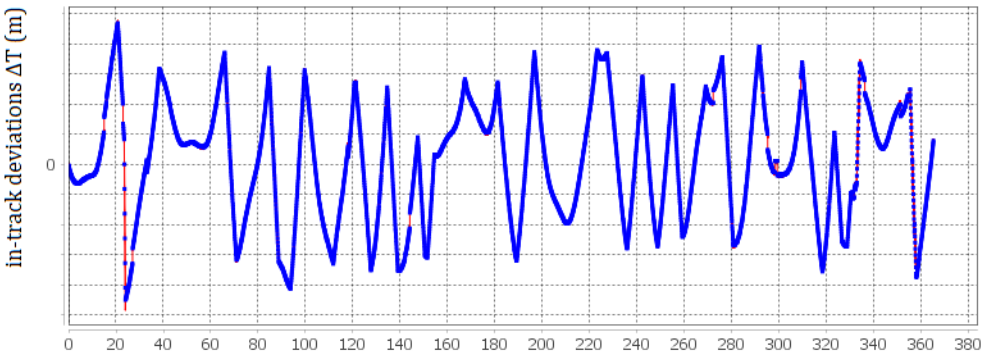

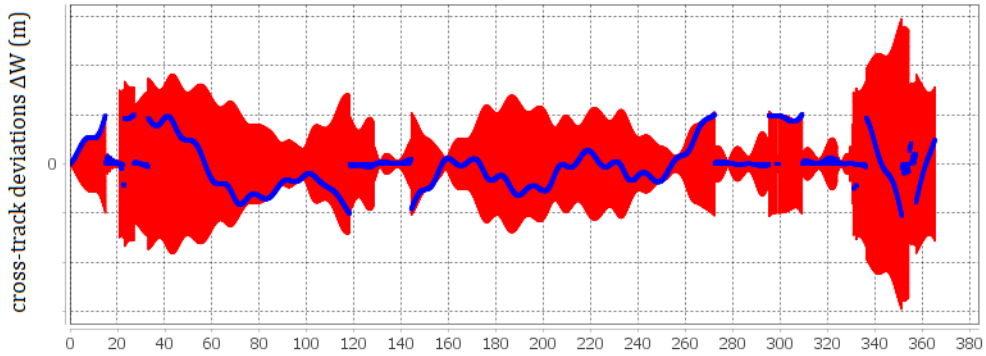

Chapter 4

Electric Mixed In-track Cross-track Manoeuvres

4.1 Strategy

The conception of electric manoeuvres is particularly complex. Indeed, time is necessary in order to achieve the ΔV require to perform a correction, such that a manoeuvre has to be spread in time. This has to be done by fulfilling the missions constraints: the manoeuvres have to be performed only in specified temporal slots. Thus, there is an elevated risk that while an in-track correction is performed, the cross-track threshold is crossed, or vice versa. For this reason, mixed in-track cross-track manoeuvres can be very useful. Of course, even in this case, several problems have to be faced, mainly concerning the manoeuvres slots managements: in particular they have to be exploited in such a way to allow an eccentricity optimisation while fulfilling the station keeping constraints.

The integration of electric mixed in-track cross-track manoeuvres is done according to the same logic adopted for the realisation of the impulsive mixed manoeuvres integration. Moreover, their computation is performed following the same procedure used for the standard in-plane and out-of-plane electric manoeuvres, explained in Section 2.3.

The electric mixed manoeuvres are conceived as a variation of out-of-plane manoeuvres, performed when both a positive correction of the semi-major axis and a correction of the inclination are required. They are evaluated as degraded impulsive manoeuvres, because of the time necessary to reach the desired value of ΔV. As for the standard manoeuvres, an efficiency $\widehat{\rho}$, whose value depends on the electric propulsion system, is introduced: the real targeted manoeuvre is characterised by $\Delta V_{elec} = \frac{\Delta V}{\widehat{\rho}}$. Thus, a mixed manoeuvre has two components:

- the tangent one : $\Delta V_{T_{elec}} = \frac{\Delta V_T}{\widehat{\rho}}$
- the out-of-plane one : $\Delta V_{N_{elec}} = \frac{\Delta V_N}{\widehat{\rho}}$

where ΔV_T is determined in the same way as for the mixed-impulsive manoeuvres, according to the value of ΔV_N: the variation of the semi-major axis that this last component induces is taken into account (see Section 3.2). Moreover, its value is limited according to the propulsion system capacity and to avoid optical instruments glare: it has to be always lower than a maximum, $\Delta V_{T_{max}}$:

$$\Delta V_{T_{max}} = min(\Delta V_{T_{max\_propu}}, \Delta V_{T_{max\_glare}})$$

where :

- $\Delta V_{T_{max\_glare}}$ is determined as explained in Chapter 5
- $\Delta V_{T_{max\_propu}} = \sqrt{\Delta V^2{}_{max\_propu} - \Delta V^2{}_{N_{elec}}}$

The mixed manoeuvres are evaluated when, at the limit date of the research horizon (date before which a correction manoeuvre is required to avoid the crossing of a threshold), both an inclination

(or/and a right ascension of the ascending node) and a positive semi-major axis corrections need emerges. All the possible slots, where the manoeuvre could be correctly executed, are stored; they are sorted according to the same criterion exploited for the selection of an impulsive mixed manoeuvre. Then, the selected manoeuvre is spread among them until either the targeted $\Delta V_{T_{elec}}$ or the targeted $\Delta V_{N_{elec}}$ is obtained. Finally, if one of these is not achieved, standard out-of-plane and in-plane manoeuvres are combined with the mixed manoeuvres along one same orbital period. In the case no mixed manoeuvre is found, a combination of in-plane and out-of-plane manoeuvres is evaluated. Thus, the results of the new algorithm integrated part can be the following:

- a combination of mixed manoeuvres;
- a combination of mixed manoeuvres and standard out-of-plane manoeuvres;
- a combination of mixed manoeuvres and standard in-plane manoeuvres;
- a combination of standard in-plane and out-of-plane manoeuvres;
- a combination of all the different types of manoeuvres.

In the next section, the algorithm behaviour is explained more in detail.

4.2 New algorithm

At the AOC activation, the limit date before which a manoeuvre has to be performed and the type of the most urgent manoeuvre are determined. When this last is an out-of plane one, a mixed manoeuvre is considered necessary if, at the limit date, a positive variation of the semi-major axis is required. When a positive in-plane manoeuvre is the most urgent manoeuvre, it is considered necessary, if, at the limit date, an inclination correction is needed. Once the mixed manoeuvre need is checked, the algorithm performs the following steps.

1. The criterion of evaluation of the manoeuvres is selected: they will be sorted according to their capacity of maximising either ΔV_T or the eccentricity.
2. The research horizon is analysed in order to determine all the possible mixed and out-of-plane manoeuvres. The two types of manoeuvres are sorted separately: the first ones according to the selected criterion; the others in an inverse chronological order. For each manoeuvre the computed value of ΔV is corrected with the efficiency $\widehat{\rho}$. For the out-of-plane manoeuvres the research continues also after the limit date: indeed, the out-of-plane manoeuvre are more expensive and the appropriate slots are more rare.
3. The best mixed manoeuvre is selected according to the evaluation criterion. Thus, the targeted $\Delta V_{T_{elec_{targeted}}}$ and $\Delta V_{N_{elec_{targeted}}}$ are determined. Then, the manoeuvre is spread on the slots where the other mixed manoeuvres were found. The inclination of each imposed mixed manoeuvre with respect to the N axis is computed as:

$$\gamma = min\Big(\arctan\Big(\frac{\Delta V_{T_{elec_{targeted}}}}{\Delta V_{N_{elec_{targeted}}}}\Big), \gamma_{max}\Big)$$

   where γ_{max} is a slot property imposed to avoid instruments glare as explained in Chapter 5. Of course, during the best manoeuvre spread, the targeted values $\Delta V_{T_{elec_{targeted}}}$ and $\Delta V_{N_{elec_{targeted}}}$ reduce. If $\Delta V_{T_{elec_{targeted}}}$ is achieved, all the next imposed manoeuvres are converted into standard out-of-plane manoeuvres. This distribution operation ends when the stored slots terminate or if $\Delta V_{N_{elec_{targeted}}}$ is achieved.
4. Several situations can occur:
   - both $\Delta V_{T_{elec_{targeted}}}$ and $\Delta V_{N_{elec_{targeted}}}$ are achieved: the research ends;

- $\Delta V_{N_{elec_{targeted}}}$ is not achieved: in this case the manoeuvre continues to be spread on the simple out-of-plane manoeuvres slots previously stored. Eventually the previously imposed mixed manoeuvres are converted into out-of-plane manoeuvres if their in-plane component value is comparable to the out-of-plane component one (which is rare).
- $\Delta V_{T_{elec_{targeted}}}$ is not achieved: all the research horizon is explored again to find standard in-plane manoeuvres to associate to the ones already imposed.

5. Once all the possible manoeuvres are selected, they are organized in chronological order. Then, their value is updated: it is necessary to take into account each manoeuvre effects on the orbit, which can induce the cancellation or the variation of successive manoeuvres, previously computed. For example, if a standard in-plane manoeuvre is added to the already selected manoeuvres and chronologically it is before a previously computed mixed manoeuvre, the semi-major axis correction that this last one imposes could become useless: it would converted into an inclination manoeuvre. Also an inclination manoeuvre can modify the need in the semi-major axis correction at a forward date. Thus, the updating is essential to impose the appropriate needed corrections.

Evidently, if it is necessary to explore the research horizon in order to find standard in-plane manoeuvres, only the slots which don't overlap the previously selected manoeuvres slots are taken into account. In case no mixed manoeuvre is found, standard out-of-plane manoeuvres are imposed; successively, the research horizon is analysed to search for standard in-plane manoeuvres to associate to them. If no inclination and mixed manoeuvres are found in the research horizon and the most urgent manoeuvre is a positive in-plane, the original algorithm method for the computation of in-plane manoeuvres is launched.

Figure 4.1 shows the scheme of the algorithm behaviour related to the electric mixed manoeuvres integration: it is a kind of flow chart. The arrows link an operation to the successive one. The yellow windows are about the preliminary steps, from the selection of the research horizon limit date to the determination of the manoeuvres selection criterion. The light blue windows concern the computation of out-of-plane and mixed manoeuvres. Inside the blue boxes, the windows are associated to the operations done to spread a selected manoeuvre and eventually to combine different types of manoeuvres. In particular, the right box is referred to the case in which no mixed manoeuvre is found.

4.3 Analysis of the results

In comparison with the performance of the original algorithm, the results are really satisfying. After the integration of the new type of manoeuvres, the performance obtained improves significantly for most of the analysed missions. Then, after the process of optimisation (see Section 3.5), the results fully demonstrate the advantages of mixed manoeuvres for a satellite provided by an electric propulsion system: they highlight the need of performing the required station keeping corrections contemporary.

As in the case of the impulsive mixed manoeuvres integration, the only missions for which the results are not completely satisfying are missions A1 and A2. In the case of mission A1, the improvement of the performance is slight and it causes an important increase of the energy cost. In the case of mission A2, there is a small degradation of the in-track station keeping, even though the maximum deviation decreases. However, both missions A1 and A2 are particularly problematic, as explained in the previous Chapter 3, as they are characterised by low orbit highly affected by the atmospheric drag. In addiction, mission A1 undergoes a very high solar activity. Moreover, even though the new performance is not as good as that of other missions, a significant degradation does not arise. Considering this and also the fact they are the only exceptions, the conclusion is that the new manoeuvres integration is useful to obtain a better station keeping performance.

An analysis of the obtained results is shown in Figure 4.2. It is possible to observe that the ΔV decrease is rare. In some cases, its increase is significant. Anyway, with the exception of mission A1,

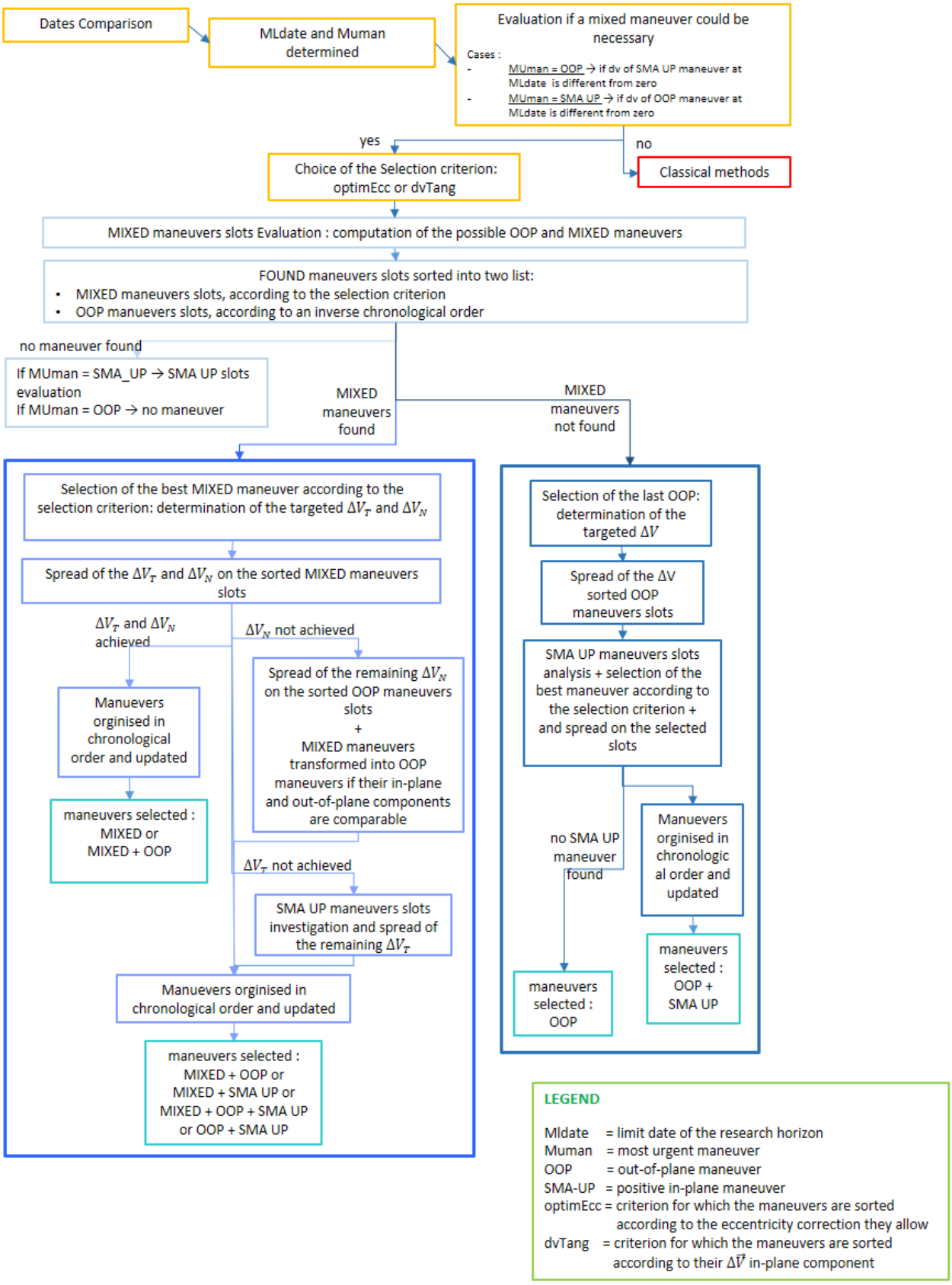

Fig. 4.1: Mixed manoeuvres integration: algorithm behaviour scheme

it is usually associated to a significant improvement of the missions performance. All the outcomes are shown in Tables 4.1 - 4.7.

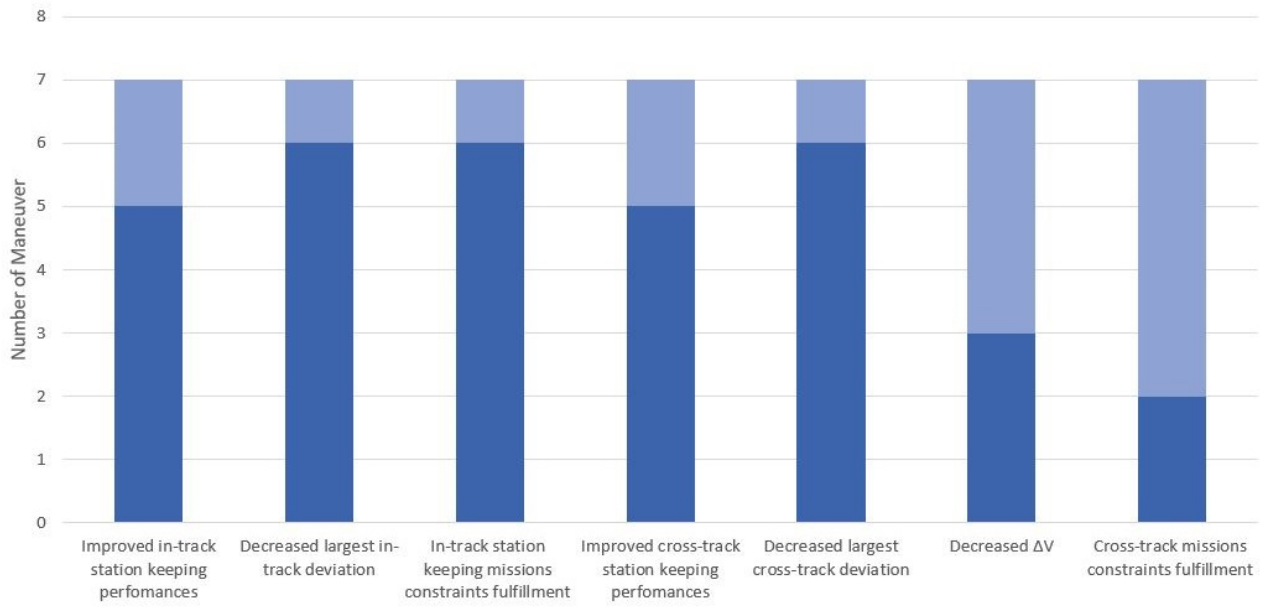

Fig. 4.2: Electric mixed manoeuvres integration outcomes

4.4 Analysis of the algorithm behaviour

In comparison to impulsive manoeuvres, the algorithm usually computes electric mixed manoeuvres, when the most urgent correction is a cross-track station keeping one. However, the times, when they are determined being an in-plane manoeuvre the most urgent, increase. This happens above all for missions A1 and A2. Then, the algorithm has a largest tendency to select different kinds of manoeuvres combinations, even though the more frequently selected remain the combinations of mixed manoeuvres. These are followed by the combinations of mixed and standard in-plane manoeuvres. The behaviour of the described algorithm is consistent with the greater need of performing manoeuvres if an electric propulsion system is exploited, since a long time is necessary to achieve the required ΔV .

The $\frac{cross-track}{in-track}$ manoeuvres ratios and the performance obtained for the analysed missions are perfectly consistent with that achieved for the corresponding chemical propulsion system missions. The only exception is mission A1, for which the number of inclination manoeuvres increases: the manoeuvres ratio is $1 : 0.098$. This is motivated by the greater need of manoeuvreing in the case of an electric propulsion system. Thanks to the integration of mixed manoeuvre, this is allowed even more than before (the old algorithm manoeuvres ratio was $1 : 0.0095$ for mission A1).

Table 4.1: Mission A1 outcomes: in-track and cross-track station keeping performance; in figures, the in-track and cross-track deviations in time

A1 mission

	old algorithm	new algorithm
percentage of respected in-track deviation (S1)	99.539%	99.541%
percentage of respected in-track deviation (S2)	100%	100%
maximum in-track deviation - S2	−374 m	−374 m
percentage of respected crossed-track deviation (S)	100%	100%
maximum crossed-track deviation - S	−390.09 m	−309.09 m
total number of manoeuvres	1163	1234
total ΔV	42.886 m/s	79.823 m/s

	optimised algorithm
percentage of respected in-track deviation (S1)	99.541%
percentage of respected in-track deviation (S2)	100%
maximum in-track deviation - S2	374 m
percentage of respected crossed-track deviation (S)	100%
maximum crossed-track deviation - S	−390.09 m
total number of manoeuvres	1234
total ΔV	79.823 m/s

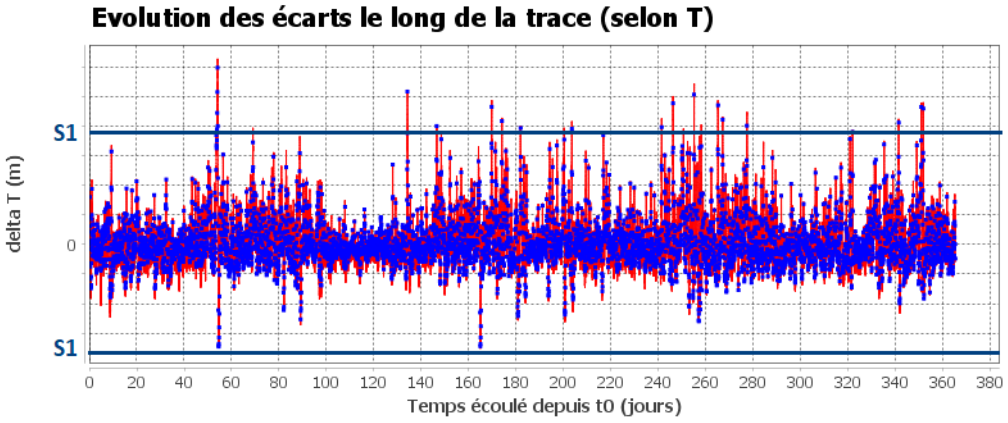

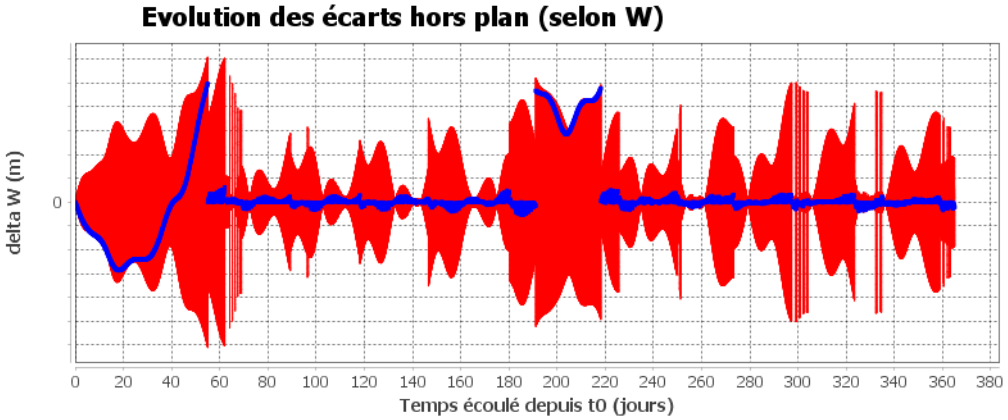

Table 4.2: Mission A2 outcomes: in-track and cross-track station keeping performance; in figures, the in-track and cross-track deviations in time

A2 mission

	old algorithm	new algorithm
percentage of respected in-track deviation (S1)	99.951%	99.679%
percentage of respected in-track deviation (S2)	100%	100%
maximum in-track deviation - S2	-899.6 m	$-783.8m$
percentage of respected crossed-track deviation (S)	100%	100%
maximum crossed-track deviation - S	$-286.37m$	-286.37 m
total number of manoeuvres	665	664
total ΔV	13.687 m/s	17.256 m/s

	optimised algorithm
percentage of respected in-track deviation (S1)	99.86%
percentage of respected in-track deviation (S2)	100%
maximum in-track deviation - S2	-924.2 m
percentage of respected crossed-track deviation (S)	100%
maximum crossed-track deviation - S	-286.5 m
total number of manoeuvres	435
total ΔV	14.771 m/s

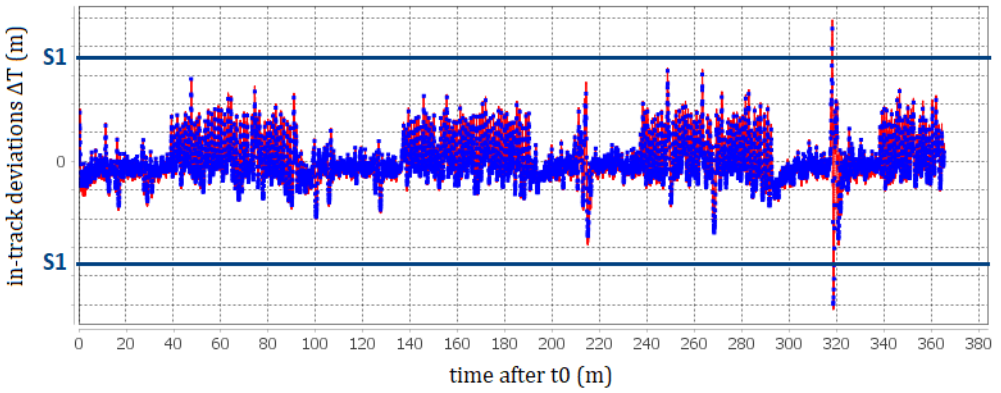

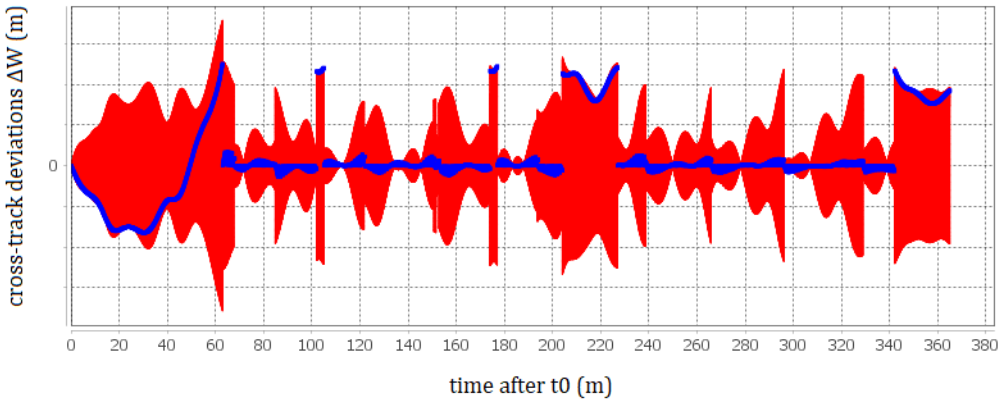

Table 4.3: Mission C outcomes: in-track and cross-track station keeping performance; in figures, the in-track and cross-track deviations in time

C mission

	old algorithm	new algorithm
percentage of respected in-track deviation (S1)	90.7%	95.698%
percentage of respected in-track deviation (S2)	95.949%	98.457%
maximum in-track deviation - S2	3242.6 m	2600.9 m
percentage of respected crossed-track deviation (S)	92.19%	91.883%
maximum crossed-track deviation - S	1236.4 m	1279 m
total number of manoeuvres	259	290
total ΔV	5.1403 m/s	5.1241 m/s

	optimised algorithm
percentage of respected in-track deviation (S1)	96.265%
percentage of respected in-track deviation (S2)	99.191%
maximum in-track deviation - S2	2564.5 m
percentage of respected crossed-track deviation (S)	99.572%
maximum crossed-track deviation - S	58.2 m
total number of manoeuvres	266
total ΔV	5.1809 m/s

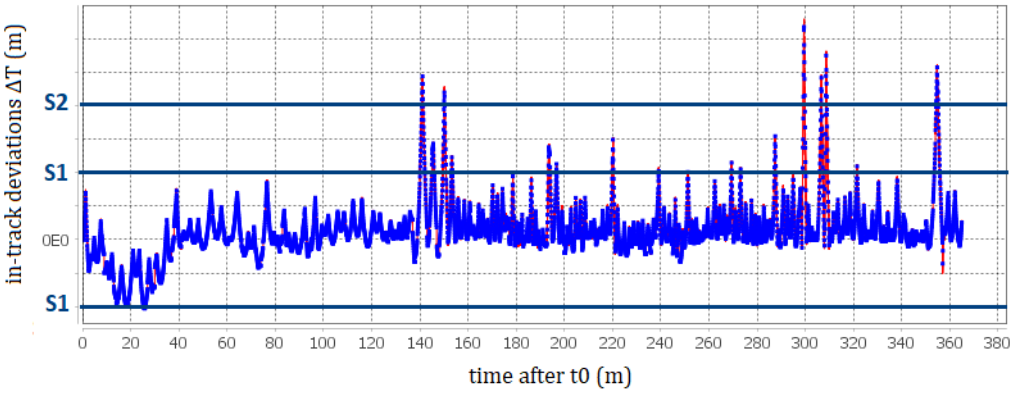

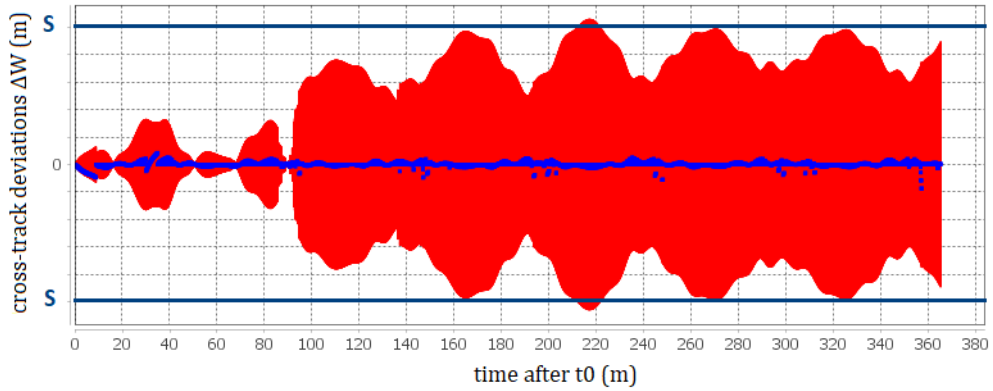

Table 4.4: Mission D1 outcomes: in-track and cross-track station keeping performance; in figures, the in-track and cross-track deviations in time

D1 mission

	old algorithm	new algorithm
percentage of respected in-track deviation (S1)	98.566%	99.995%
percentage of respected in-track deviation (S2)	100%	100%
maximum in-track deviation - S2	−1241.6 m	−1981.8 m
percentage of respected crossed-track deviation (S)	98.136%	98.178%
maximum crossed-track deviation - S	185.9 m	−236.6 m
total number of manoeuvres	458	422
total ΔV	38.224 m/s	37.613 m/s

	optimised algorithm
percentage of respected in-track deviation (S1)	100%
percentage of respected in-track deviation (S2)	100%
maximum in-track deviation - S2	−2184.7 m
percentage of respected crossed-track deviation (S)	99.545%
maximum crossed-track deviation - S	−123.3 m
total number of manoeuvres	586
total ΔV	36.534 m/s

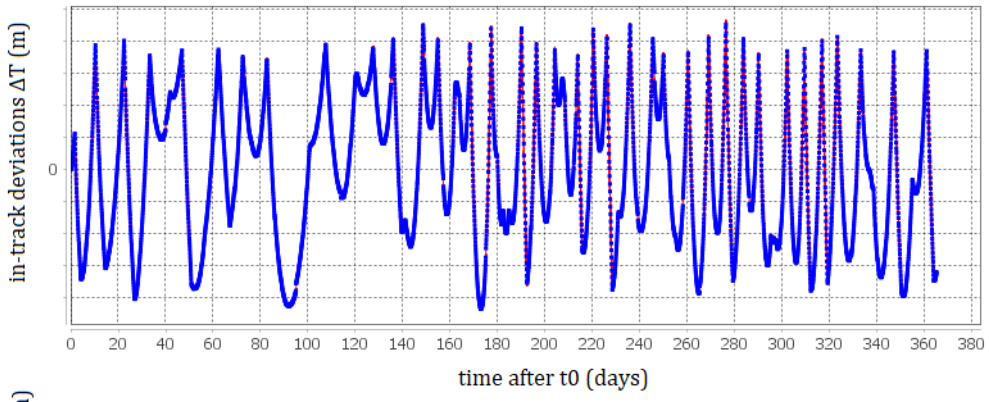

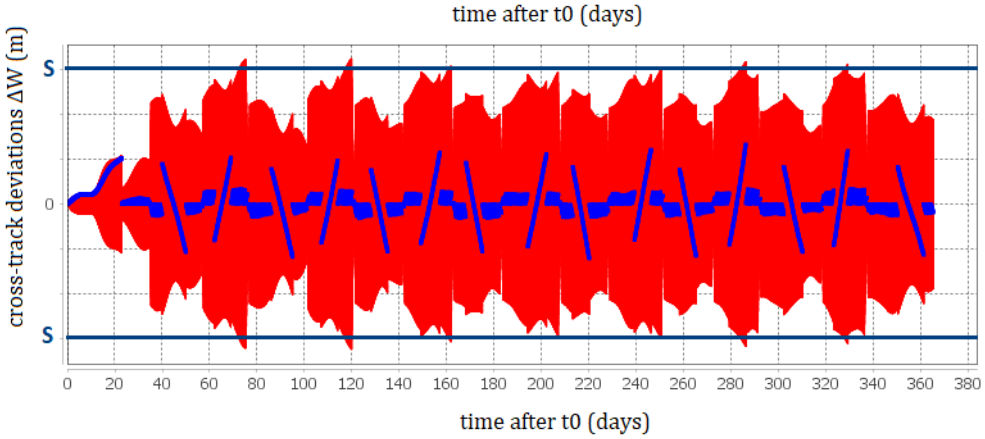

Table 4.5: Mission D2 outcomes: in-track and cross-track station keeping performance; in figures, the in-track and cross-track deviations in time

D2 mission

	old algorithm	new algorithm
percentage of respected in-track deviation (S1)	80.324%	99.699%
percentage of respected in-track deviation (S2)	98.116%	100%
maximum in-track deviation - S2	249.1 m	−1860.9 m
percentage of respected crossed-track deviation (S)	86.999%	98.107%
maximum crossed-track deviation - S	2745.9 m	188.7 m
total number of manoeuvres	363	427
total ΔV	14.799 m/s	37.736 m/s

	optimised algorithm
percentage of respected in-track deviation (S1)	100%
percentage of respected in-track deviation (S2)	100%
maximum in-track deviation - S2	−2315 m
percentage of respected crossed-track deviation (S)	99.862%
maximum crossed-track deviation - S	95.3 m
total number of manoeuvres	653
total ΔV	34.658 m/s

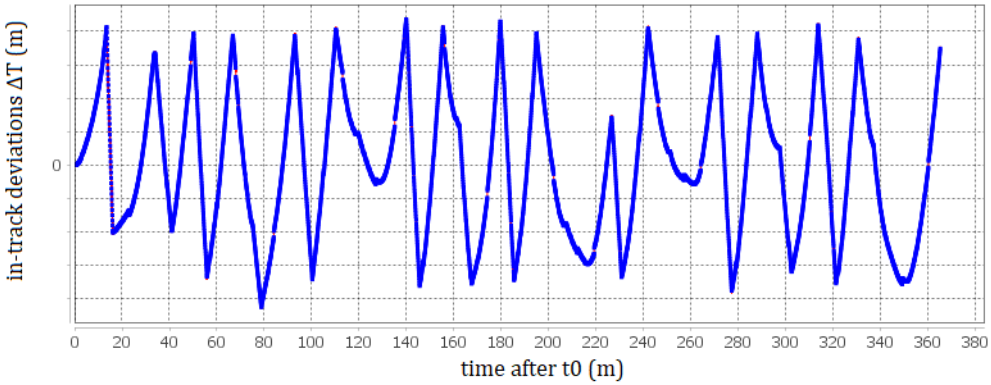

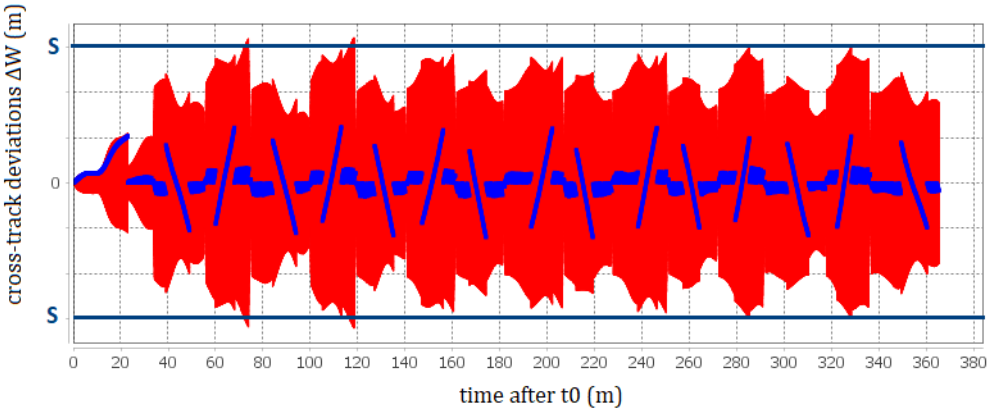

Table 4.6: Mission D3 outcomes: in-track and cross-track station keeping performance; in figures, the in-track and cross-track deviations in time

D3 mission

	old algorithm	new algorithm
percentage of respected in-track deviation (S1)	100%	100%
percentage of respected in-track deviation (S2)	98.116%	100%
maximum in-track deviation - S2	−2200 m	−2200 m
percentage of respected crossed-track deviation (S)	97.961%	98.08%
maximum crossed-track deviation - S	295.9 m	296.9 m
total number of manoeuvres	771	828
total ΔV	39.99 m/s	39.753 m/s

	optimised algorithm
percentage of respected in-track deviation (S1)	100%
percentage of respected in-track deviation (S2)	100%
maximum in-track deviation - S2	−2674.1 m
percentage of respected crossed-track deviation (S)	99.784%
maximum crossed-track deviation - S	109.9 m
total number of manoeuvres	750
total ΔV	37.803 m/s

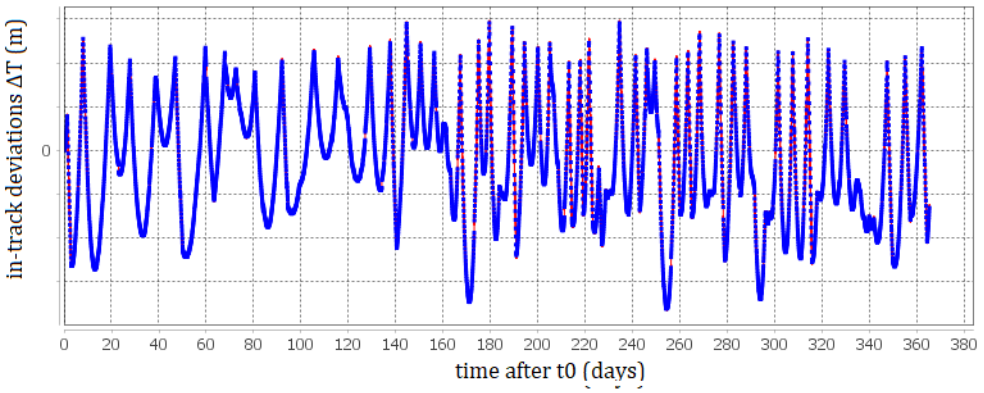

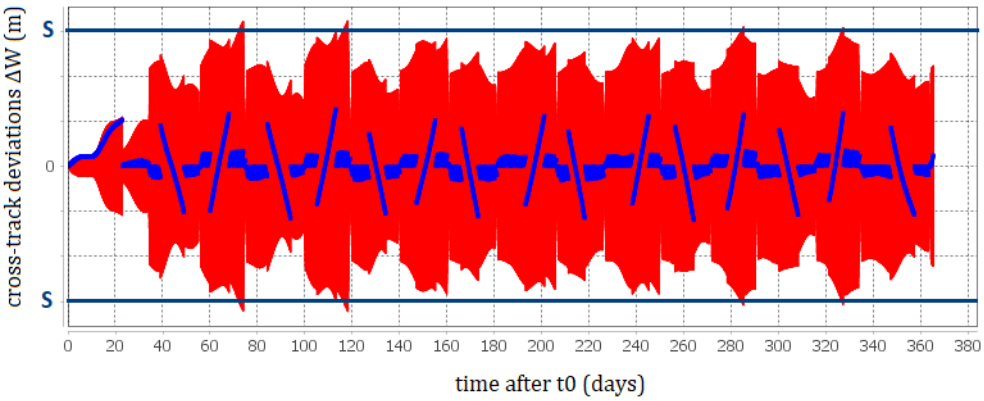

Table 4.7: Mission E outcomes: in-track and cross-track station keeping performance; in figures, the in-track and cross-track deviations in time

E mission

	old algorithm	new algorithm
percentage of respected in-track deviation (S1)	98.286%	98.286%
percentage of respected in-track deviation (S2)	100%	100%
maximum in-track deviation - S2	−934.2 m	−934.2 m
percentage of respected crossed-track deviation (S)	99.378%	98.562%
maximum crossed-track deviation - S	249.6 m	270.5 m
total number of manoeuvres	106	129
total ΔV	15.394 m/s	21.981 m/s

	optimised algorithm
percentage of respected in-track deviation (S1)	100%
percentage of respected in-track deviation (S2)	100%
maximum in-track deviation - S2	−3001.3 m
percentage of respected crossed-track deviation (S)	100%
maximum crossed-track deviation - S	−95.4 m
total number of manoeuvres	88
total ΔV	6.7488 m/s

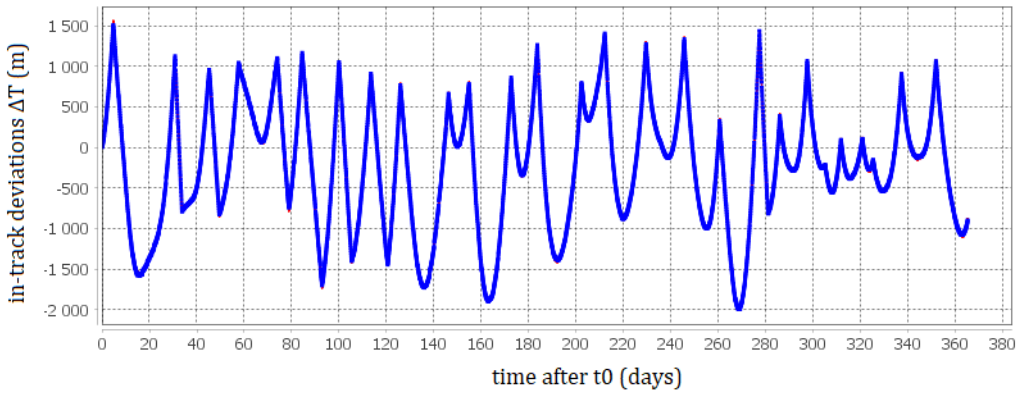

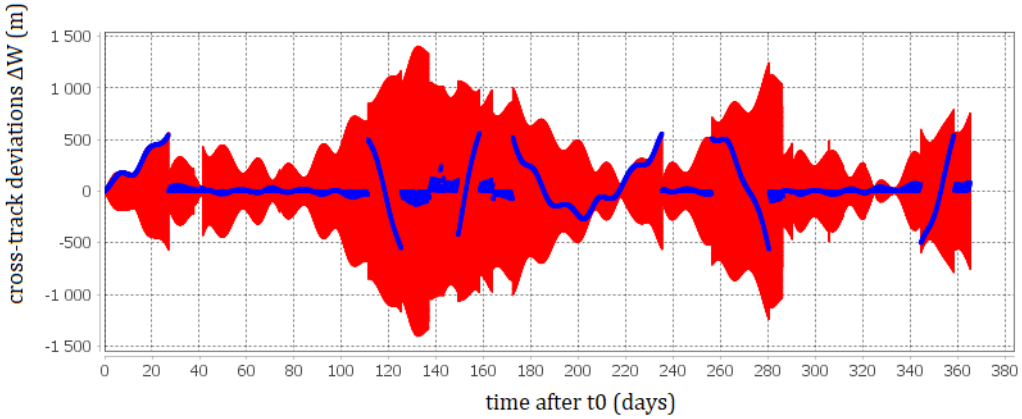

Chapter 5

Mixed In-track Cross-track Manoeuvres Time Slots

5.1 Slots definition problem

The introduction of mixed in-track cross-track manoeuvres triggers the necessity of defining the temporal slots over which it is allowed to perform them. As explained in Section 2.1.4, the slots are determined on the basis of the mission and the system constraints. In particular, it is necessary to assure a specific smallest angular distance between the Sun (or eventually another celestial body) and an optical instrument to avoid its glare. For example, in the case of a stars tracker the distance has to be almost equal to 30° [16]. This implies some constraints on the direction of the imposed $\Delta\mathbf{V}$.

Because of the analysed missions characteristics, the smallest angular distance that has to be assured between the Sun and the $\Delta\mathbf{V}$ is equal to the smallest angular distance required between the Sun and the optical instrument.

The objective of the procedure implemented, described in this chapter, is to determined the mixed manoeuvres temporal slots: then, they are listed into files with all their essential characteristics (such as the date and the duration), similar to the files already existing for the other standard manoeuvres slots. These files are read by the algorithm at its activation, so that it gets the information about the temporal intervals during which it is allowed to perform a specific manoeuvre. In particular, the implemented procedure allows the mixed in-track cross-track manoeuvres slots generation starting from the already existing out-of-plane manoeuvres slots.

5.2 Adopted strategy

The procedure adopted to generate the slots is a direct consequence of the way in which mixed manoeuvres are conceived. A mixed manoeuvre is generated as an out-of-plane manoeuvre to which a tangential component is added. Moreover, the magnitude of the out-of-plane component is usually higher than that of the in-plane one. Thus, the mixed manoeuvres slots are generated from the existing out-of-plane manoeuvres slots, which have been previously determined at CNES to satisfy the missions and the systems constraints. To give an example, in the case of an electric propulsion system exploiting solar panels, these slots have been already conceived to exclude the time intervals corresponding to solar eclipses. Moreover, they are defined to avoid instruments glare in case of a simple out-of-plane manoeuvre. Thus, it is sufficient to add the information relative to the largest tangential component that can be added to the out-of-plane manoeuvre to continue avoiding the instruments glare in case of mixed manoeuvres, without taking into account all the other missions constraints. In this way, the determination procedure of the mixed manoeuvres time slots is simplified.

In particular, to evaluate the largest tangential component that can be added, the following additional information is provided: the largest inclination angle, $\widetilde{\gamma}$, of the mixed $\Delta\mathbf{V}$ with respect to the out-of-plane direction. Thus, the largest tangential component allowed will be equal to $\Delta V_{T_{max}} = \Delta V_N \tan\widetilde{\gamma}$, where ΔV_N is the out-of-plane component calculated for the right ascension of

the ascending node correction. The evaluation of $\widetilde{\gamma}$ is performed at several dates during one single slot; if its variation is important, the slot is divided into multiple slots. The value of $\widetilde{\gamma}$, associated to one slot, assures the possibility of a mixed manoeuvre without glare risks at each time in the interval. The slots division has to be handled in such a way to avoid the optical instruments glare without limiting the value of the largest tangential component excessively and minimising the total number of resulting slots for computational reasons. Indeed, higher the number of slots that AOC has to analyse, longer will be the computational time associated to each mission. The following section explains the way in which the angle $\widetilde{\gamma}$ is computed. Section 5.4 is about the way in which the out-of-planes slots division is handled.

5.3 The largest angle γ : definition

As explained in Section 5.1, a smallest angular distance $\delta_{admissible}$ between the manoeuvre $\Delta\mathbf{V}$ and the Sun directions is required. It is possible to define a cone having the satellite-Sun position vector as axis and $\delta_{admissible}$ as aperture: in the following, it will be indicated as Sun cone. It is evident that the mixed $\Delta\mathbf{V}$ has not to intersect it. In the case of a mixed manoeuvre the $\Delta\mathbf{V}$ is not known a priori. Thus, it is necessary to determine which directions of $\Delta\mathbf{V}$ are forbidden on the manoeuvre plane.

The manoeuvre plane corresponds to the **TN** plane of the satellite coordinate system, that will be exploited for this analysis. In particular, the focus has to be on the semi-plane associated to positive values of the **T** axis, as the mixed manoeuvres tangential component is always positive. Let be $\gamma \in [0, 2\pi[$ the angle computed from the **N** axis on the **TN** plane positively clockwise (Figure 5.1): it identifies every possible direction of $\Delta\mathbf{V}$ on the manoeuvre plane. Thus, the range of forbidden directions is identified by the range of γ values for which the angular distance to the Sun direction is less than $\delta_{admissible}$.

At a considered date, the angular distance δ_{dist} between the Sun direction and each direction on the **TN** plane can be determined solving a spherical trigonometry problem (Figure 5.2):

$$\delta_{dist} = \arccos \cos\gamma \cos b + \sin\gamma \sin b \cos\beta \tag{5.1}$$

where the following notations are adopted:

- β is the angle between the **TN** plane and the **sN** plane, being **s** the Sun position vector;
- b is the angle between **N** and **s**.

At a fixed date, δ_{dist} is a function of the only γ. It is continuous and it is characterised by a global minimum and a global maximum. Indeed, the derivative of $f(\gamma)$ is

$$\frac{d\delta_{dist}}{d\gamma}(\gamma) = \frac{\sin\gamma \cos b - \sin\gamma \sin b \cos\beta}{\sqrt{1 - \cos^2 \delta_{dist}(\gamma)}}$$

It is equal to zero when

$$\tan\gamma = \tan b \cos\beta$$

The previous equation has two solutions : $\widehat{\gamma} = \arctan(\tan b \cos\beta)$ and $\widehat{\gamma} + \pi$. To identify the minimum and the maximum, the second derivative has to be computed:

$$\frac{d^2\delta_{dist}}{d\gamma^2}(\gamma) = \frac{\cos\delta_{dist}(\gamma)}{\sqrt{1 - \cos^2 \delta_{dist}(\gamma)}} + \frac{\cos\delta_{dist}(\gamma)\big(\sin\gamma\cos b - \sin\gamma\sin b\cos\beta\big)^2}{\Big(1 - \cos^2\delta_{dist}(\gamma)\Big)^{3/2}}$$

Its value for $\gamma = \widehat{\gamma}$ is:

$$\frac{d^2\delta_{dist}}{d\gamma^2}(\widehat{\gamma}) = \frac{\cos\delta_{dist}(\gamma)}{\sqrt{1 - \cos^2 \delta_{dist}(\gamma)}}$$

The denominator is always positive, so its sign depends on the sign of $\cos\delta_{dist}$. From equation (5.1),it can be notice that

$$\cos\delta_{dist}(\widehat{\gamma}+\pi) = -\cos\delta(\widehat{\gamma})$$

Thus, if δ_{dist} has its minimum at $\widehat{\gamma}$, it has its maximum value at $\widehat{\gamma}+\pi$ or vice versa. It is possible to define a function $fun(\gamma)$ equal to the difference between δ and $\delta_{admissible}$:

$$fun(\gamma) = \arccos\cos\gamma\cos b + \sin\gamma\sin b\cos\beta - \delta_{admissible} \tag{5.2}$$

Also this function has a global minimum and a global maximum at the same γ values associated to the minimum and the maximum of $\delta_{dist}(\gamma)$. It is evident that, if $fun(\gamma) > 0$ for every value of γ, there is no intersection between the manoeuvre plane and the Sun cone. On the contrary, the range of γ values, for which $fun(\gamma) < 0$, identifies the forbidden directions. This range will be centered at the value $\widehat{\gamma}$ for which fun has its minimum fun_{min}; its extremes are the function roots γ_1 and γ_2. In order to find them, the Newton method (see Appendix A) can be adopted.

Once γ_1 and γ_2 have been determined, they are exploited to compute the largest angle of inclination of $\mathbf{\Delta V}$ with respect to $\mathbf{N}$. Actually two angles are determined: $\gamma_+ \in [0, \gamma_{max}]$ computed in the same way of γ, that will be exploited in case $\Delta V_N > 0$; $\gamma_- \in [0, \gamma_{max}]$, that is computed positive from $-N$ toward $\mathbf{T}$ on the $\mathbf{TN}$ plane and that will be used if $\Delta V_N < 0$. The value $\gamma_{max} \in [0, \frac{\pi}{4}]$ depends on the analysed mission. It is defined as a function of the smallest out-of-plane ΔV, $\widehat{\Delta V}_{N_{min}}$, and the largest in-plane ΔV, $\widehat{\Delta V}_{T_{max}}$, resulting from the manoeuvres plan calculated by AOC before the integration of the mixed manoeuvres:

$$\gamma_{max} = \arctan\frac{\Delta V_{T_{max}}}{\Delta V_{N_{min}}} + 2^\circ$$

The value of 2° is added as a margin. The largest value that can be imposed to γ_{max} is $\frac{\pi}{4}$: indeed, the tangential component of a mixed manoeuvre is always significantly smaller than the out-of-plane one. For the computation of both γ_- and γ_+, γ_1 and γ_2 are adjusted in such a way to have the right extreme smaller than the left one. Indeed, since γ is defined in $[0, 2\pi]$, γ_1 could be greater than γ_2. For the determination of γ_+, if $\gamma_1 > \gamma_2$ γ_1 is redefined as $\gamma_1 = 2\pi - \gamma_1$. Then, γ_+ is defined as follows:

- if $\gamma_1 < 0$, since every manoeuvre surrounding $\mathbf{N}$ would intersect the Sun cone:

$$\gamma_+ = 0;$$

- otherwise,

$$\gamma_+ = min(\gamma_1, \gamma_{max})$$

For the computation of γ_-, if $\gamma_1 > \gamma_2$, γ_2 is redefined as $\gamma_1 = 2\pi + \gamma_2$. Then, γ_- is determined as follows:

- if $\gamma_1 < \pi < \gamma_2$, since every manoeuvre surrounding $-N$ would intersect the Sun cone:

$$\gamma_- = 0;$$

- if $\gamma_2 < \pi$,

$$\gamma_- = min(\pi - \gamma_2, \gamma_{max})$$

- if $\gamma_1 > \pi$

$$\gamma_+ = \gamma_{max}$$

Of course, the values γ_+ and γ_- are both imposed equal to γ_{max} in the case of a solar eclipse or if no intersection between the Sun cone and the manoeuvres plane occurs.

To reduce the risk linked to computational errors, the described procedure is executed considering the value $\delta_{admissible}$ increased by 0.1°.

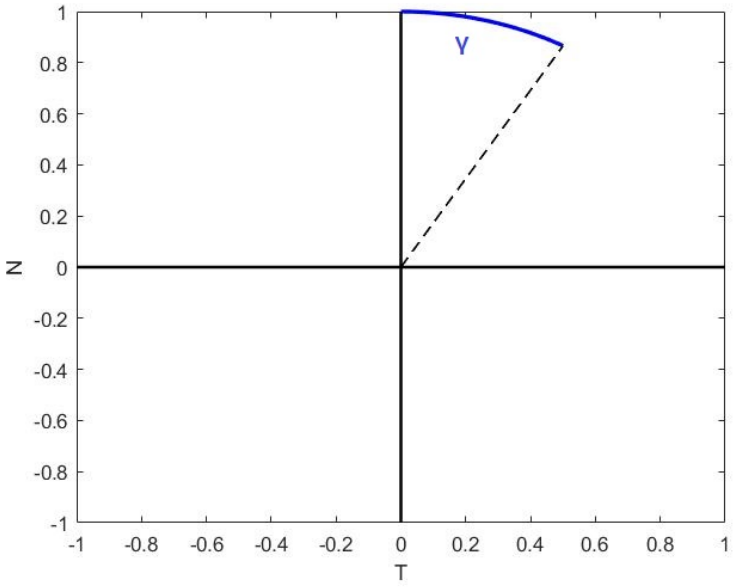

Fig. 5.1: γ angle : inclination of the mixed ΔV with respect to the out-of-plane direction

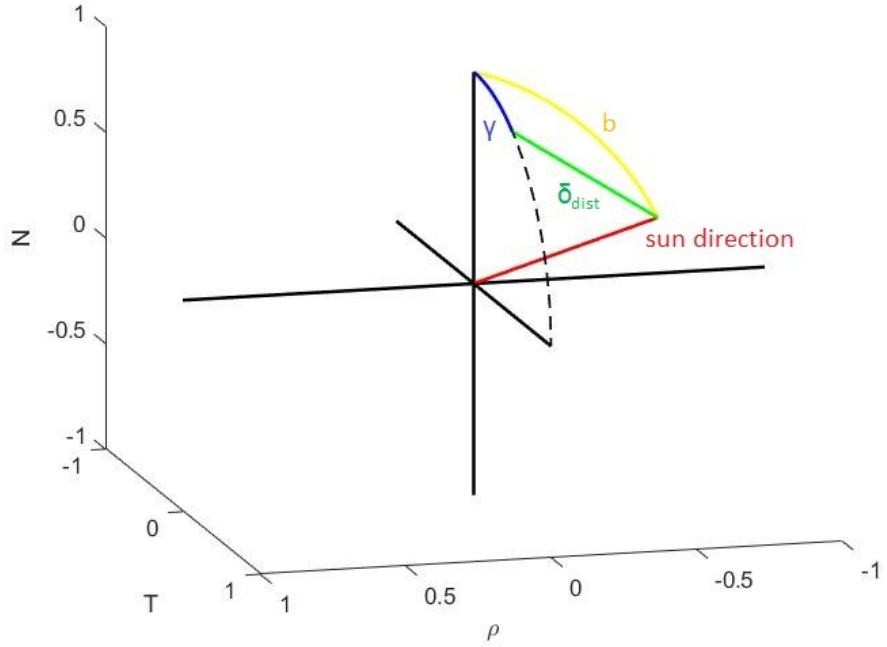

Fig. 5.2: analysed spherical trigonometry problem

5.4 Slots definition

As already introduced in Section 5.2, at each mixed manoeuvre slot a value γ_+ and a value γ_- will be associated. In this way, AOC will be able to compute the largest value of the ΔV_T component as either $\Delta V_{T_{max}} = \Delta V_N \tan\gamma_+$, if $\Delta V_N > 0$, or $\Delta V_{T_max} = |\Delta V_N| \tan\gamma_-$, otherwise.

The values of both γ_+ and γ_- vary in time. Thus, they are evaluated at about each 3° along one slot. With the assumption of a quasi circular orbit, 3° corresponds to a duration of

$$\Delta t = \frac{n\Delta t_{tot}}{3}\frac{180}{\pi}$$

being δt_{tot} the total duration of the analysed slot. The considered orbit is the reference one: the

satellite state is evaluated by means of the Eckstein and Hechler's analytic propagation method [16], that takes into account only the perturbations linked to the Earth gravity field and, more in particular, to the terms J_2, J_3, J_4, J_5 and J_6. To avoid the risk of instrument glare at each time during one slot, the values of associated γ_+ and γ_- are the smallest computed. This is the reason for which, even if the analysed slots are the out-of-plane manoeuvres ones, the mixed slots do not necessarily correspond to them. Indeed, even a small variation of both γ_+ and γ_- can determine an important variation of ΔV_{T_max}, since this last has the trend of $\tan\gamma_{+,-}$, for a fixed value of ΔV_N. Having $\gamma_{-,+} < 45°$, $\Delta\tan\gamma_{-,+}$ is about 0.1 each 5°. Then, important variations can be occur also if a solar eclipse occurs during part of the slot. In order not to be too restrictive in the definition of ΔV_{T_max}, the initial slots are divided. However, this operation is handled in such a way to minimise the total number of slots. Indeed, the duration of the slot has an impact on the total value of ΔV that can be physically be imposed by the propulsive system, above all in case of low thrust. Moreover, as the number of slots increases, the computational time increases, as already explained in Section 5.2. Finally, it has to be considered that usually $\Delta V_T << \Delta V_N$; so, even a small value of $\tan\gamma_{+,-}$ could allow the mixed manoeuvre. Therefore, it is imposed that each slot cannot be divided into slots whose duration is less than one third of the original one. Moreover, the division of the slots is triggered by a variation of γ_+ or γ_- larger that 10°.

5.5 Results

The described procedure is carried out for the analysed missions (see Section 2.4), to determine the temporal slots during which mixed manoeuvres can be performed, starting from the already existing out-of-plane manouevres slots. In Table 5.1, the obtained results are reported: the largest angle γ_{max} and the number of determined mixed manoeuvres slots compared to the out-of-plane manoeuvres slots number. It is possible to observe that the mixed manoeuvres slots correspond exactly to the out-of plane manoeuvres ones for missions A1, A2 and B1. The reason is that their maximum angle γ_{max} is small. The slots increment of missions B2, D1 and D2 has the same order of magnitude. This is a demonstration that the implemented procedure assures sufficiently accurate results. Indeed, these missions are characterised by the same type of orbits: sun-synchronous orbits.

Table 5.1: Results concerning the generation of mixed manoeuvres slots

mission	γ_{max}	number of out-of-plane manoeuvres slots	number of mixed slots
A1 chemical	10.21°	11750	11750
A2 chemical	7.916°	11750	11750
B1 chemical	4.103°	11397	11397
B2 chemical	45°	14131	17807
D1 chemical	45°	10979	14453
D2 chemical	45°	10979	14453
F chemical	45°	10738	11773

Chapter 6

Perturbations effects over the inclination

6.1 AOC necessary improvements

The results obtained after the integration done show the need of performing mixed in-track cross-track manoeuvres in order to obtain better performance. However, for some analysed missions, this integration is not sufficient to fulfill the targeted constraints in terms of station keeping performance (see Table 2.4). Other improvements can be implemented.

In Chapter 2, it was shown that the manoeuvres computation depend on the evaluation of two parameters $\Delta\ddot{\alpha}_{targeted}$ and di/dt, both functions of the orbital perturbations. The acceleration of the argument of latitude is evaluated on the basis of the values of this orbital parameter at previous orbital nodes and considering it constant during the predictable horizon and the research horizon. The long period inclination drift is approximated by summing the contribution caused by the solar potential perturbation and the one due to the terrestrial tides and the atmospheric drag. This last is evaluated as an approximated average value. The measures of Δi at the previous ascending nodes are used. At each node, the drift caused by the terrestrial tides and the atmospheric drag is computed by determining the total inclination drift during one orbital period and by subtracting from it the known long period contributions due to the solar and lunar potential perturbations. Then, all the obtained values are used to compute the mean. The overall operation has an important impact on the computational time of AOC: it slows down the computation of the out-of-plane manoeuvres.

A better estimation of the $\Delta\ddot{\alpha}_{targeted}$ and di/dt could imply an important improvement of the AOC controller.

During the last period of the internship, a study of the perturbations effect on the orbital inclination has been conducted, with main objective of determining an analytic, sufficiently accurate model of the drift. This objective is linked to the need of improving the inclination drift estimation, reducing as much as possible the computational time.

6.2 Perturbing forces effects on the orbital inclination

The perturbations that cause long period variations of the orbital inclination are the solar and lunar potentials, the atmospheric drag and the solar radiation pressure (see Table 1.1). Moreover, experimentally it has been observed that also the terrestrial tides have a long period impact on the inclination drift. However, the impact of each perturbation contribution changes according to the type of orbit. This is evident from the simulations carried out to obtain the free parameters evolution under the effects of the different perturbations. In particular, missions A2, B2, D1, and F are taken into account because they allow to analyse the sample of orbits of most interest for AOC. The same numerical propagator used to simulate the orbital dynamics to test AOC has been exploited to obtain the orbital parameters evolution in time, if no orbital control is performed. In particular, the perturbations have been considered both together and separately. Figures 6.1-6.23 show the results of the

simulations. In the figures, the blue line is refereed to the orbital parameters evolution considering only the orbital ascending nodes; the red line is relative to all the other orbital points. The effects of the geopotential are always simulated because they are included in the reference orbit. Moreover, this perturbation has no impact on the secular inclination drift: the Δi trend does not depend on it. Including the geopotential effects enables also to show the dependence of $\Delta\Omega$ on the inclination drift. Because of this perturbation, the secular $\Delta\dot{\Omega}$ depends on Δi: if the secular inclination drift is null, $\Delta\Omega$ has a linear drift; if the secular drift is constant, $\Delta\Omega$ has a quadratic trend. A secular variation of the right ascension of the ascending node due to the solar potential should also be considered for certain kinds of sun-synchronous orbits, but it can be neglected in first approximation.

The conducted simulations show that the effects of the solar radiation pressure on the inclination drift are always almost null: the period of the inclination variations is very long and the drift contribution is very small. Thus, this perturbation effects will be neglected in this study. The lunar potential imposes a long period variation. Thus, the lunar potential has no impact on the secular drift. Moreover, the characteristic period is lower than that of the periodical effects caused by other perturbations. The solar potential is the perturbation with the most significant effects. In general, it imposes long period variations; for some kinds of sun-synchronous orbits (see mission D1 and A2), it causes a secular drift. However, in order to correctly estimate the inclination drift, it is not sufficient to consider the solar potential effects: the terrestrial tides and the atmospheric drag contributions cannot be neglected. As the solar potential, the terrestrial tides cause a secular drift for some kinds of sun-synchronous orbits. On the contrary, the atmospheric drag generates always a secular inclination drift. Indeed, if the dawn orbit of mission B2 is taken into account, the main contribution to the inclination variation is caused by this perturbation. Also the orbit of mission F is subjected to a secular inclination drift due to the atmospheric drag. However, the variation is very slow and very slight in this case: the orbital altitude is high and the perturbation effects are reduced. Thus, if a sufficiently high orbit is analysed, like that of mission F or mission E (see Figure 6.24), only in this case it is possible to neglect the atmospheric drag as perturbation.

The conducted analysis confirms that, to determine the secular or the long period inclination drift, the focus has to be on the effects of three main orbital perturbations: the solar potential, the terrestrial tides and the atmospheric drag. These perturbations effects were already considered in the AOC original algorithm. However, only the analytic models of the solar and lunar potential contributions were implemented. An analytical and semi-analytical models relative the terrestrial tides and the atmospheric drag effects have been introduced. In the case of the terrestrial tides, the model has been determined on the basis of several works found in literature. In the case of the atmospheric drag, the King-Hele model has been exploited. Moreover, for sun-synchronous orbits, a standard analytic model of the secular contribution to the drift has been introduced as an alternative to the already implemented long-period contribution model. Finally, also a study concerning the lunar potential has been carried out to conceive an analytic model taking into account only the longest period contributions to the drift, which can have a non-neglecting impact. More details are provided in the following sections.

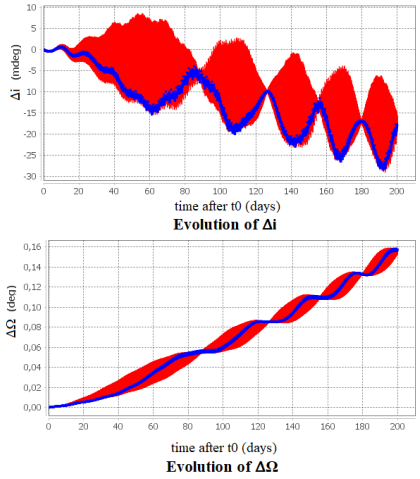

Fig. 6.1: Mission A2 - all perturbing forces effects

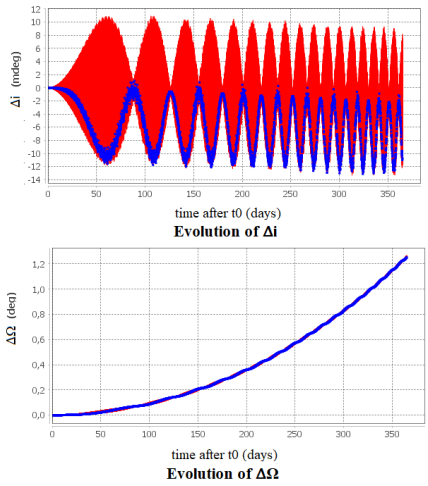

Fig. 6.2: Mission A2 - geopotential and atmospheric drag effects

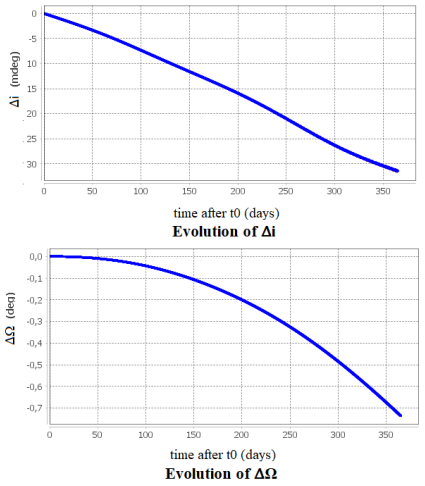

Fig. 6.3: Mission A2 - geopotential and solar potential effects

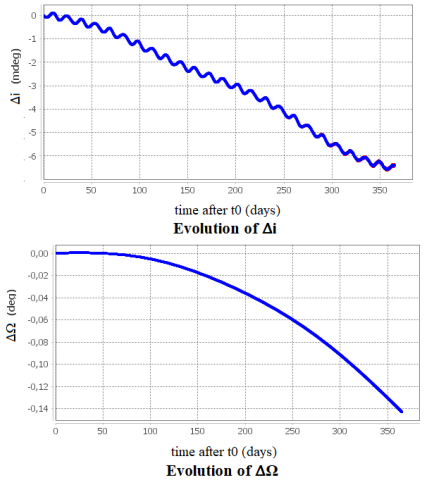

Fig. 6.4: Mission A2 - geopotential and terrestrial tides effects

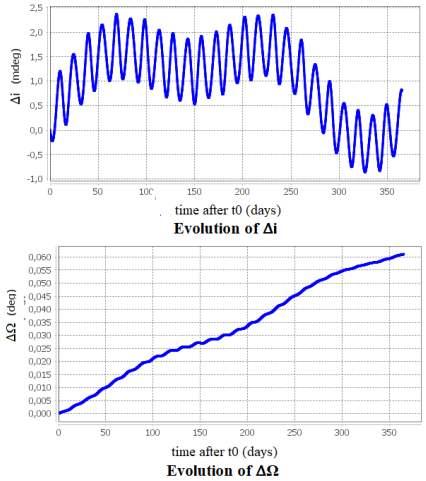

Fig. 6.5: Mission A2 - geopotential and lunar potential effects

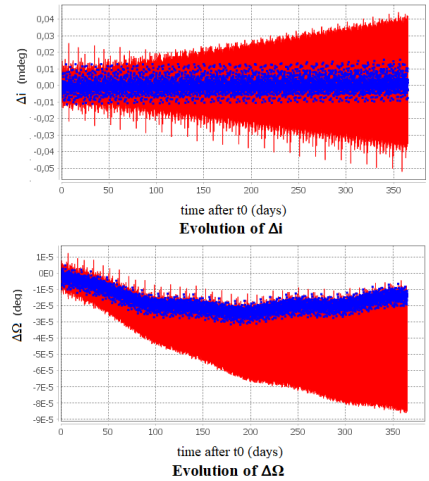

Fig. 6.6: Mission A2 - geopotential and solar radiation pressure effects

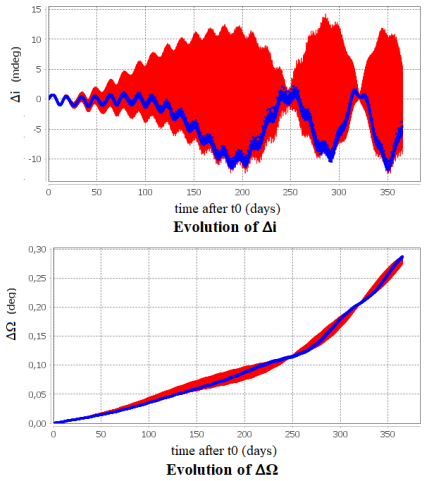

Fig. 6.7: Mission B2 - all perturbing forces effects

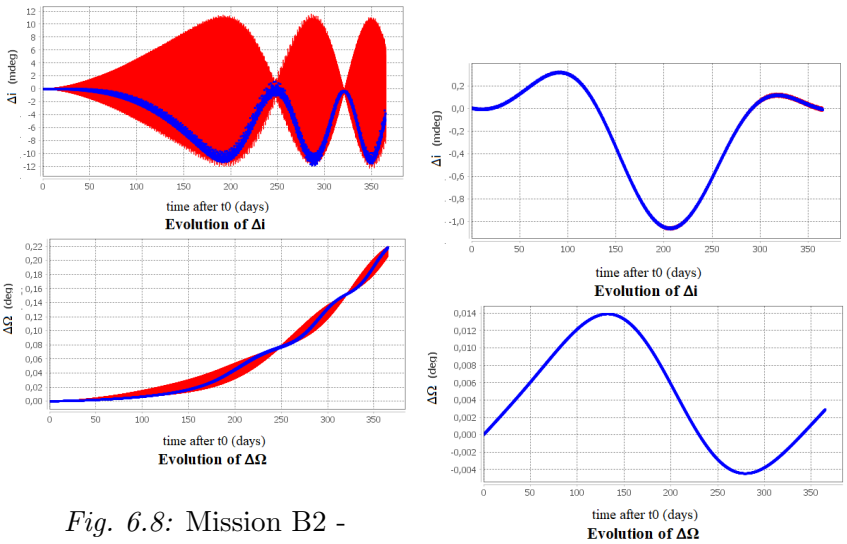

Fig. 6.8: Mission B2 - geopotential and atmospheric drag effects

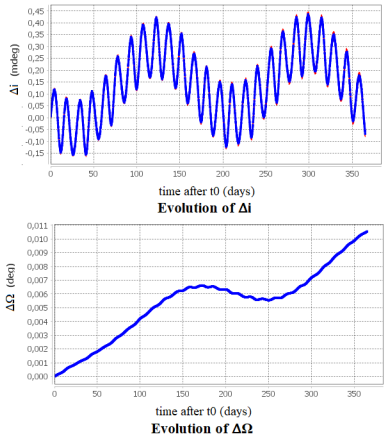

Fig. 6.9: Mission B2 - geopotential and terrestrial tides effects

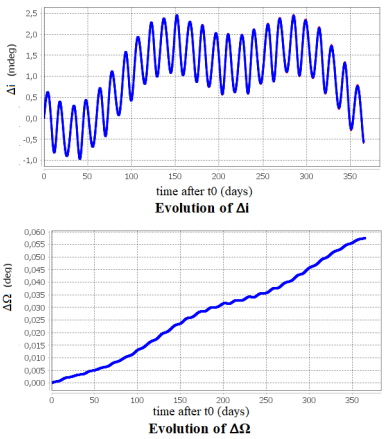

Fig. 6.10: Mission B2 - geopotential and lunar potential effects

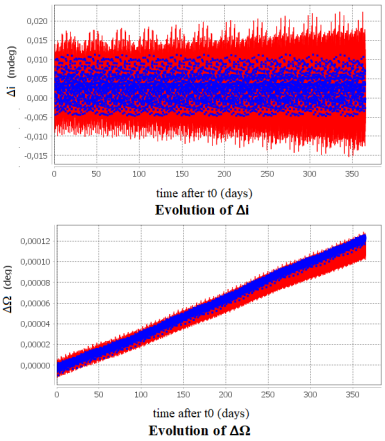

Fig. 6.11: Mission B2 - geopotential and solar radiation pressure effects

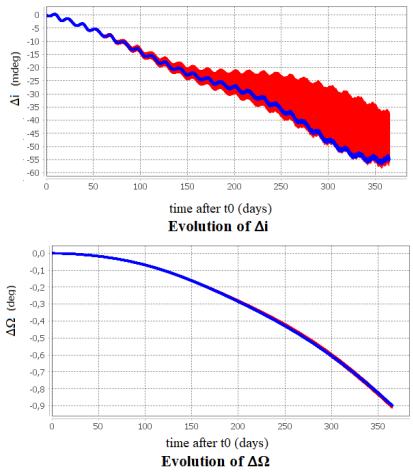

Fig. 6.12: Mission D1 - all perturbing forces effects

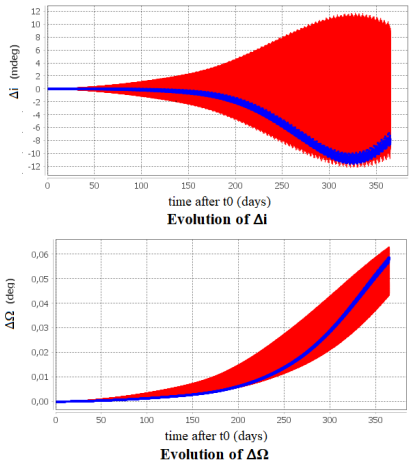

Fig. 6.13: Mission D1 - geopotential and atmospheric drag effects

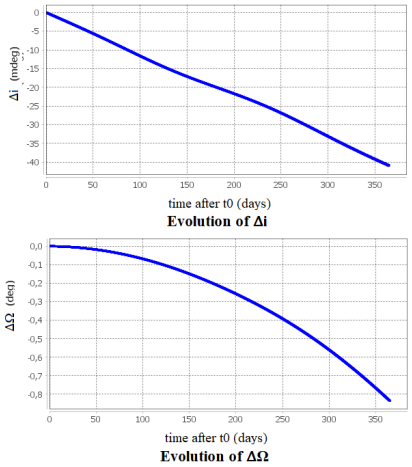

Fig. 6.14: Mission D1 - geopotential and solar potential effects

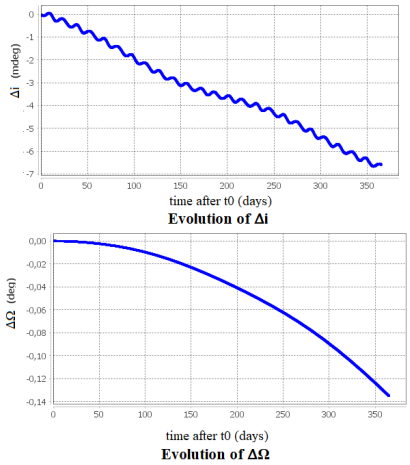

Fig. 6.15: Mission D1 - geopotential and terrestrial tides effects

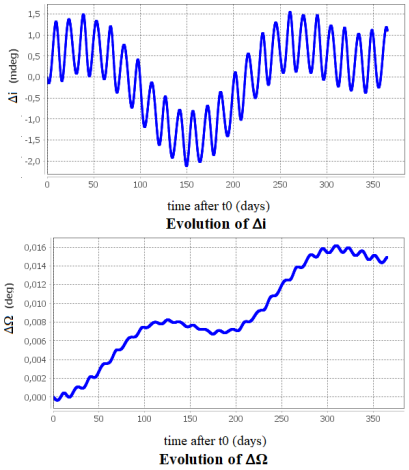

Fig. 6.16: Mission D1 - geopotential and lunar potential effects

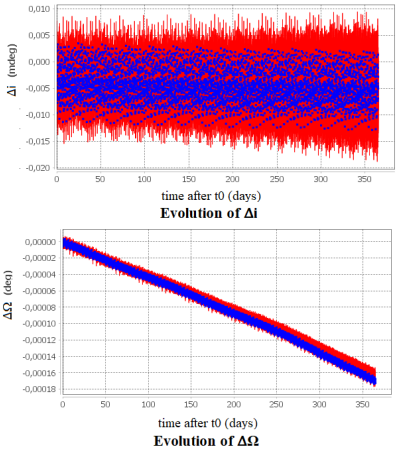

Fig. 6.17: Mission D1 - geopotential and solar radiation pressure effects

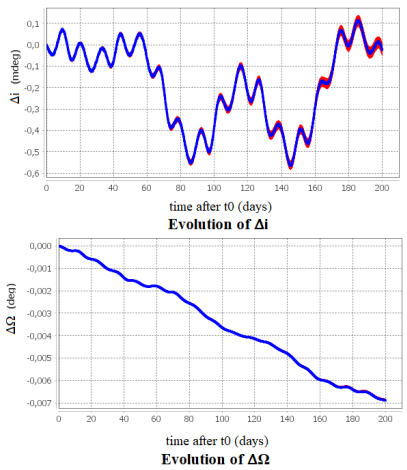

Fig. 6.21: Mission F - geopotential and terrestrial tides effects

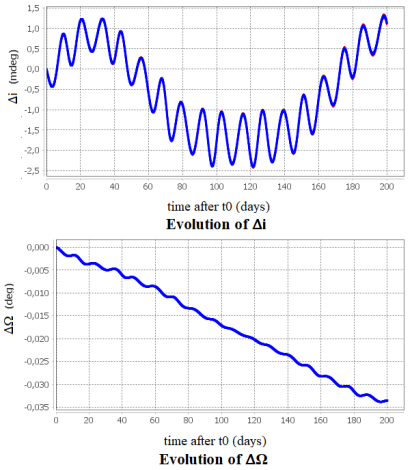

Fig. 6.22: Mission F - geopotential and lunar potential effects

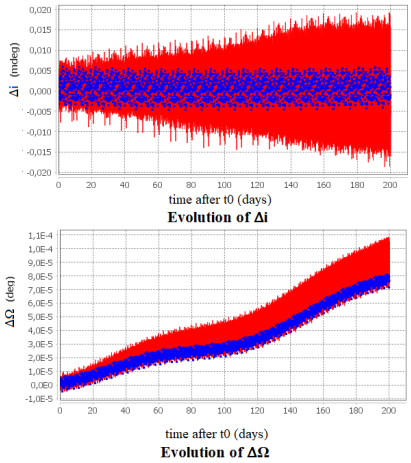

Fig. 6.23: Mission F - geopotential and solar radiation pressure effects

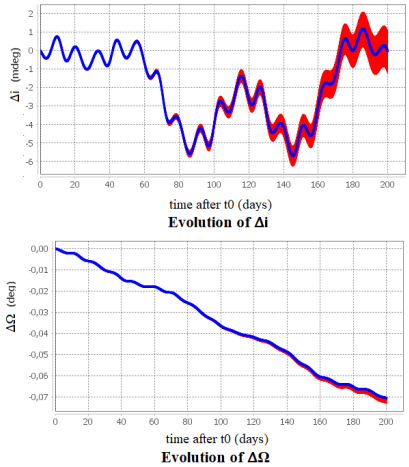

Fig. 6.18: Mission F - all perturbing forces effects

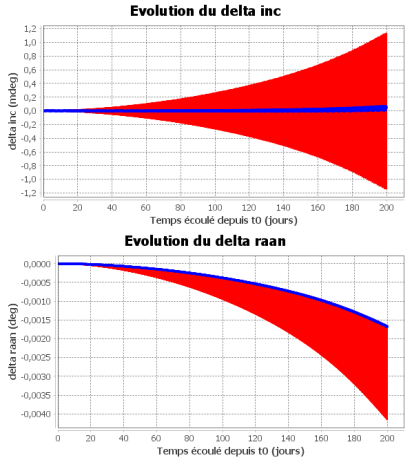

Fig. 6.19: Mission F - geopotential and atmospheric drag effects

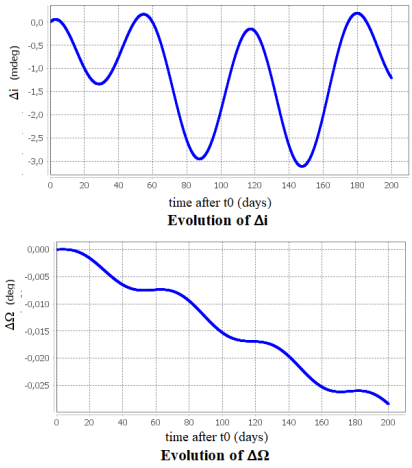

Fig. 6.20: Mission F - geopotential and solar potential effects

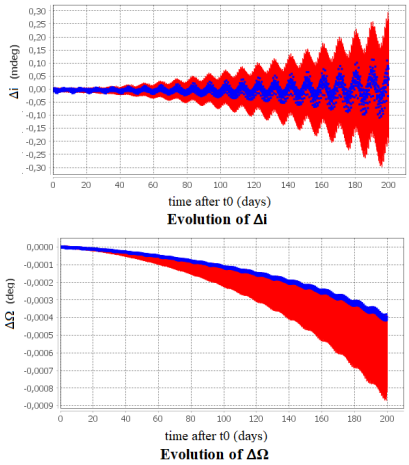

Fig. 6.24: Mission E - geopotential and atmospheric drag effects

6.3 Solar potential effects

A satellite S is subjected not only to the Earth gravitational attraction, but also to the gravitational attraction of other celestial bodies, mainly the Sun and the Moon. Let be A the considered celestial body and M_A its mass (Figure 6.25). Because of it, the satellite S is subjected to an acceleration $\mathbf{a}_{p_A}$ equal to:

$$\mathbf{a}_{p_A} = GM_A\Big(\frac{\mathbf{SA}}{\rho_A^3} - \frac{\mathbf{OA}}{r_A^3}\Big) \tag{6.1}$$

where:

- O is the central body, so the Earth;
- ρ_A is the distance between the S and A;
- r_A is the distance between A and the Earth.

This acceleration is due to the potential V_A :

$$V_A = GM_A\Big(\frac{1}{\rho_A} - \frac{\mathbf{OSOA}}{r_A^3} - \frac{1}{r_A}\Big) \tag{6.2}$$

(see [16]). This potential can be expressed in two different ways.

Cook [22] writes it as a function of the satellite and the celestial bodies coordinates in the reference frame $\mathbf{R}, \theta, \mathbf{N}$. By computing its gradient, it is possible to obtain the perturbing acceleration components in the Gaussian reference frame and apply the Gauss equations in order to estimate the inclination drift. This is the procedure followed in [21]. Here, the inclination drift is then integrated over an orbital period to obtain its long period contribution. The result is the long period inclination drift in equation (2.29).

Another way to write the potential V_A is that adopted by Kaula [23]. As $r < r_A$, where r is the satellite distance from the Earth, it is possible to express $1/\rho_A$ by means of a Legendre polynomials development and to write:

$$V_A = \frac{GM_A}{r_A}\sum_{l=2}^{\infty}\Big(\frac{r}{r_A}\Big)^l P_l(\cos\theta_A)$$

where θ_A is the angle between **OA** and **OS**. By exploiting the Legendre polynomials properties, it can be found:

$$V_A = \frac{GM_A}{r_A}\sum_{l=2}^{\infty}\Big(\frac{r}{r_A}\Big)^l \sum_{m=1}^{l} k_m \frac{(l-m)!}{(l+m)!} P_{lm}(\sin\delta)P_{lm}(\sin\delta_A)(\cos m\alpha^* \cos m\alpha_A^* + \sin m\alpha^* \sin m\alpha_A^*) \tag{6.3}$$

where $k_m = 1$ if $m = 0$, $k_m = 2$ otherwise, and:

- δ and $\alpha*$ are the satellite declination and right ascension;
- δ_A and α_A* are the three body declination and right ascension;
- $P_{lm}(x)$ is the Lagrange function.

In order to write the potential as a function of the orbital parameters, Kaula expresses each potential contribution V_{A_l} as :

$$V_{A_l} = \frac{GM_A r^l}{r_A^{l+1}}\sum_{m=0}^{l} k_m \frac{(l-m)!}{(l+m)!}\sum_{p=0}^{l} F_{lmp}(i)C_{lmp} \tag{6.4}$$

$$C_{lmp} = \begin{bmatrix} A_{lm} \\ -B_{lm} \end{bmatrix}_{(l-m)_{odd}}^{(l-m)_{even}} \cos\left[(l-2p)\alpha + m\Omega\right] + \begin{bmatrix} B_{lm} \\ A_{lm} \end{bmatrix}_{(l-m)_{odd}}^{(l-m)_{even}} \sin\left[(l-2p)\alpha + m\Omega\right]$$

$$A_{lm} = P_{lm}(\sin\delta_A)\cos m\alpha_A^*$$

$$B_{lm} = P_{lm}(\sin\delta_A)\sin m\alpha_A^*$$

$F_{lmp}(i)$ is the Kaula inclination function:

$$F_{lmp}(i) = \sum_{t=0}^{min(p,k)} \frac{(2l-2t)!}{t!(l-t)!(l-m-2t)!2^{2l-2t}} \sin^{l-m-2t} i \sum_{s=0}^{m} \begin{pmatrix} m \\ s \end{pmatrix} \cos^s i \sum_c \begin{pmatrix} l-m-2t+s \\ c \end{pmatrix} \begin{pmatrix} m-s \\ p-t-c \end{pmatrix} (-1)^{c-k} \tag{6.5}$$

where k is the integer part of $(l-m)/2$ and c is summed over all the values making the binomial coefficients nonzero. In Figure 6.26, the table reported from [24], with all the values of $F_{lmp}(i)$ for $l \in [2,4]$, is shown. In a similar way, the potential expression can be modified again to express it as a function of the third body orbital elements. So, each potential contribution can be expressed as:

$$V_{A_l} = \frac{GM_A r^l}{r_A^{l+1}} \sum_{m=0}^{l} k_m \frac{(l-m)!}{(l+m)!} \sum_{p=0}^{l} \sum_{h=0}^{l} F_{lmp}(i) F_{lmh}(i_A) \cos\left[(l-2p)\alpha - (l-2h)\alpha_A + m(\Omega - \Omega_A)\right] \tag{6.6}$$

The potential contribution with the greatest influence is the one associated to $l = 2$ [16]. In particular, from the obtained expression, applying the simplifying hypothesis of quasi circular orbit and considering the Lagrangian equation (1.35), it is evident that the long period inclination drift is due to the contributions associated to $l - 2p = 0$ and $m \neq 0$. If the third body is the Sun and the considered orbit is sun-synchronous, the drift has a secular component for $l - 2h = m$ since $\Omega - \alpha_A$ is constant (in the case of non circular orbit, it is possible to express the solar orbit argument of latitude as a function of the mean anomaly, and even in this case the constant term appears). Considering the main potential contribution associated to $l = 2$, the inclination secular drift can be found for $m = 2$, $p = 1$ and $h = 0$. Its expression has been already introduced in equation (3.3) in Chapter 3. In view of this equation, it can be observed that the secular drift is zero for sun-synchronous orbits whose local hour is 6 h, 12 h, 18 h or 24 h: this is the reason a secular inclination variation is not observed in mission B2.

In the case of sun-synchronous orbits, AOC could exploit the secular inclination drift model in equation (3.3) instead of the Lamy-Azema model (equation (2.29)), to filter the long period variations. The secular drift has been determined for mission D1 orbit and compared to that obtained from the simulation. This last one is computed by means of a least squares fit, with a linear polynomial model. The relative error is 0.0019% (see Figure 6.27).

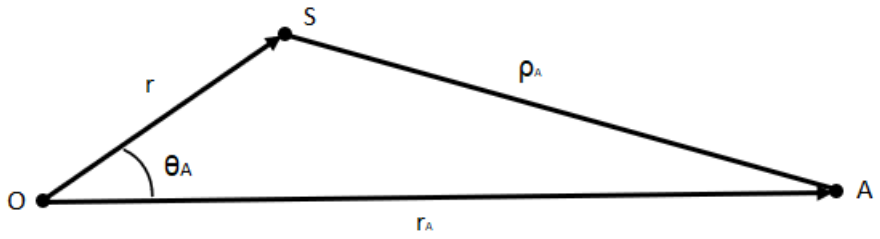

Fig. 6.25: Three Body potential perturbation: geometry of the problem

Inclination Functions $F_{lmp}(i)$

l	m	p	$F_{lmp}(i)$
2	0	0	$-3 \sin^2 i/8$
2	0	1	$3 \sin^2 i/4 - 1/2$
2	0	2	$-3 \sin^2 i/8$
2	1	0	$3 \sin i(1 + \cos i)/4$
2	1	1	$-3 \sin i \cos i/2$
2	1	2	$-3 \sin i(1 - \cos i)/4$
2	2	0	$3(1 + \cos i)^2/4$
2	2	1	$3 \sin^2 i/2$
2	2	2	$3(1 - \cos i)^2/4$
3	0	0	$-5 \sin^3 i/16$
3	0	1	$15 \sin^3 i/16 - 3 \sin i/4$
3	0	2	$-15 \sin^3 i/16 + 3 \sin i/4$
3	0	3	$5 \sin^3 i/16$
3	1	0	$-15 \sin^2 i(1 + \cos i)/16$
3	1	1	$15 \sin^2 i(1 + 3 \cos i)/16 - 3(1 + \cos i)/4$
3	1	2	$15 \sin^2 i(1 - 3 \cos i)/16 - 3(1 - \cos i)/4$
3	1	3	$-15 \sin^2 i(1 - \cos i)/16$
3	2	0	$15 \sin i(1 + \cos i)^2/8$
3	2	1	$15 \sin i(1 - 2 \cos i - 3 \cos^2 i)/8$
3	2	2	$-15 \sin i(1 + 2 \cos i - 3 \cos^2 i)/8$
3	2	3	$-15 \sin i(1 - \cos i)^2/8$
3	3	0	$15(1 + \cos i)^3/8$
3	3	1	$45 \sin^2 i(1 + \cos i)/8$
3	3	2	$45 \sin^2 i(1 - \cos i)/8$
3	3	3	$15(1 - \cos i)^3/8$
4	0	0	$35 \sin^4 i/128$
4	0	1	$-35 \sin^4 i/32 + 15 \sin^2 i/16$
4	0	2	$(105/64) \sin^4 i - (15/8) \sin^2 i + 3/8$
4	0	3	$-(35/32) \sin^4 i + (15/16) \sin^2 i$
4	0	4	$(35/128) \sin^4 i$
4	1	0	$-(35/32) \sin^3 i(1 + \cos i)$
4	1	1	$(35/16) \sin^3 i(1 + 2 \cos i) - (15/8)(1 + \cos i) \sin i$
4	1	2	$\cos i(15 \sin i/4 - 105 \sin^3 i/16)$
4	1	3	$-(35/16) \sin^3 i(1 - 2 \cos i) + (15/8) \sin i(1 - \cos i)$
4	1	4	$(35/32) \sin^3 i(1 - \cos i)$
4	2	0	$-(105/32) \sin i(1 + \cos i)^2$
4	2	1	$(105/8) \sin^2 i \cos i(1 + \cos i) - (15/8)(1 + \cos i)^2$
4	2	2	$(105/16) \sin^2 i(1 - 3 \cos^2 i) + (15/4) \sin^2 i$
4	2	3	$-(105/8) \sin^2 i \cos i(1 - \cos i) - (15/8)(1 - \cos i)^2$
4	2	4	$-(105/32) \sin^2 i(1 - \cos i)^2$
4	3	0	$(105/16) \sin i(1 + \cos i)^3$
4	3	1	$(105/8) \sin i(1 - 3 \cos^2 i - 2 \cos^3 i)$
4	3	2	$-(315/8 \sin^3 i \cos i$
4	3	3	$-(105/8) \sin i(1 - 3 \cos^2 i + 2 \cos^3 i)$
4	3	4	$-(105/16) \sin i(1 - \cos i)^3$
4	4	0	$(105/16)(1 + \cos i)^4$
4	4	1	$(105/4) \sin^2 i(1 + \cos i)^2$
4	4	2	$(315/8) \sin^4 i$
4	4	3	$(105/4) \sin^2 i(1 - \cos i)^2$
4	4	4	$(105/16)(1 - \cos i)^4$

Fig. 6.26: Kaula inclination function [24]

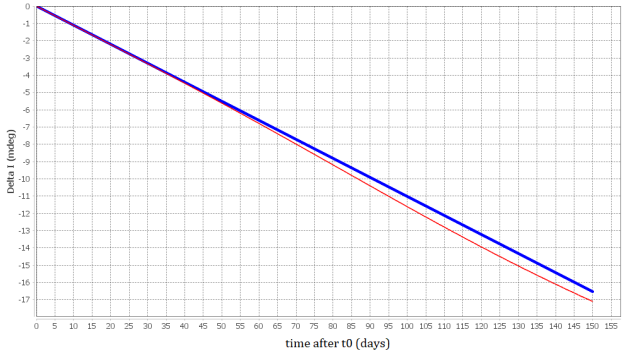

Fig. 6.27: Free evolution of Δi under the effects of the solar gravitational potential, compared with the trend obtained exploiting the secular drift analytic model evaluated at the beginning of the simulation (mission D1)

6.4 Terrestrial tides

A third body generates a perturbation on a satellite-Earth system: its effects on the orbital inclination have been discussed in the previous section. The perturbing force acting on the satellite is due the different gravitational attractions that the third body imposes on it and on the Earth. The same

principle explains the terrestrial tides. The third body (mainly the Sun and the Moon) induces an attraction force acting on the different parts on the planet. The variation of its gravitational attraction on the Earth center and the crust causes the deformation force generating the terrestrial tides. It's possible to apply the same logic of the previous section in order to determine the perturbing potential causing these deformations. Considering Figure 6.25, in this case the point S doesn't represent a satellite, but a point of the Earth crust. The perturbing potential is expressed by:

$$V_p = GM_A\Big(\frac{1}{\rho_A} - \frac{\mathbf{OSOA}}{r_A^3} - \frac{1}{r_A}\Big)$$

Exploiting the Legendre functions, it can be expressed as:

$$V_p = GM_A \sum_{l=2}^{\infty} \frac{r^l}{r_A^{l+1}} \sum_{m=0}^{l} k_m \frac{(l-m)!}{(l+m)!} P_{lm}(\sin\phi) P_{lm}(\sin\delta_A)(\cos m\lambda \cos m(\alpha_A^* - \theta_G) + \sin m\lambda \sin m(\alpha_A^* - \theta_G))$$

$$k_m = \begin{cases} 1 & m = 0 \\ 2 & otherwise \end{cases}$$

where θ_G is the sidereal time (angle between the **I** axis and the Greenwich meridian) and λ and ϕ are the longitude and the latitude of the point S. The angle $\lambda_A = \alpha_A^* - \theta_G$ is the third body longitude. Thus, the potential is characterised by several contributions:

$$V_p = \sum_{l=0}^{\infty} V_{p_l}$$

If the Earth was fluid, each contribution would act as a perturbing potential causing a movement ξ, supposed radial, such that:

$$U(r + \xi; \lambda, \phi) + V_{p_l} = U(r; \lambda, \phi)$$

$$\xi = \frac{-V_{p_l}}{\frac{\partial U}{\partial r}} \approx \frac{V_{p_l}}{g_0}$$

$$g_0 = \frac{\mu}{R_e^2}$$

Assuming the hypothesis of an elastic planet, the crust deformation is proportional to ξ, so to V_{p_l}. This is the first hypothesis of Love, who modeled the problem in order to obtain an approximation of the geopotential variation due to the terrestrial tides. Precisely, his first hypothesis consists in the assumption that the crust elevation is given by:

$$\eta_l = h_l \frac{V_{p_l}}{g_0}$$

where h_l, $l \in [2, \infty]$, are constants. Supposing that the Earth is characterised by an initial homogeneous density, from this first hypothesis, Love formulates a second hypothesis. He hypothesizes that the variation of the Earth potential due to the deformations is proportional to the perturbing potential:

$$\Delta U_l(R_e) = k_l V_{p_l}$$

where k_l are constants called Love numbers. Evidently, this variation of the geopotential causes an additional perturbation on a satellite orbit. In [16], the variation of the geopotential at a distance $r > R_e$ from the Earth center is approximated in the following way:

$$\Delta U_l(r) = \Big(\frac{R_e}{r}\Big)^{l+1} \Delta U_l(R_e) = k_l \Big(\frac{R_e}{r}\Big)^{l+1} V_{p_l}(R_e) \tag{6.7}$$

Consequently, the perturbing potential acting on a satellite due to the terrestrial tides can be expressed as:

$$V_T = GM_A \sum_{l=2}^{\infty} k_l \frac{R_e^{2l+1}}{r_A^{l+1} r^{l+1}} \sum_{m=1}^{l} k_m \frac{(l-m)!}{(l+m)!} P_{lm}(\sin\phi) P_{lm}(\sin\delta_A)(\cos m\lambda \cos m(\alpha_A^* - \theta_G) + \sin m\lambda \sin m(\alpha_A^* - \theta_G)) \tag{6.8}$$

or, considering that

$$\phi = \delta$$

$$\lambda = \alpha^* - \theta_G$$

as:

$$V_T = GM_A \sum_{l=2}^{\infty} k_l \frac{R_e^{2l+1}}{r_A^{l+1} r^{l+1}} \sum_{m=1}^{l} k_m \frac{(l-m)!}{(l+m)!} P_{lm}(\sin\delta) P_{lm}(\sin\delta_A)(\cos m\alpha^* \cos m\alpha_A^* + \sin m\alpha^* \sin m\alpha_A^*) \tag{6.9}$$

The formulation in equation (6.8) is comparable to that used for the geopotential (equation (1.39)). Therefore, it is possible to infer from it, the variations of the coefficients C_{lm} and S_{lm}:

$$V_T = \frac{\mu}{r} \sum_{l=2}^{\infty} \left(\frac{R_e}{r}\right)^l \sum_{m=0}^{l} P_{lm}(\sin\phi)(\cos m\lambda \Delta C_{lm} + \sin m\lambda \Delta S_{lm}) \tag{6.10}$$

with

$$\Delta C_{lm} = k_l * k_m * \frac{(l-m)!}{(l+m)!} \frac{M_A}{M_e} \left(\frac{R_e}{r_A}\right)^{l+1} P_{lm}(\sin\delta_A) \cos m(\alpha_A^* - \theta_G) \tag{6.11}$$

$$\Delta S_{lm} = k_l * k_m * \frac{(l-m)!}{(l+m)!} \frac{M_A}{M_e} \left(\frac{R_e}{r_A}\right)^{l+1} P_{lm}(\sin\delta_A) \sin m(\alpha_A^* - \theta_G) \tag{6.12}$$

where M_e is the Earth mass. ΔC_{lm} and ΔS_{lm} are proportional to $\left(\frac{R_e}{r_A}\right)^{l+1}$. Since $r_A >> R_e$, all the contributions characterised by $l \geq 4$ can be neglected: the most significant contributions are those associated to $l = 2$ and $l = 3$.

In the literature, it is possible to find several works, all based on the Love theory, about the analytic determination of the terrestrial tides long period effects on the orbital parameters. A semi-analytic model is already included into the Standalone version of the Draper Semi-analytical Satellite Theory (DSST) Orbit Propagator, implemented in the NASA Goddard Trajectory Determination System (GTDS) [25]. In [26], Musen and Estes propose writing the terrestrial tides potential as a function of the elliptical arguments of the Hill-Brown lunar theory, of the argument of perigee and the right ascension of the ascending node: they develop it into into trigonometric series and, finally, they exploit the Lagrangian equations to determine the orbital parameters deviations. The study carried out in this work is similar to that of Lambeck *et al.* [27], who exploit the Kaula formulation in order to express the potential and apply the Doodson theory for a better estimation of the Love number (this last will be described in Section 6.4.2).

6.4.1 Terrestrial tides effects on the orbital inclination

The formulation of the perturbing potential due to terrestrial tides in equation (6.9) is comparable to that of the perturbing potential caused by a third body (equation (6.3)). Indeed, the different contributions of the two perturbing potential are proportional:

$$V_{pl} = k_l \left(\frac{R_e}{r}\right)^{l+1} V_{A_l}$$

It is evident that, if a third body causes the generation of terrestrial tides, these lasts effects on a satellite orbit are reduced but completely comparable to the effects induced by the third body itself.

The third bodies to be considered are the Sun and the Moon. The other planets are sufficiently far from Earth to neglect their influence.

By adopting the Kaula formulation, it is possible to express each contribution of V_T in the two following ways:

$$V_{T_l} = \frac{\mu}{r}\Big(\frac{R_e}{r}\Big)^l \sum_{m,p=0}^{l} F_{lmp}(i)\Big\{ \begin{bmatrix} A_{lm} \\ -B_{lm} \end{bmatrix}_{(l-m)_{odd}}^{(l-m)_{even}} \cos\left[(l-2p)\alpha + m\Omega\right] + \begin{bmatrix} B_{lm} \\ A_{lm} \end{bmatrix}_{(l-m)_{odd}}^{(l-m)_{even}} \sin\left[(l-2p)\alpha + m\Omega\right]\Big\} \tag{6.13}$$

$$A_{lm} = k_l \frac{M_A}{M_e}\Big(\frac{R_e}{r_A}\Big)^{l+1} k_m \frac{(l-m)!}{(l+m)!} P_{lm}(\sin\delta_A)\cos m\alpha_A^* = \Delta C_{lm}\cos m\theta_G - \Delta S_{lm}\sin m\theta_G$$

$$B_{lm} = k_l \frac{M_A}{M_e}\Big(\frac{R_e}{r_A}\Big)^{l+1} k_m \frac{(l-m)!}{(l+m)!} P_{lm}(\sin\delta_A)\sin m\alpha_A^* = \Delta C_{lm}\sin m\theta_G + \Delta S_{lm}\cos m\theta_G$$

$$V_{T_l} = k_l \frac{GM_A R_e^{2l+1}}{r_A^{l+1} r^{l+1}} \sum_{m=0}^{l} k_m \frac{(l-m)!}{(l+m)!} \sum_{p=0}^{l}\sum_{h=0}^{l} F_{lmp}(i)F_{lmh}(i_A)\cos\left[(l-2p)\alpha - (l-2h)\alpha_A + m(\Omega-\Omega_A)\right] \tag{6.14}$$

The first expression (6.13) can be exploited to determine the long period inclination drift. The variation of the inclination in time is proportional to $\frac{\partial V_{T_l}}{\partial \Omega}$ and to $\frac{\partial V_{T_l}}{\partial \omega}$ (see the Lagrangian equation (1.35)). In order to get the long period variation, it is possible to exploit the same strategy adopted by Lami *et al.* in [21]: integrating the inclination drift over an orbital period assuming all the orbital parameters constants except for the true anomaly. This is motivated by the fact that in practice the orbits won't be allowed to vary too much. Also the position of the third body can be considered constant since its apparent angular motion n_A is smaller than that of the satellite: $n_A << n$. Applying the Lagrangian equation (1.35), the inclination drift can be expressed as:

$$\frac{di}{dt} = \frac{1}{na^2\sqrt{1-e^2}\sin i}\frac{\partial V_{T_l}}{\partial \Omega} + \frac{\cot i}{na^2\sqrt{1-e^2}}\frac{\partial V_{T_l}}{\partial \omega}$$

$$\frac{\partial V_{T_l}}{\partial \Omega} = \frac{\mu R_e^l}{r^{l+1}} \sum_{m=0}^{l}\sum_{p=0}^{l} F_{lmp}(i) m\Big\{ \begin{bmatrix} -A_{lm} \\ B_{lm} \end{bmatrix}_{(l-m)_{odd}}^{(l-m)_{even}} \sin\left[(l-2p)\alpha + m\Omega\right] + \begin{bmatrix} B_{lm} \\ A_{lm} \end{bmatrix}_{(l-m)_{odd}}^{(l-m)_{even}} \cos\left[(l-2p)\alpha + m\Omega\right]\Big\}$$

$$\frac{\partial V_{T_l}}{\partial \omega} = \frac{\mu R_e^l}{r^{l+1}} \sum_{m=0}^{l}\sum_{p=0}^{l} F_{lmp}(i)(l-2p)\Big\{ \begin{bmatrix} -A_{lm} \\ B_{lm} \end{bmatrix}_{(l-m)_{odd}}^{(l-m)_{even}} \sin\left[(l-2p)\alpha + m\Omega\right] + \begin{bmatrix} B_{lm} \\ A_{lm} \end{bmatrix}_{(l-m)_{odd}}^{(l-m)_{even}} \cos\left[(l-2p)\alpha + m\Omega\right]\Big\}$$

In view of the following equations,

- $\int_0^{T_0} \frac{di}{dt}dt = \int_0^{2\pi} \frac{di}{dt}\frac{1}{n}\frac{(1-e^2)^{3/2}}{(1+e\cos\nu)^2}d\nu$, having assumed constant the eccentricity
- $\sin\left[(l-2p)\alpha + m\Omega\right] = \sin\left((l-2pi)\nu\right)\cos\left[(l-2p)\omega + m\Omega\right] + \cos\left((l-2pi)\nu\right)\sin\left[(l-2p)\omega + m\Omega\right]$
- $\cos\left[(l-2p)\alpha + m\Omega\right] = \cos\left((l-2pi)\nu\right)\cos\left[(l-2p)\omega + m\Omega\right] - \sin\left((l-2pi)\nu\right)\sin\left[(l-2p)\omega + m\Omega\right]$
- $r^{l+1} = \left(\frac{a(1-e^2)}{1+e\cos\nu}\right)^{l+1}$

the computation of the integral over an orbital period of the inclination drift implies the integration the two following terms:

$$\cos\left(l-2pi)\nu\right)(1+e\cos\nu)^{l-1}$$

$$\sin\left(l-2pi)\nu\right)(1+e\cos\nu)^{l-1}$$

where $l-1 \geq 0$. For the binomial theorem, we have:

$$(1+e\cos\nu)^{l-1} = \sum_{k=0}^{l-1} \begin{pmatrix} l-1 \\ k \end{pmatrix} (e\cos\nu)^k$$

Since the orbit is quasi-circula, it is sufficient to consider the terms up to $k=2$:

$$(1+e\cos\nu)^{l-1} \sim 1 + \frac{(l-1)!}{(l-2)!}e\cos\nu + \frac{(l-1)!}{2!(l-3)!}e^2\cos^2\nu + o(e^3)$$

By substituting this expression in the integral, it can be easily found that $\forall(l-2p) \neq 0$:

$$\int_0^{2\pi} \cos(l-2p)(1 + \frac{(l-1)!}{(l-2)!}e\cos\nu + \frac{(l-1)!}{2!(l-3)!}e^2\cos^2\nu) = 0$$

$$\int_0^{2\pi} \sin(l-2p)(1 + \frac{(l-1)!}{(l-2)!}e\cos\nu + \frac{(l-1)!}{2!(l-3)!}e^2\cos^2\nu) = 0$$

since $l-2p$ is an integer number. Thus, it can be deduced that the long period variations of the inclination are associated to the potential contributions characterised by $p = l/2$ and that they depend only on $\frac{\partial V_{T_l}}{\partial \Omega}$. In particular, since p is an integer number and all the terms with $l >= 4$ are negligible, the contributions to consider are those associated to $l=2$, $p=1$ and $m \neq 0$. At this point the integral of the inclination drift is reduced to :

$$\int_0^{2\pi} C(1+e\cos\nu)d\nu = 2\pi C$$

$$C = \frac{1}{na^2\sqrt{1-e^2}\sin i}\frac{(1-e^2)^{3/2}}{n(1-e^2)^3}\frac{\mu R_e^2}{a^3}\sum_{m=1}^{2} F_{2m1}(i)m\Big\{ \begin{bmatrix} -A_{2m} \\ B_{2m} \end{bmatrix}_{(2-m)_{odd}}^{(2-m)_{even}} \sin m\Omega + \begin{bmatrix} B_{2m} \\ A_{2m} \end{bmatrix}_{(2-m)_{odd}}^{(2-m)_{even}} \cos m\Omega \Big\}$$

To get the long period inclination drift is sufficient to divide for the orbital period $T_0 = \frac{2\pi}{n}$. Thus, the long period inclination drift is :

$$\frac{di}{dt} = \frac{(1-e^2)}{na^2\sin i}\Big(\frac{\partial V_{T_{211}}}{\partial\Omega} + \frac{\partial V_{T_{221}}}{\partial\Omega}\Big) \tag{6.15}$$

$$\frac{\partial V_{T_{211}}}{\partial\Omega} = -\frac{3}{2}\frac{1}{(1-e^2)^3}\frac{\mu R_e^2}{a^3}\sin i\cos i(A_{21}\cos\Omega + B_{21}\sin\Omega)$$

$$\frac{\partial V_{T_{221}}}{\partial\Omega} = 3\frac{1}{(1-e^2)^3}\frac{\mu R_e^2}{a^3}\sin^2 i(B_{22}\cos 2\Omega - A_{22}\sin 2\Omega)$$

From the second formulation of the potential in equation (6.14), it can be deduced that, if the third body is the Sun and the orbit is sun-synchronous, the perturbing potential causes a secular inclination drift. Indeed, if $l-2h = m = 2$, the constant quantity $\Omega - \alpha_A$ appears. The drift is proportional to those induced by the Sun, discussed in the previous section 6.3. With the assumption of quasi circular orbit, it is associated to the potential contribution characterised by $l=2$, $m=2$, $p=1$ and $h=0$ and it can be approximated as:

$$\frac{di}{dt} = k_2\frac{3\pi}{2}\Big(\frac{R_e}{r}\Big)^5\frac{T_0}{T_{SO}^2}\sin i\cos^4\Big(\frac{i_{SO}}{2}\Big)\sin\Big(4\pi\Big(\frac{H}{T_E} - \frac{1}{2}\Big)\Big) \tag{6.16}$$

6.4.2 Love numbers

The Love's theory assumes that the Earth geopotential variation is proportional to the terrestrial tides. In 1980, John Wahr deepened the Love model showing that the Love numbers k_l depend on the excitation frequency [28]. Let the focus be on the coefficients ΔC_{20}, ΔC_{21}, ΔS_{21}, ΔC_{22} and ΔS_{22}. As the perturbing third bodies are the Moon and the Sun and their motion is very slow in comparison to the Earth rotation, it's possible to assume that their declination is constant and that their longitude has a one-day-long period. Thus, ΔC_{20} has long period variations, ΔC_{21} and ΔS_{21} have diurnal variations and ΔC_{22} and ΔS_{22} have semi-diurnal variations. However, to have a precise estimation of the terrestrial tides effects, it is not possible to neglect the third body motion with respect to the Earth. This motion has its own periods; when combined with the Earth rotation, for each ΔC_{lm} and ΔS_{lm} it generates a spectrum always centered at m cycles per day, but characterised also by other frequencies. Therefore, it can be affirmed that each ΔC_{lm} and ΔS_{lm} is given by a superposition of tidal waves. The analytic representation of these waves depend on the theory adopted about the Sun and the Moon motion. Usually that of Doodson, developed in 1921, is exploited. Doodson has shown that the coefficients ΔC_{lm} and ΔS_{lm} can be determined as:

$$R_e \Delta C_{lm} = N_{lm} \sum_s H_s \left[\begin{array}{c} \cos\theta_S \\ \sin\theta_s \end{array} \right]_{(m+l)_{odd}}^{(m+l)_{even}}$$

$$R_e \Delta S_{lm} = N_{lm} \sum_s H_s \left[\begin{array}{c} -\sin\theta_S \\ \cos\theta_s \end{array} \right]_{(m+l)_{odd}}^{(m+l)_{even}}$$

where

- $N_{lm} = (-1)^m \sqrt{\frac{2l+1}{4\pi} \frac{(l-m)!}{(l+m)!}}$
- H_s is the amplitude of the wave s
- θ_s is the astronomic argument of the wave s. It is the linear combination of the six Doodson fundamental arguments:

$$\theta_S = n_1\tau + n_2 S + n_3 h + n_4 P + n_5 N + n_6 p_S$$

  - τ is the Moon hour angle shifted by 180°
  - S is the Moon tropic longitude
  - h is the Sun mean tropic longitude
  - P is the Moon perigee mean tropic longitude
  - N is the opposite of the Moon node tropic longitude
  - p_S is the Sun perigee mean tropic longitude

Each Doodson wave is identified by a number defined by means of the six integers n_i, $i = 1...6$:

$$\nu(s) = 100n_1 + 10(n_2 + 5) + (n_3 + 5) + \frac{n_4 + 5}{10} + \frac{n_5 + 5}{100} + \frac{n_6 + 5}{1000}$$

For example the wave 255.555 correspond to the integers $(2; 0; 0; 0; 0; 0)$.

On the basis of the Doodson theory, Wahr has computed the Love numbers. Wahr has assumed the model of an elastic, elliptic and ocean-less Earth. He found out that there exist resonance phenomena between the excitation tides and the rotation of the Earth core, causing different crust responses. Thus, he determined the values of the Love numbers to consider for each tidal wave, in order to evaluate ΔC_{lm} and ΔS_{lm}, with $l = 2, 3$. These values have been recomputed in 1991 by Zhu, who had a better estimation of the terrestrial core nutation period available. He discovered that the important corrections to perform concern the Love number k_2. In particular, it is possible to consider one only constant value for the long period and the semi-diurnal waves: $k_2 = 0.299$ for ΔC_{20} and $k_2 = 0.302$ for ΔC_{22} and ΔS_{22}. For the diurnal waves the situation is more complex because the tidal waves impose

important variations. In this case, the usually adopted procedure is to compute a first approximated value of ΔC_{21} and ΔS_{21} considering a Love number equal to $k_2 = 0.3$ and then to correct it in the following way :

$$R_e \Delta C_{lm} = N_{lm} \sum_s H_s \Delta k_s \left[\begin{array}{c} \cos\theta_S \\ \sin\theta_s \end{array} \right]_{(m+l)_{odd}}^{(m+l)_{even}}$$

$$R_e \Delta S_{lm} = N_{lm} \sum_s H_s \Delta k_s \left[\begin{array}{c} -\sin\theta_S \\ \cos\theta_s \end{array} \right]_{(m+l)_{odd}}^{(m+l)_{even}}$$

where Δk_s is the difference between the Love number associated to the wave s and the previously exploited approximated one. To an higher precision this procedure could be adopted for each ΔC_{2m} and ΔS_{2m}; practically, it is sufficient to correct ΔC_{21} and ΔS_{21} considering a limited number of Doodson waves, shown in Table 6.1.

Table 6.1: Love number corrections to adopt to estimate the coefficients ΔC_{21} and ΔS_{21}

Doodson number	Δk_s
145.555	-0.0016
163.555	-0.0098
165.545	-0.0299
165.555	-0.0317
165.565	-0.0338
166.554	0.1665

For the long period inclination drift model (equation (6.15)), the adopted Love numbers and ΔC_{21} and ΔS_{21} corrections are those of the IERS 2003 standard, used in the CNES Patrius library. For the secular inclination drift (equation (6.4.1)), the Zhu estimated Love number $k_2 = 0.302$ is exploited.

6.4.3 Inclination drift model evaluation

In order to verify the accuracy of the analytical long period inclination drift model, the estimated drift value is compared to the drift obtained by simulation. In the simulations, the orbit evolution is determined by numerical propagation, exploiting the terrestrial tides model included in the *Patrius library*. The analytically estimated drift is updated only after a period equal to the predictable horizon increased by an orbital period. Indeed, AOC exploits the drift value computed at the ascending node to evaluate the eventual out-of-plane manoeuvres. The missions taken into account for the error evaluation are mission D1 and mission B2. The results obtained for mission B2, being it characterised by a dawn orbit, can be significant also for the missions not characterised by sun-synchronous orbits. By exploiting the value of the drift updated at each ascending node, the mean relative committed error is 0.0093% for mission D1 and 0.13% for mission B2 (Figures 6.29, 6.31). The error is higher for mission B2 because the changes in the Δi trends are less smooth and small medium period variations appear. The obtained results are really positive and show that the model is accurate. This is also confirmed by the simulations executed by considering the other missions (see Figures 6.32a - 6.32d). In the all the figures, the red line represents the simulated Δi trend induced by the terrestrial tides (considering only the orbital ascending nodes), while the blue line represents the trend estimated by means of the analytically determined drift.

Mission D1 has also be exploited to verify the secular drift model. The trend of the real Δi shows a drift equal to almost $-2.18\dot{1}0^{-7}$ mdeg/s, while the analytic value computed at the beginning of the simulation is $-2.1438\dot{1}0^{-7}$ mdeg/s: the approximated relative error is 1.74%.

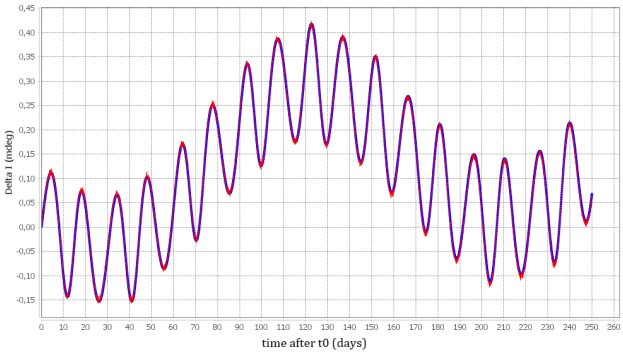

Fig. 6.28: Mission B2 - Free evolution of Δi under the effects of terrestrial tides compared with the trend estimated by exploiting the inclination drift computed analytically and updated at each ascending node

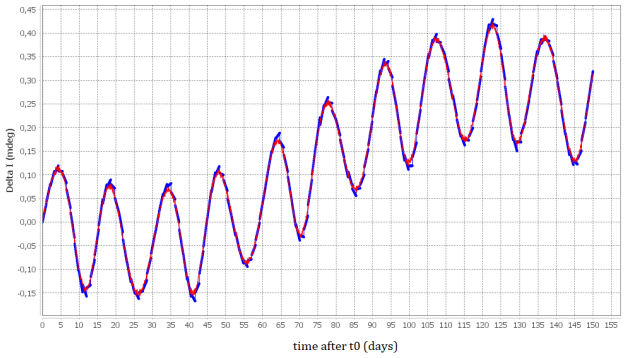

Fig. 6.29: Mission B2 - Free evolution of Δi under the effects of terrestrial tides compared with the trend estimated by exploiting the inclination drift computed analytically and updated after a period equal to the predictable horizon increased by one orbital period

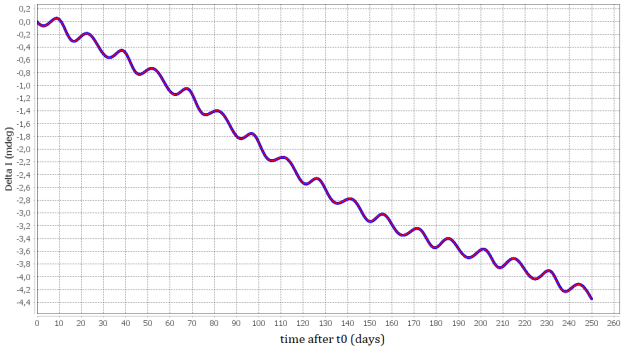

Fig. 6.30: Mission D1 - Free evolution of Δi under the effects of terrestrial tides compared with the trend estimated by exploiting the inclination drift computed analytically and updated at each ascending node

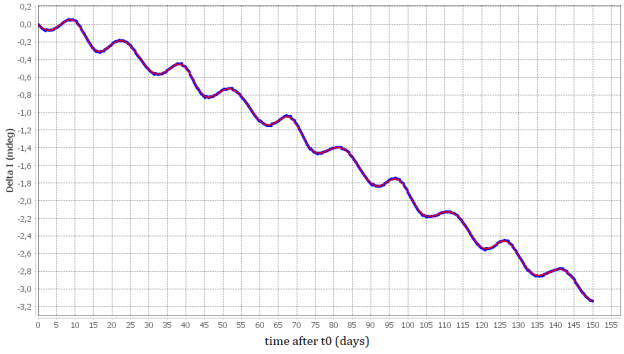

Fig. 6.31: Mission D1 - Free evolution of Δi under the effects of terrestrial tides compared with the trend estimated by exploiting the inclination drift computed analytically and updated after a period equal to the predictable horizon increased by one orbital period

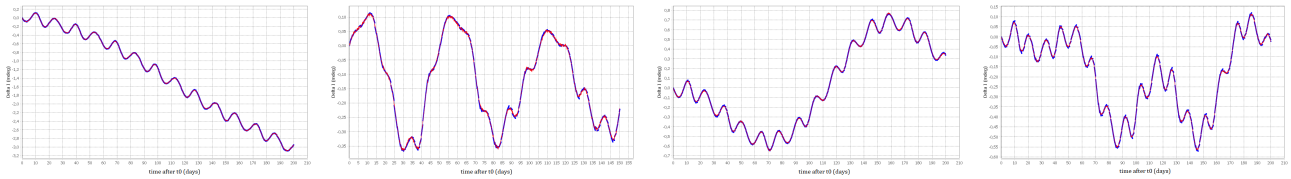

(a) Mission A2 *(b)* Mission C *(c)* Mission E *(d)* Mission F

Fig. 6.32: Free evolution of Δi under the effects of terrestrial tides compared with the trend estimated by exploiting the inclination drift computed analytically and updated after a period equal to the predictable horizon increased by one orbital period

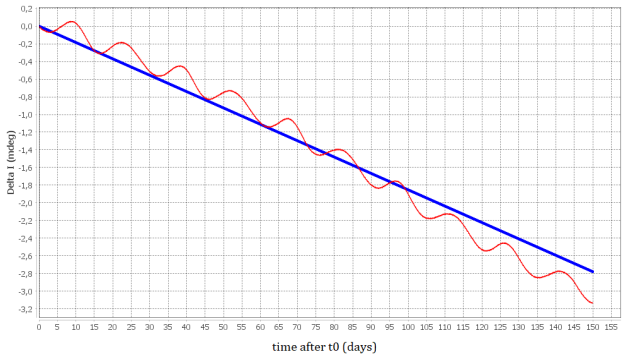

Fig. 6.33: Mission D1 - Free evolution of Δi under the effects of terrestrial tides compared with the trend estimated by exploiting the secular inclination drift computed analytically

The results are satisfying: both the analytic models to compute the long period and the secular inclination drifts are acceptable and sufficiently accurate.

6.5 Atmospheric drag

The atmospheric drag is one of the perturbations with the greatest influence on near-Earth satellites. The perturbing acceleration, that it causes, can be modeled as follow:

$$\mathbf{a}_{p_{drag}} = \frac{1}{2}\frac{C_D A}{m}\rho v_r \mathbf{v_r} \tag{6.17}$$

where:

- C_D is the drag coefficient
- A is the effective cross-section area of the satellite
- m is the satellite mass
- ρ is the atmospheric drag
- v_r is the satellite speed relative to the local atmosphere

The relative speed depends on the atmosphere rotation ω_{drag} speed:

$$\mathbf{v_r} = \mathbf{v} - \omega_{drag} \times \mathbf{r}$$

Its relative velocity component, imposed by the atmospheric angular velocity, causes the inclination drift: it generates an acceleration component that is normal with respect to the orbital plane [29]:

$$a_{p_{drag_N}} = -\frac{\rho v \epsilon}{2\sqrt{Q}} r\omega_{drag} \sin i \cos\alpha \tag{6.18}$$

with $\epsilon = \frac{QAC_D}{m}$, $Q = \left(1 - \frac{r_p \omega_{drag}\cos i}{v_p}\right)^2$, r_p the satellite perigee distance and v_p the satellite perigee velocity. Applying equation (1.26), the inclination drift can be expressed as:

$$\frac{di}{dt} = \frac{r\cos\alpha}{na^2\sqrt{1-e^2}\sin i} a_{p_{drag_N}} \tag{6.19}$$

By means of this equations, it would be possible to get the long period drift of the inclination. However, this evaluation is complicated. Indeed, even though a large literature exists on the atmospheric drag, this is still one of the most difficult perturbations to evaluate. The reason is that it depends on parameters, whose evolution is difficult to predict. The precision of the acceleration evaluation depends on the precision of the exploited atmosphere model since the parameters C_D, ρ and

V_r depend on it. In particular, the correct computation of the density is complex: this parameter varies exponentially with the altitude, but it depends also on the solar hour, on the year epoch, on the latitude, on the solar activity and on the geomagnetic activity. Very complex models which take into account these factors have been developed. However, they cannot be exploited by AOC to compute the inclination drift: indeed, there is no possibility to predict the solar activity and the geomagnetic activity in a sufficiently accurate way. Consequently, another strategy has to be adopted.

King-Hele has developed formulas that can be used to compute the long period variation of the inclination and of the other orbital parameters in a semi-analytic way for quasi circular orbits ($e < 0.2$). He assumes that the atmospheric rotation velocity is proportional to the Earth rotation rate:

$$\omega_{drag} = \zeta \omega_e$$

Moreover, he adopts a very simple model for the density:

$$\rho = \rho_p e^{-\frac{r-r_p}{H_{scale}}} \tag{6.20}$$

where ρ_p is the value of the density at the orbital perigee and H_{scale} is an altitude scale. As in [21], he considers all the orbital elements constant during one orbital period except for the true anomaly. After having integrated over an orbital period, the inclination variation which he computes is expressed as [19]:

$$\Delta i = -\frac{\pi a \zeta \omega_e \epsilon \rho_p}{2n\sqrt{Q}} e^{-c} \sin i [I_0(c) - 2eI_1(c) + (I_2(c) - 2eI_1(c)) \cos 2\omega] \tag{6.21}$$

where:

- $c = \frac{ae}{H_{scale}}$
- $I_s(c)$ is the modified Bessel function [30]:

$$I_s(c) = \frac{1}{2\pi} \int_0^{2\pi} \cos(sx) e^{c \cos x} dx$$

Dividing it for the orbital period, it is possible to obtain the long period inclination drift. The problem of this formulation is linked with the correct computation of ρ_p. However, there is a way to solve it. Indeed, it is possible to express the inclination drift as a function of the semi-major axis drift, considering that the only long variation of this orbital parameter is due to the acceleration drag (see Table 1.1) [29]. The semi-major axis long period variation is given by [19]:

$$\Delta a = -2\pi \epsilon a^2 \rho_p e^{-c} [I_0(c) + 2eI_1] \tag{6.22}$$

Thus, we have:

$$\Delta i = C \Delta a \tag{6.23}$$

$$C = \frac{1}{4} \frac{\zeta \omega_e \sin i}{an\sqrt{Q}} \frac{I_0(c) - 2eI_1(c) + (I_2(c) - 2eI_1(c)) \cos 2\omega}{I_0(c) + 2eI_1}$$

As a consequence, it is possible to write:

$$\frac{di}{dt} = C \frac{da}{dt} \tag{6.24}$$

In this way, there is no a direct dependence of this formulation on the density. The values of the altitude scale H_{scale} are furnished by Blitzer [19]. The semi-major axis drift can be computed approximately by exploiting the values of the Δa at the orbital ascending nodes. By measuring Δa_j at a current ascending node j and having the measure of Δa_{j-1} at the previous ascending node, $\frac{da}{dt}$ can be estimated as:

$$\frac{da}{dt} \sim \frac{\Delta a_j - \Delta a_{j-1}}{T_0}$$

This strategy is not optimal. Indeed, the inclination drift, estimated by applying equation (6.24), includes the medium period, the long period and the secular contributions. It is no possible to isolate the secular component or at least exclude the medium period one. In order to do that, the measures done at a large number of ascending nodes should be exploited, which can be very expensive in terms of computational time. If a lot of nodes are exploited, it would be necessary to take into account the temporal variation of the coefficient C in equation (6.24): then, the long period drift would have to be estimated as the mean of the values computed at the different nodes:

$$\frac{di}{dt}_{mean} = \frac{1}{n}\sum_{n} C_n \frac{da}{dt}_{n}$$

On the contrary, a shorter time interval allows to consider the coefficient constant, since the orbital parameters variation in time is slow. Thus, it would be simply necessary to estimate an average semi-major axis drift to determine an estimation of the long period inclination drift:

$$\frac{di}{dt}_{mean} = C\frac{1}{n}\sum_{n} \frac{da}{dt}_{n}$$

In any case, the secular inclination drift cannot be determined and only an approximated value of the long period drift can be found. It has to be verified that, assuming this last constant for a time equal to the predictable horizon increased by one orbital period, the error is acceptable.

Several simulations are carried out to verify the validity of the strategy. MATLAB has been used to compute the error. Missions B2 and D1 are taken into account. The simulations measures are used to determine the average long period approximated trend of the inclination variation. This is used to compute the local average real drift at the different times. The trend curve is determined by means of the MATLAB moving-average filter (see Appendix A) (Figures 6.35-6.34).

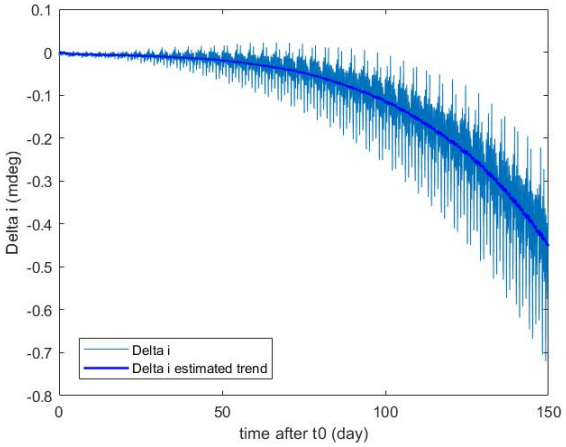

Fig. 6.34: Mission D1 - real free evolution of Δi and estimated trend under the effects of the atmospheric drag

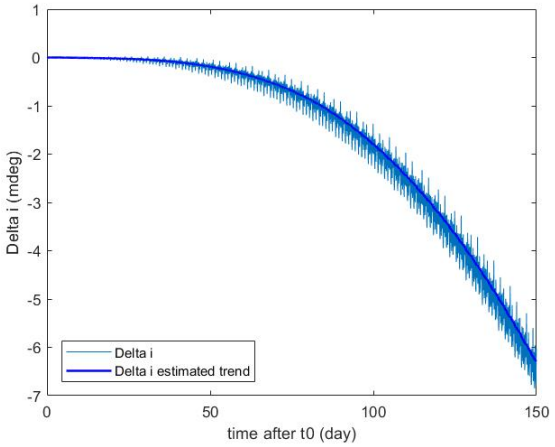

Fig. 6.35: Mission B2 - real free evolution of Δi and estimated trend under the effects of the atmospheric drag

The average real values of the long period drift obtained are compared to those computed using the model in (6.24), considering the coefficient C constant. The measures at four, eight and sixteen previous ascending nodes are used to approximate the semi-major axis drift. The average absolute and relative errors are reported in Table 6.2 for mission B2 and in Table 6.3 for mission D1. The results are shown in Figures 6.36 and 6.37. The error is significant, which is due to two main reasons. First of all, the inclination drift formulation in equation (6.24) is based on a simplified model of the atmosphere, while that exploited for the numerical propagation is more complex and accurate, since it takes into account the solar and geomagnetic activity. Moreover, the outcomes confirm that the one of the main issues of the strategy is linked to the medium period variations that cannot be filtered. It can be observed that higher variations imply an higher error. Indeed, in mission B2 the error is

lower because the medium period variations are reduced with respect to mission D1. Furthermore, at the increase of the number of nodes exploited, the mean absolute error decreases. However, both the average absolute error and the average relative error are still significant exploiting sixteen nodes.

Table 6.2: Mission B2 - average error of the inclination drift estimated as in equation (6.24)

	Average absolute error [mdeg/s]	Average relative error
measures at 4 nodes	$1.18 \cdot 10{-}6$	290.73%
measures at 8 nodes	$5.76 \cdot 10^{-7}$	139.67%
measures at 16 nodes	$1.28 \cdot 10^{-7}$	37.8%

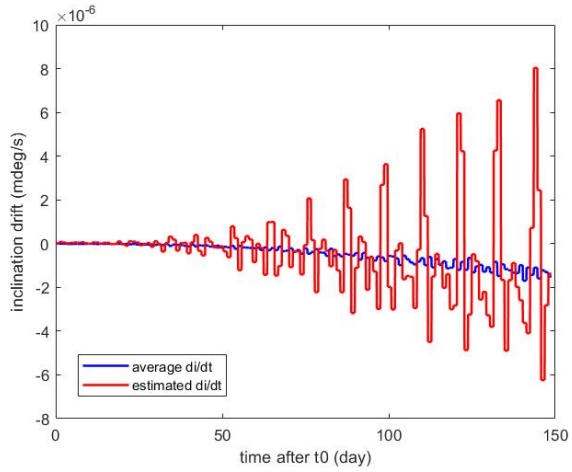

(a) $n = 4$

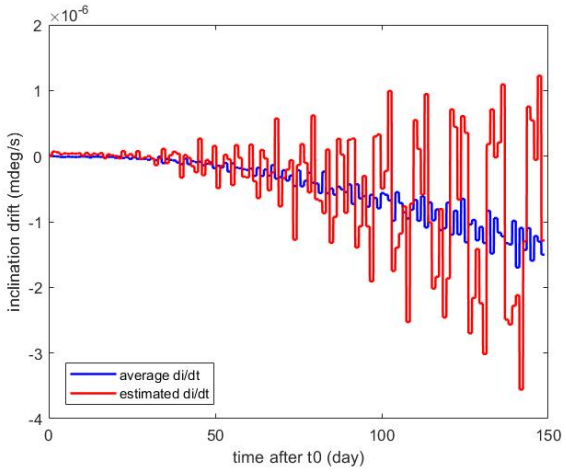

(b) $n = 8$

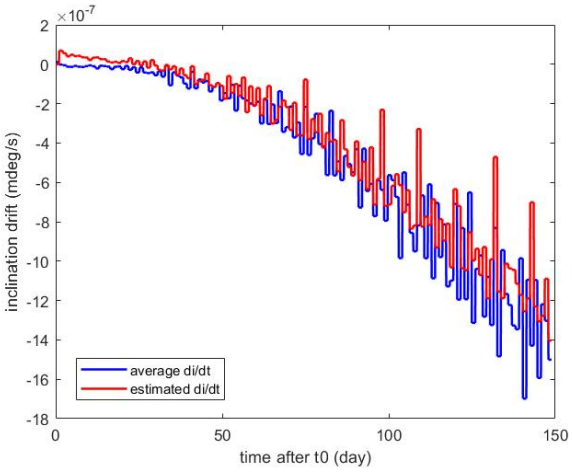

(c) $n = 16$

Fig. 6.36: Mission B2 - Average real long period inclination drift under the effects of the atmospheric drag (blue) compared with drift computed semi-analytically and updated after a time equal to the predictable horizon increased by one orbital period (red). The measures at n previous node are used to estimate the drift.

Table 6.3: Mission D1 - average error of the inclination drift estimated as in equation (6.24)

	Average absolute error [mdeg/s]	Average relative error
measures at 4 nodes	$1.89 \cdot 10{-}7$	1463.1%
measures at 8 nodes	$3.8 \cdot 10^{-7}$	157%
measures at 16 nodes	$2.88 \cdot 10^{-8}$	385%

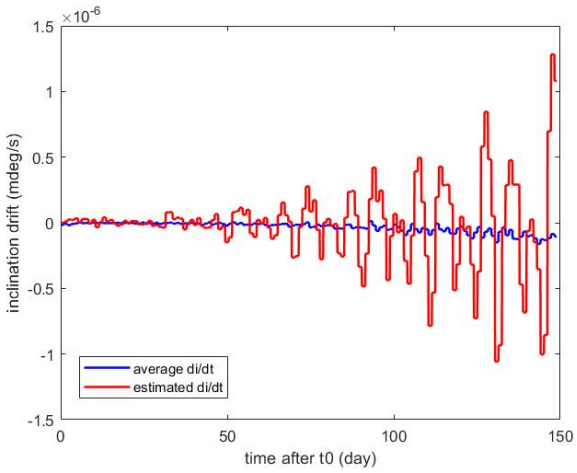

(a) $n = 4$

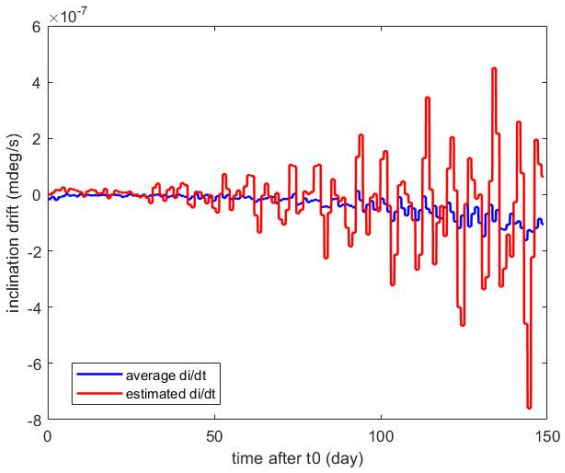

(b) $n = 8$

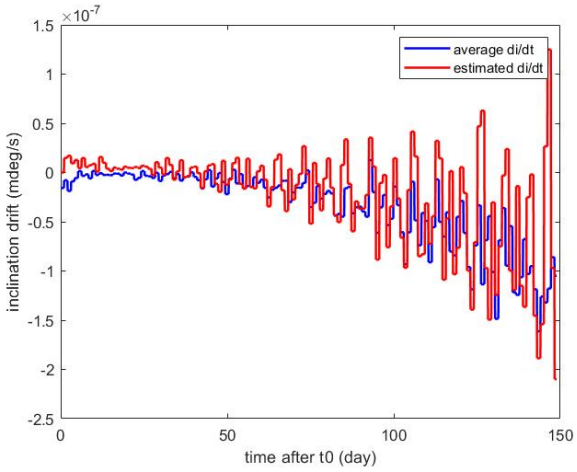

(c) $n = 16$

Fig. 6.37: Mission D1 - Average real long period inclination drift under the effects of the atmospheric drag (lue) compared with drift computed semi-analytically and updated after a time equal to the predictable horizon increased by one orbital period (red). The measures at n previous node used to estimate the drift

The same simulations have been re-executed taking into account the temporal variation of the coefficient C in equation (6.24). For mission B2, the results don't change. For mission D1, if sixteen nodes are used, the error decreases: the mean absolute error becomes $2.62 \cdot 10^{-7}$ mdeg/s, the mean relative error becomes 349%. Thus, if more than sixteen nodes are used, which could be done in order to obtain an higher accuracy, it will probably be necessary to take into account the temporal variation of C.

An alternative strategy can be exploited to determine the inclination drift due to the atmospheric drag. It coincides with the same method already implemented in AOC: to estimate the average long period drift by exploiting the measures of the Δi values at the ascending nodes. At each node, the total inclination drift over one orbital period is determined: by subtracting from it the long period contributions due to the other orbital perturbations (the moon attraction, the sun attraction and the terrestrial tides), the drift caused by the atmospheric drag is approximated. Then, the determined values are used to get the mean. This strategy has the same problematic of the previous one presented: the inclination drift estimation is subjected to the medium period variations. The only way to filter them is to consider the measures at a large number of nodes, which has an impact on the computational time. Indeed, at each node the long period contributions, due to the solar and lunar potentials and the

terrestrial tides, would have to be computed. Even with this strategy, it is not possible to determine the secular contribution, but only the approximated long period drift.

To evaluate the two strategies and comparing them, simulations involving all the orbital perturbations have to be performed. This problem is discussed in the following section.

6.6 Inclination drift approximation: results

The three main perturbations that have to be considered in order to determine the secular or long period inclination drift are: the solar potential, the terrestrial tides caused by the Sun gravitational attraction and the drag. This last perturbation influence depends on the orbital altitude. The missions of interest for AOC involve very low orbits; so, the drag influence cannot usually be neglected. This perturbation is the most complex to handle. In the previous section, two strategies have been introduced. None of them is satisfying, because none of them allows to filter the inclination drift from the medium period variations. In order to determine which strategy produces the smallest error, several simulations are carried out. Missions D1 and B2 are exploited. The estimated inclination drift is considered constant for a time equal to the predictable horizon increased by one orbital period, after which it is updated. It is compared with an average real local drift evaluated on the basis of the long period Δi trend. This last one is determined as described in the previous section, for mission B2. For mission D1, a simple least square fitting, based on a first order polynomial, has been used, since the trend is linear. In the following, the strategy associated to equation (6.24) will be indicated as method 1; the other strategy will be indicated as method 2. For both the methods, the estimated drift is computed by considering the measures at sixteen previous ascending nodes.

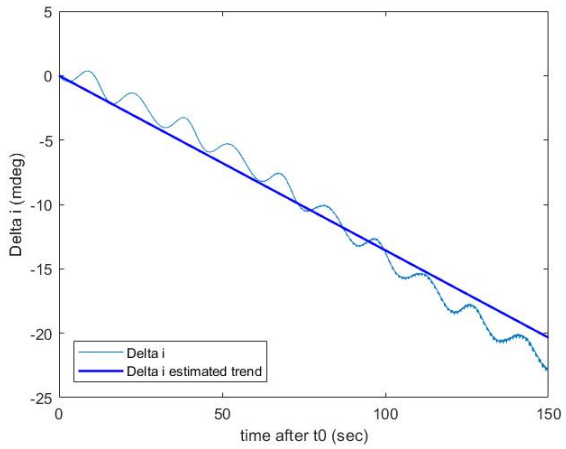

Fig. 6.38: Mission D1 - real free evolution of Δi and estimated trend

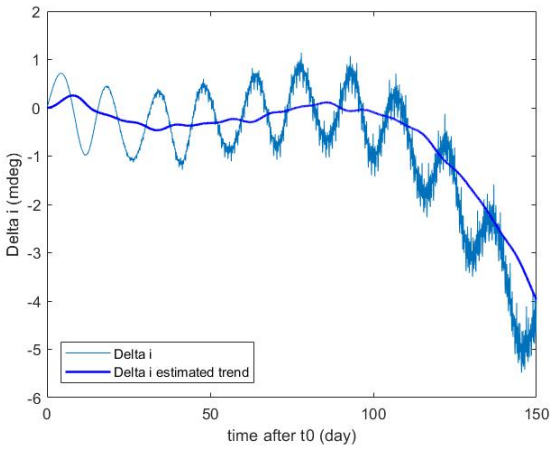

Fig. 6.39: Mission B2 - real free evolution of Δi and estimated trend

The results for mission B2 are shown in Table 6.4 and in Figure 6.40. Those of mission D1 are shown in Table 6.5 and in Figures 6.41 and 6.42. For mission D1, the solar gravitational attraction and the terrestrial tides contributions are computed by means of both the long period model and the secular model.

Table 6.4: Mission B2 - average absolute and relative errors of the inclination drift estimation, executed considering the measures at sixteen ascending nodes

average error	method 1	method 2	drag neglected
absolute [mdeg/s]	$2.89 \cdot 10^{-7}$	$1.11 \cdot 10^{-6}$	$3.69 \cdot 10^{-7}$
relative	159.7%	630.55%	110.35%

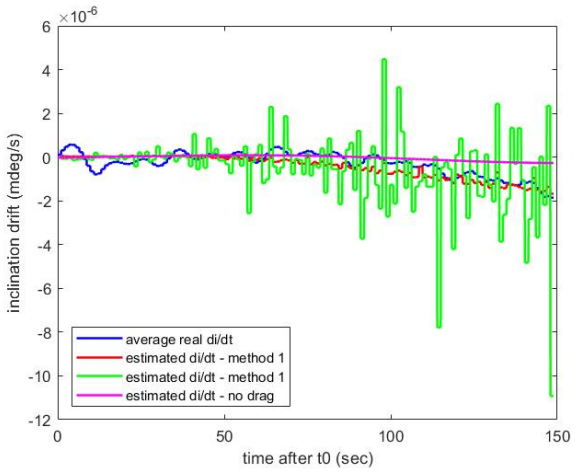

Fig. 6.40: Mission B2 - inclination drift estimated exploiting the measures at sixteen previous node

Table 6.5: Mission D1 - average absolute and relative errors of the inclination drift estimation, executed considering the measures at sixteen ascending nodes

solar potential and terrestrial tides contribution	average error	method 1	method 2	drag neglected
long period	absolute [mdeg/s]	$6.52 \cdot 10^{-8}$	$3.67 \cdot 10^{-7}$	$6.42 \cdot 10^{-7}$
	relative	4.16%	23.39%	4.09%
secular	absolute [mdeg/s]	$5.3 \cdot 10^{-8}$	$3.59 \cdot 10^{-7}$	$7.95 \cdot 10^{-8}$
	relative	3.38%	22.87%	5.064%

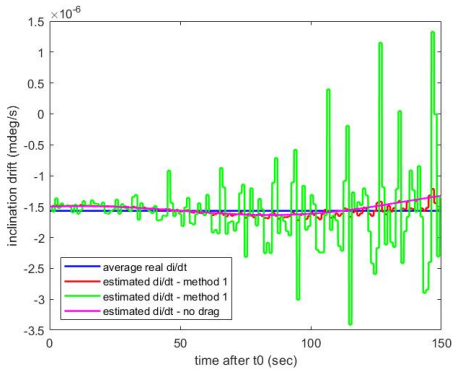

Fig. 6.41: Mission D1 - inclination drift estimated considering the long period drift models associated to the solar potential and the terrestrial tides and exploiting the measures at sixteen previous node

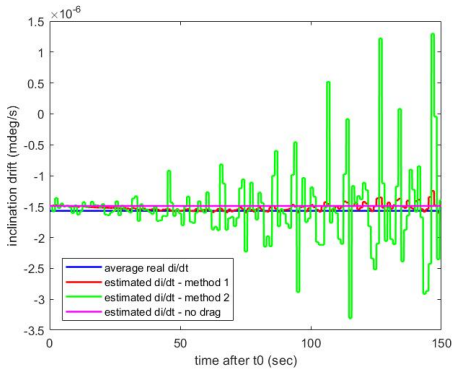

Fig. 6.42: Mission D1 - inclination drift estimated considering the secular drift models associated to the solar potential and the terrestrial tides and exploiting the measures at sixteen previous node

It is possible to observe that, the secular drift model is accurate as much as the long period one: so it could be exploited for certain kind of missions. Moreover, it is evident that neglecting the drag can not be an option: for mission D1 it could be acceptable, but not for mission B2, whose orbit is already too low. From both the missions outcomes, it results that the most accurate method to include the drag effects results to be method 1. Indeed, for the same number of nodes exploited to get the necessary measures, method 1 gives better estimations of the long period inclination drift than method 2. This is completely justifiable considering that, in method 2, the drift estimation is affected by the medium period variations due to other perturbations, mainly the solar radiation pressure, in addiction to the

atmospheric drag. To improve the accuracy, these medium period contributions should be modeled; but, this is really complex since, as the atmospheric drag, also the solar radiation pressure effects vary with the unpredictable solar activity. Moreover, method 2 is based on several analytic models: even though these are accurate, the errors associated to them accumulate. Thus, with the objective of exploiting a limited number of nodes, method 1 results to be more promising. However, its issues concerning the model, discussed in the previous section, should be solved to increase its accuracy. Indeed, it produces an important error, especially if the drag is the perturbation causing the main contribution of the long period inclination variation, as in the case of mission B2; for mission D1, the error is inferior only because the atmospheric drag has a significantly reduced effect in comparison to the solar potential. It is expected that, increasing the number of nodes used to estimate the inclination drift, the accuracy will increase for both the methods. However, for method 1, very likely, this would imply to take into account the temporal variation of the coefficient C in equation (6.24).

The large error obtained for mission B2 can be caused also by another factor, which is not linked to the atmospheric drag. The lunar potential effects have not been considered to estimate the drift. Indeed, it causes inclination variations characterised by frequencies which are superior than those induced by the other perturbations. However, there are contributions whose period is sufficiently high to have potentially an impact.

6.7 Lunar potential contribution

The inclination variations due to the lunar potential have different characteristic periods: indeed the inclination trend can be decomposed into several harmonics. Their period is usually lower than that of other perturbations such that the lunar potential can sometimes be neglected in first approximation. In particular, this is the case of low, non-dawn/dusk, sun-synchronous orbits, for which the secular contributions of the Sun, the solar terrestrial tides and the atmospheric drag generate the main drift contributions. However, for all the other kinds of orbits, there are some harmonics whose period is sufficiently long to have an impact and to be taken into account. A study to determine the lunar potential longer period contributions to the drift is carried out: it is based on the work of Kaula [23], [13].

In Section 6.3, the Kaula formulation to express a third body potential has been introduced in equation (6.6). This last one is exploited in order to determine the lunar potential drift contributions with the longest periods. Considering that $r << r_A$, the main components are those associated to $l = 2$. The inclination variation is proportional to $\frac{\partial V_M}{\partial \Omega}$ and to $\frac{\partial V_M}{\partial \omega}$. Indeed, applying equation (1.35), the drift results to be:

$$\frac{di}{dt} = \frac{1}{na^2\sqrt{1-e^2}\sin i}\frac{\partial V_M}{\partial \Omega} + \frac{\cot i}{na^2\sqrt{1-e^2}}\frac{\partial V_M}{\partial \omega}$$

$$\frac{\partial V_M}{\partial \Omega} = -\frac{GM_M r^2}{r_M^3}\sum_{m=0}^{2}\sum_{p=0}^{l} k_m \frac{(2-m)!}{82+m)!} m F_{2mp} F_{2mh}(i) \sin\left(2-2p)\alpha - (2-2h)\alpha_M + m(\Omega - \Omega_M\right)$$

$$\frac{\partial V_M}{\partial \omega} = -\frac{GM_M r^2}{r_M^3}\sum_{m=0}^{2}\sum_{p=0}^{l} k_m \frac{(2-m)!}{82+m)!} (2-2p) F_{2mp} F_{2mh}(i) \sin\left(2-2p)\alpha - (2-2h)\alpha_M + m(\Omega - \Omega_M\right)$$

where subscript M is referred to the Moon. Integrating over one orbital period, it is possible to determine the long period drift contributions. The lunar orbital parameters can be considered constant, since the Moon angular velocity is significantly smaller than the orbital one. Moreover, as in [21], also all the orbital parameters are considered constant except for the true anomaly.

Considering the following equivalences:

- $\int_0^{T_0} \frac{di}{dt} dt = \int_0^{2\pi} \frac{di}{dt} \frac{1}{n} \frac{(1-e^2)^{3/2}}{(1+e\cos\nu)^2} d\nu$, having assumed constant the eccentricity
- $\sin\left[(2-2p)\alpha - (2-2h)\alpha_M + m(\Omega - \Omega_M)\right] = \sin\left((2-2pi)\nu\right)\cos\left[(2-2p)\omega - (2-2h)\alpha_M + m(\Omega - \Omega_M)\right] + \cos\left((2-2pi)\nu\right)\sin\left[(2-2pi)\omega - (2-2h)\alpha_M + m(\Omega - \Omega_M)\right]$

- $r^2 = \left(\frac{a(1-e^2)}{1+e\cos\nu}\right)^2$

integrating over one orbital period implies to solve the following integrals:

$$\int_0^{2\pi} \frac{sin[(2-2p)\nu]}{(1+e\cos\nu)^4} d\nu$$
$$\int_0^{2\pi} \frac{cos[(2-2p)\nu]}{(1+e\cos\nu)^4} d\nu$$

The first one is always null for every value of p. The second one is always different from zero if $p = 1$. If $p = 0$ or $p = 2$, the integral is null if $e < 0.07$. Since the orbits of interest are quasi circular, the only significant contribution is that associated to $p = 1$. Thus the inclination drift will depend on the only $\frac{\partial V_M}{\partial \Omega}$. It can be divided into six components, associated to the different values of $m \in [1, 2]$ and $h \in [0, 2]$:

$$\frac{di}{dt}_{10} = -\frac{1}{6\pi}\frac{GM_M}{r_M^3}\frac{(1-e^2)^3}{n\sin i}F_{211}(i)F_{210}(i_M)\sin\left[-2\alpha_M + \Omega - \Omega_M\right]\int_0^{2\pi}\frac{1}{(1+e\cos\nu)^4}d\nu \tag{6.25}$$

$$\frac{di}{dt}_{11} = -\frac{1}{6\pi}\frac{GM_M}{r_M^3}\frac{(1-e^2)^3}{n\sin i}F_{211}(i)F_{211}(i_M)\sin\left(\Omega - \Omega_M\right)\int_0^{2\pi}\frac{1}{(1+e\cos\nu)^4}d\nu \tag{6.26}$$

$$\frac{di}{dt}_{12} = -\frac{1}{6\pi}\frac{GM_M}{r_M^3}\frac{(1-e^2)^3}{n\sin i}F_{211}(i)F_{212}(i_M)\sin\left[2\alpha_M + \Omega - \Omega_M\right]\int_0^{2\pi}\frac{1}{(1+e\cos\nu)^4}d\nu \tag{6.27}$$

$$\frac{di}{dt}_{20} = -\frac{1}{12\pi}\frac{GM_M}{r_M^3}\frac{(1-e^2)^3}{n\sin i}F_{221}(i)F_{220}(i_M)\sin\left[-2\alpha_M + 2(\Omega - \Omega_M)\right]\int_0^{2\pi}\frac{1}{(1+e\cos\nu)^4}d\nu \tag{6.28}$$

$$\frac{di}{dt}_{21} = -\frac{1}{12\pi}\frac{GM_M}{r_M^3}\frac{(1-e^2)^3}{n\sin i}F_{221}(i)F_{221}(i_M)\sin\left[2(\Omega - \Omega_M)\right]\int_0^{2\pi}\frac{1}{(1+e\cos\nu)^4}d\nu \tag{6.29}$$

$$\frac{di}{dt}_{22} = -\frac{1}{12\pi}\frac{GM_M}{r_M^3}\frac{(1-e^2)^3}{n\sin i}F_{221}(i)F_{222}(i_M)\sin\left[2\alpha_M + 2(\Omega - \Omega_M)\right]\int_0^{2\pi}\frac{1}{(1+e\cos\nu)^4}d\nu \tag{6.30}$$

where the integral $\int_0^{2\pi}\frac{1}{(1+e\cos\nu)^4}d\nu$ can be easily solved by means of the trapezoidal rule (see Appendix A). The sum of these contributions gives a very accurate estimation of the long period inclination variation. Indeed, comparing it with that obtained by simulation, the resulting average relative and absolute errors are 5.23% and 0.0080 mdeg, for mission B2 (Figure 6.43), 2.43% and 0.0087 mdeg, for mission E (Figure 6.44).

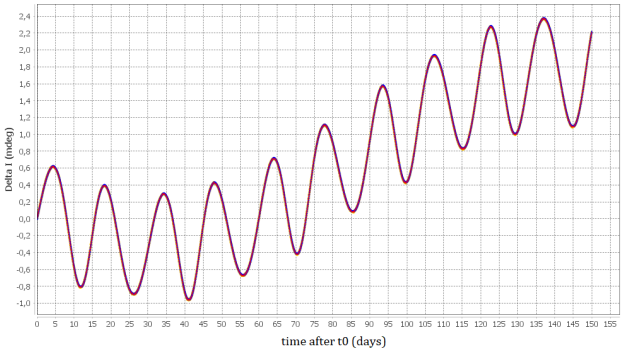

Fig. 6.43: Mission B2 - estimated and simulated inclination variations due to the lunar potential

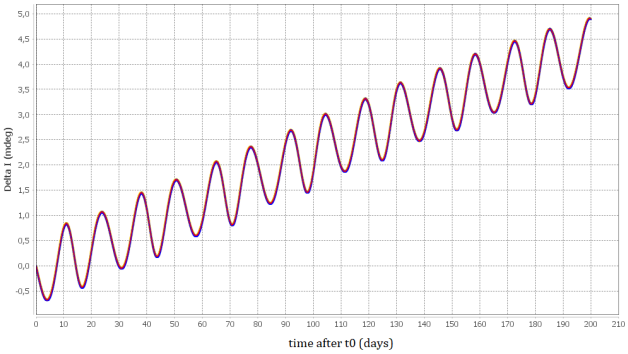

Fig. 6.44: Mission E - estimated and simulated inclination variations due to the lunar potential

Analysing term by term, it is evident that the longer period contributions to the drift are associated to $h = 1$, since they do not depend on the lunar argument of latitude: they are $\frac{di}{dt}_{11}$ and $\frac{di}{dt}_{21}$. This is confirmed also experimentally: see Figure 6.45. Thus, the longer period inclination drift due to the lunar potential can be approximated as:

$$\frac{di}{dt} = -\frac{GM_M}{r_M^3}\frac{(1-e^2)^3}{n\sin i}\left[\frac{1}{6\pi}F_{211}(i)F_{211}(i_M)\sin(\Omega-\Omega_M) + \frac{1}{12\pi}F_{221}(i)F_{221}(i_M)\sin[2(\Omega-\Omega_M)]\right]\int_0^{2\pi}\frac{1}{(1+e\cos\nu)^4}d\nu \tag{6.31}$$

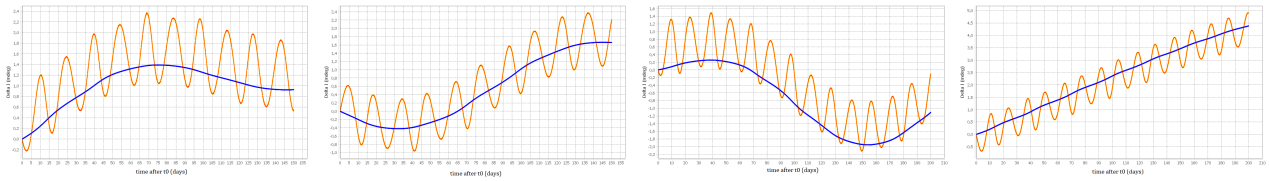

(a) Mission A2 *(b)* Mission B2 *(c)* Mission D1 *(d)* Mission E

Fig. 6.45: Estimated longer period contribution to the inclination drift due to the lunar potential

6.7.1 Inclusion of the lunar potential contribution

The longer period lunar contribution is added to the the contributions of the solar potential, the terrestrial tides and the atmospheric drag. The new results obtained are shown in Table 6.6 for mission B2 and in Table 6.7 D1 for mission D1.

Table 6.6: Mission B2 - average absolute and relative errors of the inclination drift estimation, executed considering the measures at sixteen ascending nodes and including the lunar potential longer period contributions

average error	method 1	method 2
absolute [mdeg/s]	$1.069 \cdot 10^{-7}$	$1.06 \cdot 10^{-6}$
relative	84.24%	556.7%

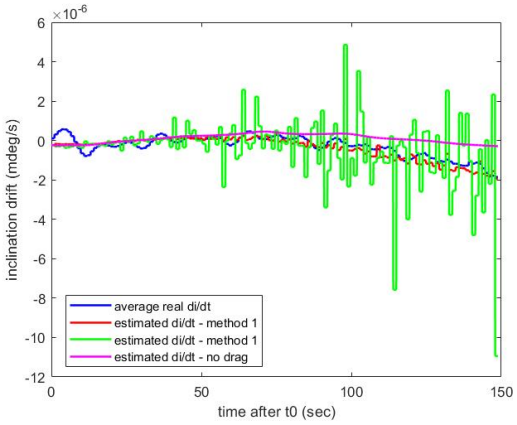

Fig. 6.46: Mission B2 - inclination drift estimated exploiting the measures at sixteen previous node and including the lunar potential

Table 6.7: Mission D1 - average absolute and relative errors of the inclination drift estimation, executed considering the measures at sixteen ascending nodes and including the lunar potential longer period contributions

average error	method 1	method 2
absolute [mdeg/s]	$2.34 \cdot 10^{-7}$	$4.45 \cdot 10^{-7}$
relative	15.02%	28.55%

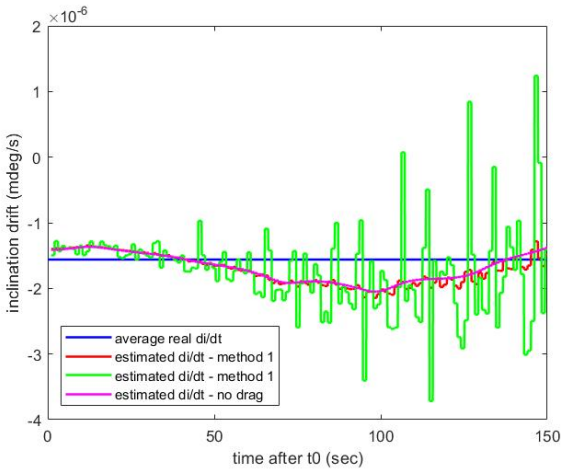

Fig. 6.47: Mission D1 - inclination drift estimated exploiting the measures at sixteen previous node and including the lunar potential

As expected the mean error decreases in case of mission B2 and it increases in case of mission D1. Indeed, including the lunar potential contribution improves the estimation of the long period inclination drift, but the estimation of the secular inclination drift is degraded (see Figure 6.48). This is the demonstration that the lunar potential longer period contributions can be neglected for sun-synchronous orbit which are not dawn/dusk, but they have to be taken into account for all the others orbits.

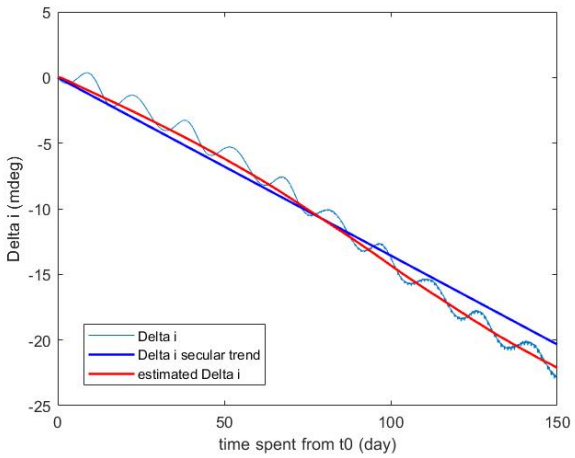

Fig. 6.48: Mission D1 - simulated free evolution of the orbital inclination compared to the one estimated considering the long period solar potential, terrestrial tides, lunar and atmospheric drag (method 1) contributions

Even though the results improve, they confirm the conclusions deduced before the inclusion of the lunar potential contribution. The error associated to method 1 is too significant, which implies that the model has to be improved.

6.8 Future Work

In conclusion, further studies are necessary. The subject concerning the atmospheric drag has to be deepened to find a better solution. The model of method 1 can be improved, for example by taking into account the Earth oblateness and the variations of the altitude scales with the altitude and the solar activity. Then, more simulations should be performed to test the validity of the model for a largest sample of orbits. Moreover, it should be necessary to determine the number of nodes to take into account in order to minimise the error for both method 1 and 2 and to compare the methods in such a way to select that allowing to determine a sufficiently accurate solution, minimising the computational time.

Chapter 7

Conclusion

The objective of the conducted work was the integration of a new kind of manoeuvre in AOC, the CNES predictable autonomous orbit controller: mixed manoeuvres. They are useful to perform concurrently the in-track and cross-track orbit control, which allows to improve the AOC station keeping performances. Their integration has been conducted in such a way to maintain the original algorithm working principles: they have been conceived as modified classical cross-track station keeping manoeuvres to which a component is added if an in-track correction is necessary. Of course, some limitations concerning the manoeuvres inclination over the orbital plane and their magnitude have been taken into account in order to avoid the instruments glare and to fulfill the propulsion systems constraints. The performed simulations show that the integration has been correctly executed and demonstrate its utility: the results are consistent with the analysed missions characteristics and the algorithm behaviour; the station keeping performances improve. In particular, as expected, the improvement is important for missions characterised by a low-thrust propulsion system. During this work of integration, an optimiser has been realized to set the parameters with the largest influence on the missions performances.

Finally, a new study has been started whose objective is to determine analytic and semi-analytic models of the long period inclination drift, sufficiently accurate to be exploited by AOC for the cross-station keeping manoeuvres computation. The main orbital perturbation causing long period and secular variations of the low orbits inclination are the Sun gravitational potential, the terrestrial tides and the atmospheric drag. The introduced analytic formulations of the drift due to these perturbations are accurate, except for the atmospheric drag. The model associated to the Sun gravitational potential was already exploited in the algorithm. An analytic model of the drift due to the terrestrial tides has been determined: it allows to obtain very precise estimations. Finally, a semi-analytic model of the drag effects has been introduced. The drag effects are the most complex to determine and it will be necessary to continue the study of this subject in future. In future, it could be interesting also to analyse the solar radiation pressure long period effects on the drift. The solar radiation pressure long period contribution is almost negligible, but still present: it could be possible to estimate a priori an appropriate constant value to take it into account in the drift estimation. Finally, it will necessary to study the effects of the new proposed way to estimate the inclination drift on the algorithm behaviour, mainly to determine if it is beneficial in terms of computational cost and station keeping performance.

Despite the promising results obtained with the integration of in-track cross-track manoeuvres and the elevated station keeping performance obtained, the algorithm is not still able to fulfill completely all the kinds of low-Earth orbit missions station keeping constraints. This is the main reason why the study of the perturbations effects over the inclination drift has been performed. Thus, as first next future step this study will have to be completed. Moreover, a similar study concerning the argument of latitude acceleration will have to be performed.

Appendix A

A.1 Legendre polynomials and Legendre functions

For every $l \geq 0$, a Legendre polynomial is defined as:

$$P_l(x) = \frac{1}{2^l l!} \frac{d^l[(x^2-1)^l]^l}{dx^l} \tag{A.1}$$

For every $l \geq 0$, for every $0 <= m <= l$, in the dominion $[-1; 1]$, a Legendre function is defined as:

$$P_{lm} = (1-x^2)^{\frac{m}{2}} \frac{d^m P_l(x)}{dx^m} \tag{A.2}$$

An important property of the Legendre functions and polynomials is the Legendre addition formula [16]. Let be S_1 and S_2 two points belonging to the same sphere of latitudes and longitudes (ϕ_1, λ_1) and (ϕ_2, λ_2) respectively. If θ is their angular distance, considering a frame centered at the sphere center, it results that:

$$\cos\theta = \sin\phi_1 \sin\phi_2 + \cos\phi_1 \cos\phi_2 \cos(\lambda_2 - \lambda_1)$$

$$P_l(\cos\theta) = P_l(\sin\phi_1) P_l(\sin\phi_2) + 2 \sum_{m=1}^{l} \frac{(l-m)!}{(l+m)!} P_{lm}(\sin\phi_1 P_{lm}(\sin\phi_2) \cos(m(\lambda_2 - \lambda_1))$$

A.2 Newton method

The Newton method is a numerical algorithm for computing an approximation of the roots of the equation $f(x) = 0$.

Let be $f(x)$ be a continuous differentiable function and let r be the searched root: $f(r) = 0$. The Newton method is an iterative method that, starting from an initial guess x_0, computes an improved estimate x_k of r at each iteration. It is based on the idea of linear approximation. Indeed at each iteration the next estimate is computed as:

$$x_{k+1} = x_k - \frac{f(x_k)}{\frac{df(x_k)}{dx}}$$

From a geometric point of view, the method uses the slope of the function $f(x)$ at the current iterative solution x_k to find the the solution x_{k+1} in the next iteration. The Newton method is characterised by a locally quadratic convergence: from a suitable iteration, the number of correct decimal places in the solution doubles after each iteration.

A.3 CMA-ES

The Covariance Matrix Adaptation Evolution Strategy (CMA-ES) is an evolutionary strategy used to solve non-linear non-convex black-box optimisation problems.

It is possible to define a black-box optimisation problem as a problem whose objective is to minimise a cost function

$$f: \quad \mathbb{R}^n \to \mathbb{R}$$
$$\mathbf{x} \to f(\mathbf{x})$$

whose values at the evaluated search points are the only accessible information. The problem domain is assumed continuous. The algorithms implementing CMA-ES generate randomly the search points, by sampling a multivariate normal search distribution, $\mathcal{N}(\mathbf{m}, \mathbf{C})$, characterised by a mean $\mathbf{m}$ and a covariance matrix $\mathbf{C}$:

$$\mathbf{x}_k^{g+1} \sim \mathbf{m}^{(g)} + \sigma^{(g)}\mathcal{N}(0, \mathbf{C}^{(g)})$$
$$k = 1, ..., \lambda$$

where

- $\mathbf{x}_k^{g+1}$ is the $k-th$ offspring (search point) at the $g+1$ generation
- $\mathcal{N}(0, \mathbf{C}^{(g)}$ is a multivariate normal distribution with zero mean. It holds

$$\mathbf{m}^{(g)} + \sigma^{(g)}\mathcal{N}(0, \mathbf{C}^{(g)}) \sim \mathcal{N}(\mathbf{m}^{(g)}), \sigma^{(g)}\mathbf{C}^{(g)})$$

- $\mathbf{m}^{(g)}$ is the mean value at the g generation;
- $\mathbf{C}^{(g)}$ is the covariance matrix up to the scalar factor $\sigma^{(g)}$ at the g generation;
- $\sigma^{(g)}$ is the step-size at the g generation.

A generation coincides to an algorithm iteration at which a set of search points (individuals) are evaluated. After the analysis of each generation, the mean $\mathbf{m}$ and the covariance matrix $\mathbf{C}$ are updated, until an acceptable solution is found. The covariance matrix updating is referred to as covariance adaptation: it allows to reduce the number of f-evaluations needed to reach a target f-value. At the first generation, the mean value coincides with the search point initial guess; the initial covariance matrix is imposed as a diagonal matrix whose values are the guessed deviations of the initial guess components with respect to those of the optimum. The new mean is computed as a weighted average of ζ selected points, with $0 < \zeta < \lambda$:

$$\mathbf{m}^{(g+1)} = \sum_{i=1}^{\zeta} w_i \mathbf{x}_i^{(g+1)}$$

$$\sum_{i=1}^{\zeta} w_i = 1$$

The new re-estimated covariance matrix is:

$$\mathbf{C}_{\zeta}^{(g+1)} = \sum_{i=1}^{\zeta} w_i (\mathbf{x}_i^{(g+1)} - \mathbf{m}^{(g)})(\mathbf{x}_i^{(g+1)} - \mathbf{m}^{(g)})^T$$

Other covariance adaptation strategies can be adopted. For example, another possible estimator to adopt after a sufficient number of generations can be the mean of the previous estimated covariance matrixes. Indeed, in order to achieve a fast research, the population size λ at each generation should be small. However, a small value of λ can imply bad estimator for the updated covariance matrix. As a remedy, information from previous generations can be exploited, using the following estimator:

$$\mathbf{C}^{(g+1)} = \frac{1}{g+1} \sum_{i=0}^{g} \frac{1}{\sigma_i^2} \mathbf{C}_{\zeta}^{(g+1)}$$

More detailed information about the algorithm and the other covariance adaptation methods can be found in [31].

The CMA-ES is considered as state-of-the-art in evolutionary computation: it is used as standard tool to solve continuous optimisation problem in research and industrial environment. It is implemented in Java, Matlab, Octave and C, C++, Fortran and Phyton: it is possible to find the online documentation in [32].

A.4 Moving-Average Filter

A moving-average filter is a common method used for smoothing noisy data [33]. It slides a window of length along the data, computing averages of the data contained in each window. The following difference equation defines a moving-average filter of a vector $\mathbf{x}$:

$$y(n) = \frac{1}{windowSize}(x(n) + x(n-1) + ... + x(n-(windowSize-1)))$$

A.5 Trapezoidal rule

The trapezoidal rule is a technique exploited in numerical analysis to approximate the integral:

$$I(f) = \int_a^b f(x)dx$$

with $[a, b]$ finite. The trapezoidal rule consists in approximating $f(x)$ by a straight line joining $(a, f(a))$ and $(b, f(b))$ and the area subtended by it by a trapezoidal region. Thus, the integral is approximated as follows:

$$I(f) \sim \Big(\frac{b-a}{2}\Big)[f(a) + f(b)]$$

If $b-a$ is not sufficiently small, the trapezoidal rule is not sufficiently accurate. However, it is possible to divide the integral into a sum of integrals over small sub-intervals, usually characterised by the same length, and apply to each of them the trapezoidal rule:

$$I(f) \sim \frac{b-a}{n}\Big(\frac{f(a)+f(b)}{2} + \sum_{k=1}^{n-1} f\Big(a + k\frac{b-a}{n}\Big)\Big)$$

with $n \geq 1$, $n \in \mathbb{N}$. It is possible to find further details in [34].

Bibliography

[1] Laurichesse D. Grondin M. Bertrand R. Lamy A., Charmeau C. *Experiment of autonomous orbit control on the Demeter satellite.* International Symposium on Space Flight Dynamics, Munich, Germany, 2004.

[2] Wertz J.R. Collins J.T., Dawson S. *Autonomous constellation mantainance system.* 10th Annual AIAA/USU Conference on Small Satellites, Utah State University, Utah, 1996.

[3] Advanced avionics concepts: autonomous spacecraft control. Technical report, NASA JohnsonSpaceCenter, 1989.

[4] Oneweb. https://directory.eoportal.org/web/eoportal/satellite-missions/.

[5] Maute A.P.A. Autonomous orbit control method and system for a geostationary satellite. Technical report, 1992.

[6] Bernstein H. Chao C.C. Onboard stationkeeping of geosynchronous satellites using a global positiong system receiver. *Journal of guidance, control and dynamics*, 17, 1994.

[7] Wertz J.R. Gurevich G., Bell R. *Autonomous on-board orbit control: flight results and applications.* AIAA 2000 Conference and Exposition, Long Beach, California, 2000.

[8] J.R. Wertz. *Autonomous Navigation and Autonomous orbit control in planetary orbits as a mean of reducing operations cost.* 5th International Symposium on Reducing the Cost of Spacecraft Ground Systems and Operations Pasadena, Pasadena, California, 2003.

[9] D'Amico S. Radice G. De Florio, S. *Precise autonomous orbit control in low earth orbit.* AIAA/AAS Astrodynamics Specialist Conference, Minneapolis, Minnesota, 2012.

[10] Xing G. Parvez S.A. Autonomous orbit control with position and velocity feedback using modern control theory. Technical report, 1997.

[11] Sandre T. Gicquel A. Bonaventure F., Baudry V. *Autonomous orbit control for routine station-keeping on a leo mission.* International Symposium on Space Flight Dynamics, Pasadena, California, 2005.

[12] Azema G. Thomassin J., Ecochard M. *Predictive autonomous orbit control method for low Earth orbit satellites.* International Symposium on Space Flight Dynamics, Matsuyama, Japon, 2017.

[13] Vallado D. A. *Fundamentals of Astrodynamics and Applications.* Space Technology Library, New York, 1997. Sections: 1.4, 8.2, 8.3, 8.5, 10.4.

[14] International earth rotation and reference systems service, 2014. http://hpiers.obspm.fr/iers/bul/bulb_new/bulletinb.pdf.

[15] International atomic time (tai). https://www.bipm.org/en/bipm-services/timescales/tai.html.

[16] Carrou J. *Mécanique Spatiale - tome I.* Cépaduès-Editions, CNES, Toulouse, France, 1995. Sections: 5.1, 5.A.1.1, 5.A.1.2, 13.4.1, 13.6.2, 13.6.3, 13.6.4.

[17] Battin R. H. *An introduction to the Mathematics and Methods of Astrodynamics.* AIAA Education Series, New York, 1999.

[18] Chao C. *Applied Orbit Perturbation and Maintenance.* AIAA, Inc., Reston, Virginia, 2005.

[19] Blitzer L. *Handbook of Orbital Perturbations.* University of Arizona, Tucson, Arizona, 1970.

[20] Manglaviti S. Performance analysis of the predictive autonomous orbit control (AOC) method. Technical report, CNES, Toulouse, France, 2018.

[21] Azema G. Lamy A. *Selection and optimization of a constellation of satellites for continuous zonal coverage.* International Symposium on Space Flight Dynamics, Toulouse, France, 2009.

[22] Cook E.G. Luni-solar perturbations of the orbit of an earth satellite. *The Geophysical Journal of the Royal Astronomical Society*, 1961.

[23] W.M. Kaula. Development of the lunar and solar disturbing functions for a close satellite. *The Astronomical Journal*, 67(5), 1962.

[24] W.M. Kaula. *Theory of Satellite Geodesy.* Blaisdell publishing company, Los Angeles, California, 1966.

[25] Montenbruck O. Fiedler H. Cefola P., Setty S. Application of semi-analytical satellite theory orbit propagator to orbit determination for space object catalog maintenance. *Advances in Space Research*, 57, 2016.

[26] Estes R. Musen P. On the tidal effects in the motion of of artificial satellites. *Celestial Mechanics*, 6, 1971.

[27] Balmino G. Lambeck K., Cazenave A. Solid earth and ocean tides estimated from satellite orbit analysis. *Reviews og geophysical and space physics*, 12(3), 1971.

[28] Taburiau D. Valorge C. Structure d'accueil du problème dynamique (sadyn) - manuel d'algorithmique du modèle de force marte - marees terrestres. Technical report, CNES, Toulouse, France, 1992.

[29] Scott D.W. King-Hele D.G. The effect of atmospheric rotation on a satellite orbit, when scale height varies with height. *Planet. Space Sci.*, 17, 1969.

[30] Stegun I. A. Abramowitz M. *Handbook of mathematical functions with formulas, graphs, and mathematical tables.* United States Departement of Commerce, Washington D.C., 1964.

[31] Nikolaus Hansen. The cma evolution strategy: A tutorial. Technical report, Université Paris-Saclay, 2016.

[32] The cma evolution strategy, 2016. http://cma.gforge.inria.fr.

[33] Filter- 1-d digital filter, 2019. https://fr.mathworks.com.

[34] Atkinson K. E. *An introduction to numerical analysis (2nd ed.).* John Wiley Sons, New York, 1989.